A CRITICAL ANALYSIS OF LUNAR TEMPERATURE MEASUREMENTS IN THE INFRARED

by

Hector C. Ingrao, Andrew T. Young, & Jeffrey L. Linsky

Harvard College Observatory
Cambridge, Massachusetts (USA)

Scientific Report No. 6
NASA RESEARCH GRANT No. NsG 64-60

* * * * *

April 15, 1965

Prepared for

NATIONAL AERONAUTICS AND SPACE ADMINISTRATION

The authors are particularly indebted to Professor Donald H. Menzel for his continuous interest in this phase of the project as well as for many fruitful discussions.

ABSTRACT

The Harvard College Observatory radiation pyrometer for lunar measurements and the associated data reduction techniques are described. Under good observing conditions, this system can measure the brightness temperature of a square area of 12 x 12 kilometers at the sub-earth point of the lunar surface, located with an accuracy of ± 2 km; relative temperatures near the subsolar point can be measured with a precision of ± 1°K and an absolute accuracy of ± 8.5°K, and lower temperatures can be measured accurately down to about 180°K with a post-detection integration time of 0.2 seconds. Below this temperature, the integration time has to be increased since the instrumental noise starts contributing significantly to the uncertainty of temperature measurements. Some data obtained at the total lunar eclipse on June 24-25 and December 18-19, 1964 are presented.

Propagation of error analysis shows that it would be very difficult to determine the subsolar point temperature with an absolute accuracy better than ± 5°K, or a few degrees during eclipse. Numerical integration of the heat-flow equation for several lunar surface models shows that the accuracy of infrared brightness temperature measurements during an eclipse is too low to permit realistically more than the most general conclusions about the lunar surface. In the two-layer model thicknesses greater than about 4 mm cannot be measured by infrared technique.

1) The eclipse observations cannot be reconciled with a model having homogeneous surface material with temperature-independent thermal properties.

2) Eclipse observations of the crater Tycho and its environs are consistent with models having two-layer temperature-independent thermal properties.

3) Very different models can have similar surface temperatures during an eclipse, but which differ by 10°K or more at depths of several millimeters. The combination of millimeter-wave data with infrared data may possibly distinguish one model from another.

Homogeneous models with linearly temperature-dependent thermal properties and models including a radiative transfer term give a better fit with the lunation data of Murray and Wildey.

Since the eclipse and lunation data may both be described by several different models of the thermal properties of the lunar surface, at present the possibility of our learning about these properties from infrared data alone seems very doubtful.

A general computer program coded in the FORTRAN language has been written which solves the heat conductivity equation for a multilayer lunar surface and for arbitrarily temperature-dependent thermal properties (Scientific Report #7, in preparation).

CONTENTS

I. Introduction to the Observational Problem

This report will discuss problems of measuring lunar temperatures in the infrared part of the spectrum, particularly in regard to data gathering, data reduction, precision of the measurements, and the significance of the different models used to interpret the data.

The type of measurements made and the methods used will be determined solely by the information that we want to obtain from the data: the choice of high or low spatial resolution, high or low temperature resolution, and relative or absolute measurements can be made only on the basis of the answers we are seeking from our program.

The specific instrumentation obviously will be determined by the program to be carried out. For example, to correlate radio with infrared measurements, instruments with resolution elements of several minutes have been used. With these instruments it is not a problem to locate the area under measurement within a fraction of the resolution element. However, if the program calls for high spatial resolution and one expects to correlate the thermal features with the lunar features, the observational and instrumental problem is completely different. For example, if the resolution element is 9" x 9" in size, its accurate location is very difficult and, in fact, requires us to solve an astrometric problem.

At high spatial resolution the stability requirements

of the telescope also are more demanding. If the Moon is being scanned, we must be able to determine the position of the resolution element on the lunar surface as a function of time, and within a fraction of the resolution element size.

The problem of temperature resolution can be a serious one, depending upon the dynamic range that our equipment has to handle and the time allowed for a complete measurement. A scan during full Moon and through the subsolar point must handle a signal ratio power of the order of 270, if we assume two extreme temperatures, 150°K and 400°K. If the noise level of the pyrometer is of the order of 5×10^{-11} watts and if we want the measurements to be limited only by this noise level, we have to resolve 3 parts in 1000 at 400°K. To handle this amount of information, rather complex equipment is needed.

The probable error in the absolute temperature measurements will depend mainly on the accuracy of the measurements of the instrumental parameters and of the atmospheric attenuation.

For measurements of relative temperatures, knowledge of the instrumental parameters is not so important and less accuracy is required in measurements of the atmospheric attenuation.

In our program of lunar temperature measurements, we have designed and built at Harvard College Observatory

a radiation pyrometer.[1] This instrument was designed to provide high spatial resolution, high accuracy in locating the resolution element on the lunar surface, and the highest temperature resolution that can be achieved with thermal detectors. This instrument has three channels: infrared, visual, and photographic. The three channels use the same telescope optics; an optical switching mechanism allows one to observe the Moon 50% of the time in the infrared and 50% of the time in the visual range and photographically, at an adjustable rate from 10 cps to 70 cps. The pyrometer has the following data outputs: 1) a 35 mm film having a field of view 7.5' x 5.0', with a crosshair centered on the frame, which coincides with the barycenter* of the infrared detector; 2) a paper chart on which are recorded the infrared signal, marks indicating the time, marks indicating when a picture has been secured, and a mark indicating an event that needs to be recorded; and 3) a magnetic tape recording on which the observer describes the area under measurement or any event important to the data analysis, and the operator of the electronic equipment records relevant data; the tape also records WWV time signals and a tone indicating that an event needs to be recorded.

---

*We define the barycenter as the point in the detector with the highest responsivity.

II. Identification of the Resolution Element on the Lunar Surface

The main difficulty in high spatial resolution pyrometry is the problem of identifying the resolution element on the lunar disk. Observations of high spatial and temperature resolution must be obtained, in general, with reflectors of fairly big aperture, 48 inches (122 cm) and larger. The use of two independent optical systems, one to identify the resolution element and the other for pyrometry, introduces the difficult problem of keeping both optical axes collimated at different attitudes of the telescope; errors can be of the order of minutes of arc.

However, schemes can be devised to solve this problem and, without discussing the advantages and disadvantages of the several methods used, we will describe the one used in our pyrometer. The basic principle is indicated in Figure 1. The equipment is designed to operate with optical systems with f-numbers between 3.5 and 6. The telescope beam is chopped at a rate which can be adjusted from 10 cps to 70 cps. The chopper is made of glass and has evaporated aluminum on the front face and evaporated gold on the back.

When the chopper blocks the optical path to the detector in position D, the focal plane d-d' is transferred to the position k'-k. We can call the point R the homologue of the point D that defines the geometrical center of the detector. Coplanar with the image plane k'-k is a reticle with 1/2 millimeter divisions, illuminated at the edge. A flat mirror E folds back the beam and the photographic

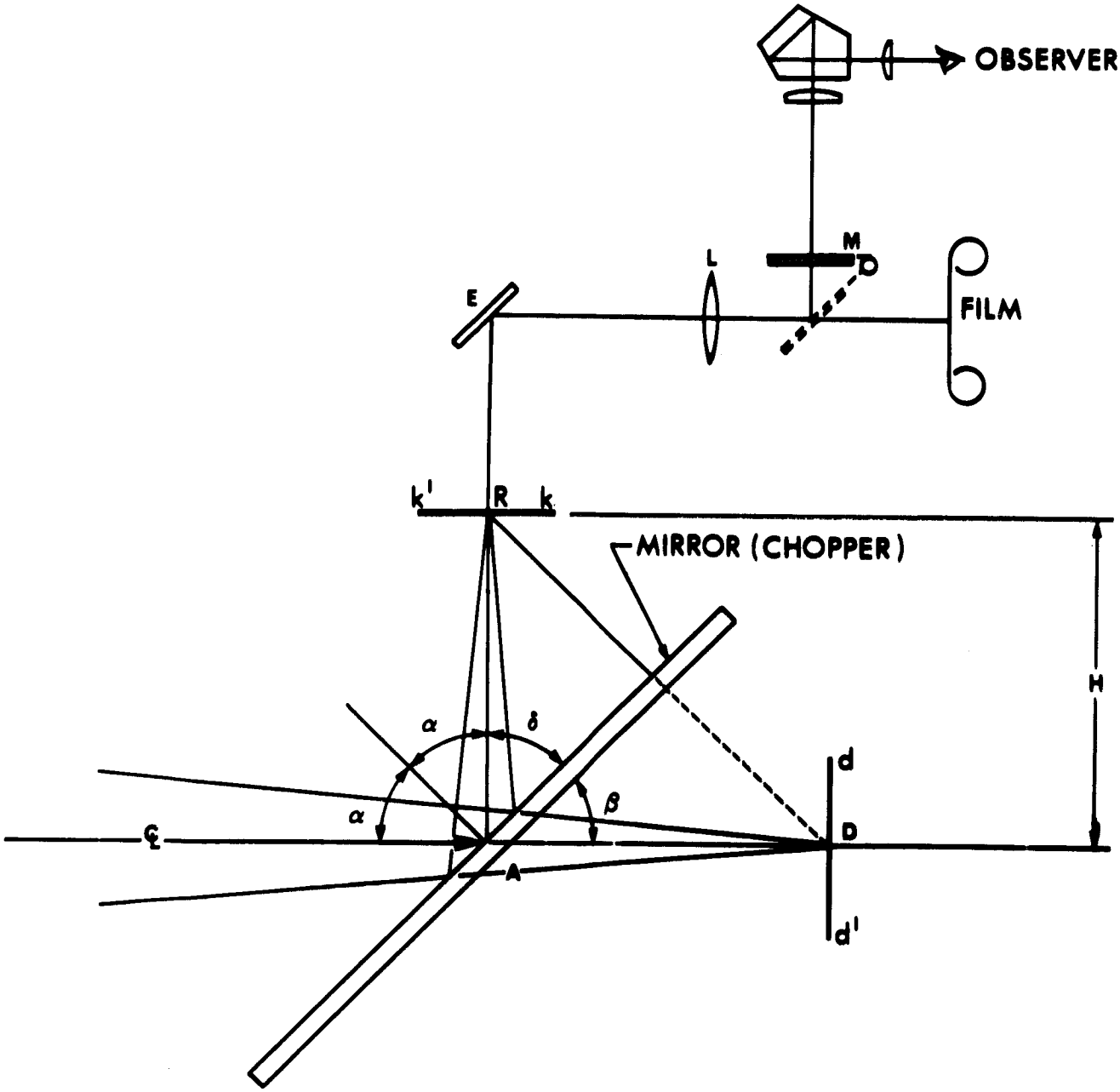

FIG. 1. Basic principle of the mechanism for identifying the resolution element on the lunar disk in the radiation pyrometer developed at Harvard College Observatory.

objective L images the plane k'-k onto the photographic film. A reflex system with mirror M and a pentaprism allows for visual observation of the same field of view.

After the chopper has been made perpendicular to the axis of rotation by means of an autocollimator, the whole optical train is adjusted. For this adjustment we have an auxiliary optical system that is attached to the pyrometer head flange and gives a point image on D which, by means of the chopper, can be transferred to R.

For the sake of simplicity we will consider the reticle alignment a two-dimensional problem; it is, in fact, a three-dimensional one.

If we assume that the plane of the mirror chopper has been fixed and that the position D of the detector is determined, the homologous point R is defined. Since $\gamma = \beta$ for any α, the alignment will depend only upon the relative positions of D, the chopper and R.

This method, because of the design of the pyrometer head, could produce a systematic error in the positioning of D. There is always an error in the positioning of the detector flake with respect to the detector holder, which makes the position of D indeterminate. Since we assume that the position of D is known for the alignment in the laboratory, a systematic error is introduced in the positioning of the reticle. Moreover, since the pyrometer head is designed for use with different detectors, we should expect a different systematic error for each detector.

To determine the systematic error at the telescope, we scan the detector several times with a star image in a direction parallel to the diagonals (square detector) until we get the maximum response. If we correlate photographically the position of the star image on the reticle with maximum signal output from the detector, we can measure the systematic error very accurately.

Figure 2 shows an actual picture taken with the photographic channel of the pyrometer. The picture was secured at 01:21:50 UT, December 19, 1964, a few minutes before total eclipse, using Edgerton, Germeshausen & Grier XR film plus Wratten #15 filter and 1/15 second exposure time. With pictures of this type, the task is to determine the orthographic coordinates of the reticle, which, in turn, are the coordinates of the barycenter of the detector. We obtain this information by projecting each frame on the proper plate of the "Orthographic Atlas of the Moon."* A special projecting system (shown in Figure 3) has been constructed in our laboratory for this purpose.

The foreground of Figure 3 shows the Leitz film projector which is mounted on a structure having 3 degrees of freedom. The projector head can be rotated 360 degrees. As seen in the background of Figure 3, the image is projected onto a screen mounted on a gimbal to simulate to first order

---

*"Orthographic Atlas of the Moon," The University of Arizona Press, 1961.

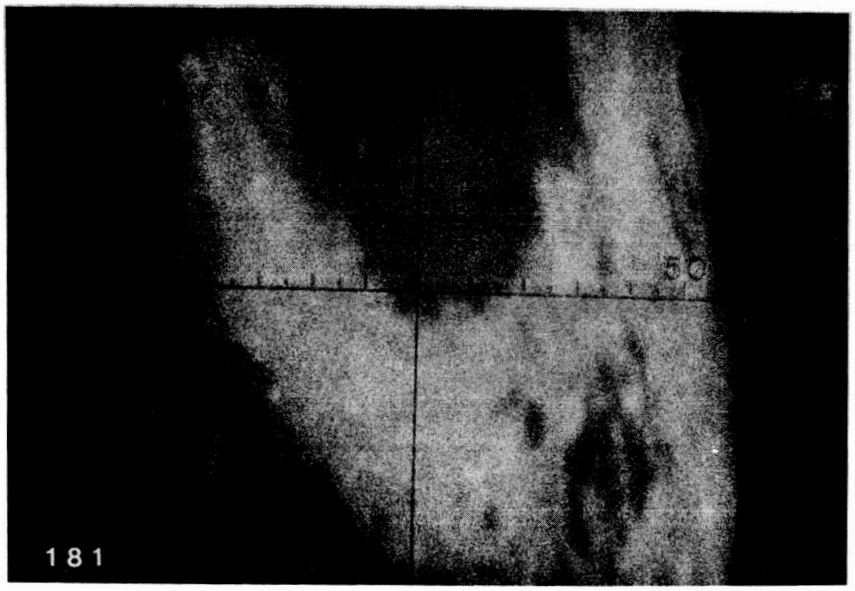

FIG. 2. Picture obtained with the photographic channel of the radiation pyrometer, using Edgerton, Germeshausen & Grier XR film, Wratten #15 filter, and an exposure time of 1/15 second. The center of the reticle is on the south tip of Mare Crisium (Lunar Eclipse, December 18-19, 1964).

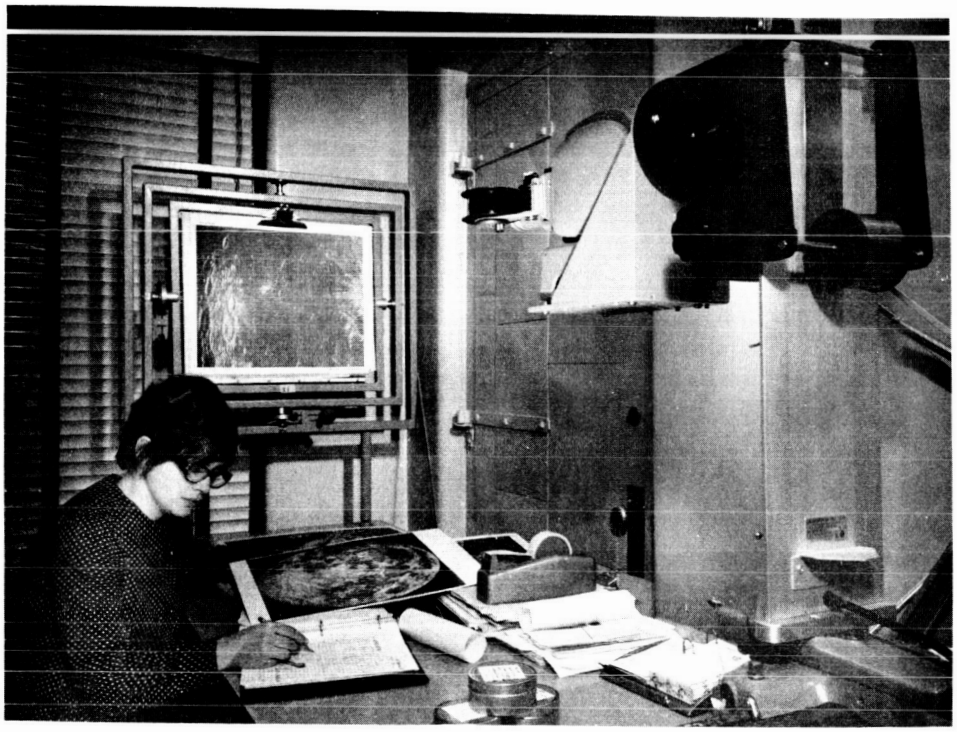

FIG. 3. Film analyst making initial identification of a lunar region in one picture frame using a high contrast photograph of the Moon. In the background the projection screen mounted on a gimbal; in the foreground the film projector mounted on a structure with three degrees of freedom. The rotation of the projector head gives the fourth degree of freedom.

the librations of the Moon. After studying the projected frame, the film analyst must locate the exact area on a photograph of the Moon so that the appropriate plate from the Photographic Lunar Atlas* can be chosen. The projected image is then superimposed on the correct Lunar Atlas plate. In order to ascertain whether the superimposed image is identical to that on the plate, a sheet of white opaque paper is held over the screen and moved around while the outstanding features are lined up with photographic plate. The point where the reticle crosses is marked on the plate, and is then transferred to the corresponding orthographic plate. The ξ and η coordinates are determined and recorded in tabular form along with the number of the picture frame. These coordinates will be used later in a computer program to determine the coordinates of the barycenter of the detector as a function of time. Because we have less varied illuminations of the Moon on Orthographic Atlas plates than on Photographic Atlas plates, we must ordinarily use the Photographic Atlas plates for the initial plotting of coordinates.

The accuracy in determining the orthographic coordinates of the barycenter of the detector depends upon the quality of the raw data. For pictures obtained under good conditions (seeing disk 2" or smaller), having good contrast

---

*"Photographic Lunar Atlas", The University of Chicago Press, 1960.

and a reasonable number of identifiable lunar features, the standard deviation in the determination of the orthographic coordinates is ±3". For pictures obtained under poor seeing conditions (5" or larger), having poor contrast and few identifiable features, the standard deviation will be between 6" and 8".

Usually we take about four pictures per scan; thus, in the best case we know the position of the line of scan within 1.5", and in the worst within 4.0".

The previous discussion regarding the location of the resolution element apply only to the illuminated part of the Moon. On the basis of these measurements, we can also determine the position of the line of scan on the shadowed areas, as shown in Section IV. The problem of location on the eclipsed Moon is more complicated, especially during dark eclipses. Still in some cases it is possible to take the identifying pictures with high-speed film or an image converter, or to take the pictures at the limb of the Moon against the star background. In the last case, the position of the line of scan on the Moon will be found from the position of the reticle with respect to a given set of background stars.

III. Spatial Resolution

In our radiation pyrometer the size of the resolution element will be limited by the telescope optics, the detector size, and the atmospheric seeing. If our measurements are in the range of 8 - 14 microns and we can assume 10 microns as the effective wavelength, and are using a 60-inch telescope, the diameter of the Airy disk is 3.3", that of the second dark ring of the diffraction pattern is 6.0", and that of the third is 8.7". About 94 percent of the total flux falls within the third diffraction ring of an unobstructed circular aperture. On this basis we established as a requirement that the detector should cover at least the third ring of the diffraction pattern; this means that for a telescope with a scale of s = 25"/mm, the detector should be of the order of 0.35 mm in size. The thermistor bolometer used in our pyrometer, 0.1 mm x 0.1 mm in size and immersed in a Germanium lens, gives an effective size of 0.35 mm x 0.35 mm. To obtain the instrumental profile experimentally we scanned the field of view of our radiation pyrometer with the image of a star, Alpha Scorpii, and the pyrometer mounted at the Newtonian focus of the 74-inch telescope in Pretoria (Republic of South Africa). Figure 4a shows the photographic record; each small division of the reticle is equivalent to 11". Frames 1 to 4 show Alpha Scorpii crossing the field along the horizontal line of the reticle. The time when the picture was secured is indicated in the upper part of each frame. The film used was E,G&G XR, the chopping frequency 14 cps and the shutter speed 1.0 second. Figure 4b

shows the output of the radiometer when Alpha Scorpii scanned the detector. The marks 1, 2, 3, and 4 indicate the times at which the identifying pictures were secured. The measurements were taken nearly along the diagonal of the square detector.

A series of similar scans was obtained parallel to the horizontal line of the reticle and spaced only a few seconds of arc apart. Using these measurements we determine the size of the resolution element, the responsivity diagram of the pyrometer-telescope combination, as well as any systematic error in the location of the barycenter of the detector with respect to the center of the reticle. On the basis of the record shown in Figure 4b, we measured a resolution element 8" x 8" between 50% power points.

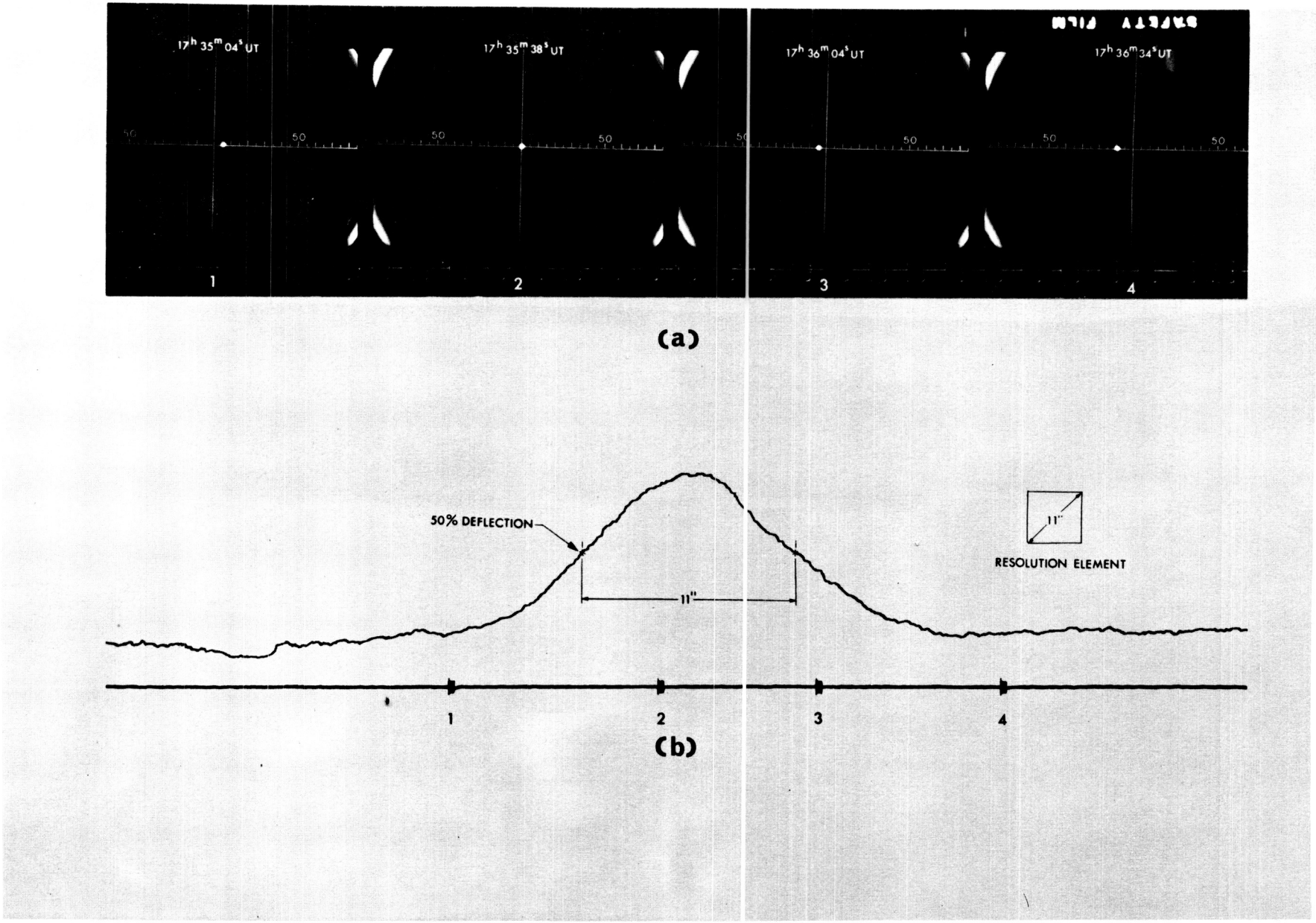

FIG. 4. Measurement of the radiation pyrometer profile: a) frames 1 to 4 show Alpha Scorpii crossing the field of view of the photographic channel of the radiation pyrometer along one line of the reticle; b) output of the radiometric channel when Alpha Scorpii crossed the field of view.

IV. Astrometric Analysis of the Observational Data

Two modes of scanning can be chosen in the family of sequential read-in simultaneous read-out*: fix the telescope relative to the Earth and let the Moon drift in the field of view of the detector; or track the Moon with the telescope and have built in the pyrometer a scanning device to provide a television-type raster. In the first method, the spatial-time relationships can be easily determined if no perturbations are introduced in the mode of scanning. Under actual observing conditions, this is not always true; if we use a telescope with a plate scale of 25"/mm (310 inches focal length) and a resolution element of 10" x 10", a displacement of 400 microns at the end of the telescope will be equivalent to the displacement of one resolution element. With a telescope of 60 inches or larger, a displacement of 400 microns can be produced by the wind, and by perturbations introduced by the observer, displacement of the telescope mirror objective, etc. The second method of scanning involves all the problems of the first method; an additional difficulty is the fact that to find the location of the detector within one resolution element on the lunar disk, the scanning mechanism should have the relationship between position and time known within ±.5% of the lunar radius.

Of the two basic modes of scanning, we chose the first one. For this method, we analyzed the astrometric problem and worked out a computer program to give the orthographic coordinates

---

*W. K. Weihe, "Classification and Analysis of Image-Forming Systems," Proc. Inst. Radio Engrs. 47, 1593 (1959).

of the resolution element as a function of time. It is clear from the physical situation that if the detector moves at a constant rate in each coordinate, the entire course of the scan relative to the Moon, as a function of time, can be found from two timed photographs. If the telescope is held fixed relative to the Earth, the rates are known exactly and only one photograph is needed.

The computer program logically consists of three blocks. The first block reads in the observer's coordinates, the Lunar Ephemeris, and other fixed data needed to solve the problem. The second block computes the hour angle and declination of the detector at the time of every photograph. The third block uses the photographic data to interpolate the hour angle and declination, and hence the lunar coordinates of the detector, at any arbitrary time -- for example, a time at which a temperature datum is measured.

In addition to the Lunar Ephemeris, the basic data consist of the observer's astronomical latitude, longitude, and height above sea level, and the effective wavelengths of the photographic and infrared detectors. The wavelengths are needed to compute the differential refraction due to atmospheric dispersion.

Ordinarily, the observer's coordinates are read first. The meridional rectangular coordinates are evaluated by means of

$$\rho \sin \phi' = (1-e^2)\sin \phi/H \qquad (1)$$

and

$$\rho \cos \phi' = \cos \phi/H \ , \qquad (2)$$

where ϕ = geodetic latitude, ϕ' = geocentric latitude, e = the eccentricity of the meridian, and

$$H = \sqrt{1-e^2 \sin^2 \phi}\ /(1+h/a) \ , \qquad (3)$$

where a is the equatorial radius of the Earth. Equations (1) and (2) are exact if h = 0; the approximation made in Eq. (3) is correct to order (1/f)(h/a) or about 5×10^{-7} per kilometer above sea level, an accuracy probably greater than the adopted values of $e^2 = 0.00672267$ and $1/a = 1.567794 \times 10^{-7}$.

These exact forms are faster and simpler for the computer than the usual expansions in Fourier series in ϕ, since only three elementary functions (sin ϕ, cos ϕ, and a square root) need to be evaluated.

The second set of fixed data consists of the effective wavelengths λ_P of the photographic and λ_D of the infrared detection systems; these are used to compute the differential refraction due to atmospheric dispersion between the two wavelengths. Since the correction is very small, less than 4" for our work even at a zenith distance of 75°, a rough approximation is good enough. We adopt the simple relation r = (n-1) tan Z, where r is the refraction in radians, Z is

the zenith distance, and n the refractive index of air at the telescope. The differential refraction is then

$$\Delta r = \left[(n-1)_P-(n-1)_D\right]\tan Z \ . \qquad (4)$$

The square bracket is evaluated for standard conditions from the Edlén formula:

$$\Delta(n-1)_{} = 2.94981 \times 10^{-2}\left[1/(146-\nu_P^2)-1/(146-\nu_D^2)\right] +$$

$$2.554 \times 10^{-4}\left[1/(41-\nu_P^2)-1/(41-\nu^2)\right] \ , \qquad (5)$$

where

$$\nu_P^2 = 1/\lambda_P^2 \ , \quad \nu_D^2 = 1/\lambda_D^2 \qquad (6)$$

for λ in microns. The accuracy needed for Δr is about 10%, or roughly 1/20 of the detector diameter at $Z = 75°$. To this order it is immaterial whether the observed (refracted) or calculated (unrefracted) zenith distance is used, as their difference is about 10^{-3} radian at $Z = 75°$. According to Penndorf[2] the Edlén formula may be slightly in error in the infrared, but the indicated error in $\Delta(n-1)$ is less than 10% for our work. As the absolute temperature at the telescope never differs by more than 10% from the standard value, its effect can also be neglected. Similarly, variations in barometric pressure at any one site can be neglected as they are usually within 3 or 4 percent of the average value. However, the variation of pressure and refractive index with

altitude is appreciable, so we have adopted the relation

$$\Delta(n-1) = \Delta(n-1)_0 e^{-h/8000} , \qquad (7)$$

assuming a refractive scale height of 8 km. Finally, an uncertainty of 250 Ångstroms in the photographic wavelength corresponds to an uncertainty of about 10% in $\Delta(n-1)$.

Since the uncertainty in location of a typical scan is about 2", the systematic error in the refraction correction is obviously small compared to the random errors in the geometric data. In a typical case, the refraction error may amount to about 0.2".

The remaining fixed data consist of tables from the Astronomical Ephemeris. Three tables are required: the radial ephemeris (semidiameter and horizontal parallax, tabulated for every 0.5 day of E.T.); the geocentric angular ephemeris (apparent right ascension and declination, tabulated for every hour of E.T.); and the physical ephemeris (Earth's selenographic longitude and latitude, Sun's selenographic colongitude and latitude, and the position angle of the lunar axis, tabulated for 0^h U.T.).

Values required from the tables are interpolated to second differences by a subroutine which has special provisions for interpolating correctly across the discontinuity of 2π radians occurring in tabular values of angles that pass through zero without changing sign.

All data are checked for consistency and plausibility. No minutes or seconds greater than 60, no negative right

ascension, no declinations greater than 90° are acceptable. The tables must also agree as to month and year. As a final check, all fixed input data are printed out again so that a visual check can be made against the Ephemeris. However, since the input cards are punched in exactly the same format as the printed tables in the Ephemeris, errors are extremely unlikely.

At this point, the first block of the program is completed. We now take up the second block, which computes the hour angle (h) and declination (δ) of the detector for each photograph.

The input data for each photograph are the Universal Time and the orthographic lunar coordinates ξ and η of the intersection of the crosshairs, which is the optical conjugate of the detector. The Ephemeris Time, which is the argument of several tables, is computed from the Universal Time by adding the correction ΔT (currently 35 seconds).

The first step in finding the topocentric h and δ of the point photographed is to find the topocentric coordinates of the Moon's center--the topocentric librations. To do this, we first need the geocentric hour angle and declination of the center of the Moon, referred to the local meridian.

The geocentric right ascension and declination of the Moon's center, α_G and δ_G are interpolated from the tables, using the E.T. as argument. The geocentric hour angle is computed as

$$h_G = ST_0 + 1.00273791t - \lambda - \alpha_G \quad , \tag{8}$$

where ST_0 is the Greenwich Sidereal Time at 0^h U.T., 1.00273791 t is the sidereal time interval elapsed since 0^h U.T., converted from the U.T. day fraction in radians, t; and λ is the observer's longitude, measured positive West from Greenwich and converted to radians from the value in time units given in the Ephemeris. All conversion factors involving π are specified to 8 decimal digits.

At this point, the cosine of the geocentric zenith distance is computed:

$$\cos Z_G = \sin \delta_G \sin \phi + \cos \delta_G \cos \phi \cos h_G \tag{9}$$

If this value is negative, the Moon is below the horizon at the specified time; the program gives an error message and terminates. From $\cos Z_G$ we compute

$$\sin Z_G = (1 - \cos^2 Z_G)^{1/2} \quad , \tag{10}$$

which provides adequate accuracy since this value is used only to compute the differential corrections from geocentric to topocentric librations.

The topocentric librations are computed by Atkinson's method.[3]

We first compute the "topocentric parallax" π_T, i.e., the angle subtended at the center of the Moon between the observer and the center of the Earth; this angle represents the difference between the geocentric and the topocentric

lines of sight to the Moon's center. For this calculation we can neglect the flattening of the Earth; since the Moon is about 60 Earth radii away, the error in π_T is less than 1/297 x 1/60 $\cong$ 1/18000 radian. For our application, this error in the libration is reduced on the sky by an additional factor of about 240, since as seen from the Earth the Moon's radius is about 1/240 of a radian. Thus the error resulting from this approximation is about 2×10^{-7} radian, or 0.05", which can be neglected. All other approximations made by Atkinson in the formula for π_T produce smaller errors. The resulting formula for π_T is

$$\pi_T = \pi_G \sin Z_G(1 + 0.0168 \cos Z_G) \quad , \tag{11}$$

where π_G is the geocentric horizontal lunar parallax interpolated from the tables. Equation (11) is preferable to the form involving sin $2Z_G$, given in the Explanatory Supplement* (p. 324), because it uses a quantity already calculated and does not require the computation of another sine function value, which is relatively time consuming for the computer.

The sine and cosine of the parallactic angle Q are next found from Atkinson's formulae:

$$\sin Q = \sin h_G \cos \phi / \sin Z_G \quad , \tag{12}$$

$$\cos Q = (\sin \phi - \cos Z_G \sin \delta_G)/(\cos \delta_G \sin Z_G) \quad . \tag{13}$$

The angle Q is then found by an arctangent subroutine that accepts the sine and cosine as arguments, divides them to

*"Explanatory Supplement...", HMSO (1961).

get the tangent, and places the result in the proper quadrant. The geocentric position angle of the Moon's axis (C_G) is interpolated from the tables and the difference angle ($Q - C_G$) in Atkinson's formulae is computed.

The geocentric libration in latitude (the selenographic latitude of the Earth) b_G is interpolated from the tables, so that it can be used in finding the topocentric libration in longitude (the selenographic longitude of the observer), ℓ_T:

$$\Delta\ell = -\pi_T \sin(Q - C_G)/\cos b_G \quad , \tag{14}$$

$$\ell_T = \ell_G + \Delta\ell \quad , \tag{15}$$

dividing by $\cos b_G$ rather than multiplying by $\sec b_G$ as in the Explanatory Supplement, p. 324, is more efficient programming. Similarly, we have

$$b_T = b_G + \pi_T \cos(Q - C_G) \quad . \tag{16}$$

Atkinson's formulae are intended to give an accuracy of 0.01 degree on the Moon, which is about 0.15" on the sky as seen from the Earth. This is also the accuracy of the tables in the Ephemeris. Finally, the topocentric position angle of the lunar axis C_T is computed:

$$C_T = C_G + \sin b_T \, \Delta\ell - \pi_T \sin Q \sin \delta_G/\cos \delta_G \quad , \tag{17}$$

where the ratio $\sin \delta_G/\cos \delta_G$ is used in place of $\tan \delta_G$ because these values have already been computed. Atkinson

points out that the chief error here is in using $\tan \delta_G$ instead of $\tan(\delta_G + \delta_T/2)$. The resulting error in C_T is less than 2×10^{-4}, or again about 0.15" on the sky. Even if we have photographs from one limb only, the error at the opposite limb cannot exceed 0.3", which is clearly acceptable for our work.

The topocentric hour angle (h_T) and declination (δ_T) of the lunar center are then calculated, by use of the auxiliary quantities given on p. 60 of the Explanatory Supplement and two other auxiliary quantities.

$$
\begin{aligned}
A &= \cos \delta_G \cdot \sin h_G \\
B &= \cos \delta_G \cdot \cos h_G - \rho \cos \phi' \cdot \sin \pi_G \\
C &= \sin \delta_G \qquad\qquad - \rho \sin \phi' \cdot \sin \pi_G \\
D &= A^2 + B^2 \\
F &= (D + C^2)^{1/2} \\
S &= D^{1/2}
\end{aligned}
\tag{18}
$$

from which we obtain

$$h_T = \arctan(A/B) \tag{19}$$

and

$$\delta_T = \arctan(C/S) \quad . \tag{20}$$

The next problem is to find the topocentric coordinates h_P and δ_P of the photographed point with orthographic coordinates (ξ,η). We first assume the Moon is spherical, so that

$$\zeta = (1 - \xi^2 - \eta^2)^{1/2} \quad . \tag{21}$$

As the first step we convert (ξ, η, ζ) to axes (x, y, z) such that z lies along the line from the lunar center to the observer and the y,z-plane contains the lunar pole[4].

We first define the auxiliary quantity

$$c = \xi \sin \ell + \zeta \cos \ell \quad . \tag{22}$$

Then

$$\begin{aligned} x &= \xi \cos \ell - \zeta \sin \ell \quad , \\ y &= \eta \cos b - c \sin b \quad , \\ z &= \eta \sin b + c \cos b \quad . \end{aligned} \tag{23}$$

We next translate the origin to the observer, reverse the direction of z and rotate the x-and y-axes so that the new y-axis is in the topocentric hour circle passing through the lunar center and the new x-axis points East:

$$\begin{aligned} x' &= -x \cos C_T + y \sin C_T \quad , \\ y' &= x \sin C_T + y \cos C_T \quad , \\ z' &= R - z \quad , \end{aligned} \tag{24}$$

where

$$R = 3.670 \; F/\sin \pi_G \tag{25}$$

is the topocentric distance to the center of the Moon, in units of the lunar radius (3.670 is the length of the Earth's equatorial radius in lunar units).

We next rotate the z'-axis down to the celestial equator, using the relations

$$\sin \delta_T = C/F \quad ,$$
$$\cos \delta_T = S/F \quad , \tag{26}$$

and

$$X = x' \quad ,$$
$$Y = z' \sin \delta_T + y' \cos \delta_T \quad ,$$
$$Z = z' \cos \delta_T - y' \sin \delta_T \quad . \tag{27}$$

From these we readily find that

$$(\alpha_P - \alpha_T) = \arctan(X/Z) \tag{28}$$

and

$$\delta_P = \arctan[Y/(X^2 + Z^2)^{1/2}] \quad , \tag{29}$$

whence

$$h_P = h_T - (\alpha_P - \alpha_T) \quad . \tag{30}$$

This information suffices to determine the line of scan across the Moon. However, we need some additional geometric information for the interpretation of the data, and the refraction correction is not yet included. We first compute the air mass m by the relations

$$\cos Z_T = \sin \delta_T \sin \phi + \cos \delta_T \cos \phi \cos h_T \quad , \tag{31}$$

$$\sec Z_T = 1/\cos Z_T \quad , \tag{32}$$

and

$$m = \sec Z_T[1 - 0.0012(\sec^2 Z_T - 1)] \quad , \tag{33}$$

which is accurate to 0.002 at $Z_T = 75°$.

The differential refraction corrections are obtained by using the standard relations

$$h - h' = r \sec \delta \sin Q \quad ,$$

$$\delta - \delta' = -r \cos Q \quad , \tag{34}$$

where the primes denote the refracted coordinates and r is the refraction correction. In our case, we are correcting only for differential refraction, so that r is given by Eqs. (4) - (7). Combining these with Eqs. (12) and (13), and using topocentric instead of geocentric coordinates, we obtain

$$h'_P = h_P - r' \sin h_P \cos \phi \quad ,$$

$$\delta'_P = \delta_P + r'(\sin \phi - \cos Z_T \sin \delta_P) \quad , \tag{35}$$

where

$$r' = \Delta(n-1)\sec Z/\cos \delta \quad . \tag{36}$$

Equation (35) gives the topocentric hour angle and declination of the resolution element at the time of the photograph, corrected for differential refraction. We do not correct for the whole refraction because only the non-linear part of the change in refraction during a scan affects our results. On the assumption that the tangent term alone is a satisfactory representation, the second derivative of the refraction correction as a function of Z is $2(n - 1) \sec Z^2 \tan Z$. The error contributed by neglecting this term is $2(n - 1) \sec Z^2 \tan Z(\Delta Z)^2$; it amounts to about a second of arc for a scan one degree

long at $Z = 75°$, and decreases rapidly toward the zenith. In practice, the telescope moves only a fraction of a degree, or is stationary, during a scan, so that the curvature of the total refraction is not important. Ignoring the total refraction also simplifies the program by making accurate refraction corrections in both the second and third parts of the program unnecessary; only an approximate correction is needed for the second part, as explained above, and from this point on the refraction can be forgotten.

The only remaining task of the second part of the program is to compute the geometrical relations between the observer, the Sun, and the point observed. The angles required are the phase angle (the angle at the point observed between the line of sight and the direction of illumination), the elevations of the Sun and Earth (observer) above the lunar horizon at the point observed, and the difference in azimuth between Sun and observer.

These quantities are readily calculated in terms of vector dot products. Three vectors are involved: the lunar zenith, with orthographic components (ξ,η,ζ); the direction of the Sun, specified by its selenographic latitude and colongitude, and the direction of the observer. The vector (ξ,η,ζ) is already a unit vector, by Eq. (21). We construct unit vectors to the Sun and observer as follows:

The orthographic coordinates of the subsolar point are

$$\xi_\odot = \sin \ell_\odot \cos b_\odot \quad ,$$

$$\eta_\odot = \sin b_\odot \quad ,$$

$$\zeta_\odot = \cos \ell_\odot \cos b_\odot \quad , \tag{37}$$

where $\ell_\odot$ is obtained by subtracting the interpolated solar colongitude from $\pi/2$. These are also the components of the unit vector from the lunar center to the Sun, and hence (ignoring the solar parallax) the unit vector from the point photographed to the Sun.

To compute the vector from the point to the observer, we first obtain this vector in the (x,y,z) system:

$$x = -x'$$

$$y = y'$$

$$z = z' \quad . \tag{38}$$

We then convert to the lunar coordinate system, using the topographic librations and the auxiliary quantity c':

$$c' = z \cos b_T - y \sin b_T$$

$$\xi_E = (x \cos \ell_T + c' \sin \ell_T)/R'$$

$$\eta_E = (y \cos b_T + z \sin b_T)/R'$$

$$\zeta_E = (-x \sin \ell_T + c' \cos \ell_T)/R' \tag{39}$$

where

$$R' = (x^2 + y^2 + z^2)^{1/2}. \tag{40}$$

The cosine of the phase angle is then the dot product

$$\cos \theta = \xi_\odot \cdot \xi_E + \eta_\odot \cdot \eta_E + \zeta_\odot \cdot \zeta_E \quad . \tag{41}$$

The altitudes of Sun and observer are similarly given by the expressions

$$\cos(\pi/2 - a_\odot) = \xi \cdot \xi_\odot + \eta \cdot \eta_\odot + \zeta \cdot \zeta_\odot \qquad (42)$$

and

$$\cos(\pi/2 - a_E) = \xi \cdot \xi_E + \eta \cdot \eta_E + \zeta \cdot \zeta_\odot \quad . \qquad (43)$$

To find the separation in azimuth between Sun and observer, consider the spherical triangle whose vertices are the lunar zenith, $A(\xi,\eta,\zeta)$; the direction to the Sun, $B(\xi_\odot, \eta_\odot, \zeta_\odot)$; and the direction to the observer, $C(\xi_E, \eta_E, \zeta_E)$. Applying the law of cosines for side a, we have

$$\cos a = \cos b \cos c + \sin b \sin c \cos A \quad . \qquad (44)$$

Now, A is the azimuth angle required; cos a, cos b, and cos c are given by Eqs. (41) - (43), respectively; and sin b and sin c are readily calculated from the identity $\sin x = (1 - \cos x^2)^{1/2}$ since the cosines are known. Solving Eq. (44) for cos A, we have

$$\cos A = (\cos a - \cos b \cos c)/(\sin b \sin c), \qquad (45)$$

from which A is obtained by use of an arccosine subroutine.

This completes the calculations for the second block of the program. The results are converted to practical units (degrees instead of radians) and printed out. The program remembers the values of h'_P and δ'_P, and looks for another record of photographic data.

When all the photographs referring to a single scan have been analyzed in this manner, the program goes on to the third block.

The first problem is to determine the course of h'_p and δ'_p with time. In some cases, we know that the telescope has been held fixed, so that h'_p and δ'_p must be constant. In other cases, we know that the telescope was moved and that time-dependent terms must be included. Occasionally we are not certain whether the telescope was moving or not, and we must ask the program to decide on the basis of the available data. In general, we cannot assume that motion takes place in only one coordinate, even if only one axis of the telescope is moving; for the effects of differential refraction and polar-axis error* will in general produce a displacement in both coordinates.

We first compute the means of all the times, the h'_p's and the δ'_p's. For convenience, this means, together with the corresponding subsolar point and topocentric disk center (computed as described above), are printed out (Fig. 5a.). The differential variables

$$\begin{aligned} \Delta h &= h'_p - \bar{h} \quad , \\ \Delta \delta &= \delta'_p - \bar{\delta} \quad , \\ \Delta t &= t - \bar{t} \quad , \end{aligned} \tag{46}$$

are then computed for each photograph. If the telescope was known to be fixed, a control card sets a switch in the program and $\bar{h}$ and $\bar{\delta}$ are adopted for all times. The values

*We refer to the error in the alignment of the polar axis of the telescope.

of Δh and $\Delta\delta$ are then regarded as residuals. On the other hand, if the telescope was either known or suspected to be moving, equations of the form

$$\Delta h = \frac{dh}{dt}\Delta t \quad ,$$

$$\Delta\delta = \frac{d\delta}{dt}\Delta t \quad , \tag{47}$$

are fitted by least squares. Since all variables are measured from their means, no constant term is required and the least squares solution reduces to

$$\frac{dh}{dt} = \frac{\Sigma \Delta t \Delta h}{\Sigma (\Delta t)^2} \quad ,$$

$$\frac{d\delta}{dt} = \frac{\Sigma \Delta t \Delta \delta}{\Sigma (\Delta t)^2} \quad . \tag{48}$$

The residuals

$$\Delta h' = \Delta h - \frac{dh}{dt}\Delta t \quad ,$$

$$\Delta\delta' = \Delta\delta - \frac{d\delta}{dt}\Delta t \quad , \tag{49}$$

are then computed.

In a large-volume automatic data-reduction program it is extremely important to reject faulty data, since enormous residuals frequently result from errors in transcription and keypunching, dropped minus signs, digit transpositions, and the like. Therefore the residuals are scanned to see whether any point falls more than 10" from its calculated position. If no point falls outside this tolerance limit, normal processing continues. If one or more points

fall outside the rejection limit, the point with the largest residual in position $r^2 = [(\Delta h \cos \delta)^2 + \Delta\delta^2]$ is rejected, the residuals in both coordinates are printed with an error message, new means are taken of the remaining data, and the whole reduction process is repeated from that point on.

When a satisfactory set of residuals is obtained, the root-mean-square residual in position (both coordinates combined) is calculated and printed out, together with a graph of the residuals as a function of time (see Fig. 5b).

If the program has been asked to decide whether or not the telescope was moving, it uses the following precepts:

1) The calculation is originally carried out on the assumption of telescope motion.

2) If, after bad data are rejected, only one or two points remain, the telescope is assumed to have been stationary, on the grounds that no test of the significance of $\frac{dh}{dt}$ and $\frac{d\delta}{dt}$ is possible. The entire calculation from Eqs. (46) to (49) is repeated on this basis.

3) If three or more points remain after bad data are rejected, the significance criterion

$$q = \left(\frac{dh}{dt}\right)^2 + \left(\frac{d\delta}{dt}\right)^2 - \frac{v}{(n-1)\Sigma(\Delta t)^2} \qquad (50)$$

is evaluated, where

$$v = \Sigma r^2 \quad . \qquad (51)$$

The sum of the first two terms in Eq. 50 is the square

of the rate of telescope motion; the last term is the square of its standard deviation. If $q \leq 0$, the rate of motion is certainly not significant; the program concludes that the telescope was stationary, and the entire reduction beginning with Eq. (46) is repeated on this basis. If $q > 0$, the derived motion is accepted.

The last part of the program uses the equations

$$\Delta t = t - \bar{t} \quad ,$$
$$h = \bar{h} + \frac{dh}{dt}\Delta t \quad ,$$
$$\delta = \bar{\delta} + \frac{d\delta}{dt}\Delta t \quad , \tag{52}$$

to obtain the hour angle h, and declination δ, for each observation at time t. If the telescope was held fixed, $\frac{dh}{dt} = \frac{d\delta}{dt} = 0$. In principle, we require only an inversion of Eqs. (23) - (30), but there is a complication in determining where the line of sight intersects the (spherical) Moon.

To begin with, the topocentric librations and coordinates of the lunar center are computed by Eqs. (8) - (20) for the time t, exactly as previously described. Equation (25) gives the distance from the observer to the Moon's center, but <u>not</u> to the point where the line of sight intersects the Moon. We now compute the value

$$\Delta\alpha = h_T - h \tag{53}$$

and the direction cosines

$$X = \sin \Delta\alpha \cos \delta \quad ,$$

$$Y = \sin \delta \quad ,$$

$$Z = \cos \Delta\alpha \cos \delta \qquad (54)$$

These coordinates are referred to the topocentric meridian through the center of the Moon and the celestial equator. We rotate the Z-axis to the center of the Moon by

$$x' = X$$

$$y' = Y \cos \delta_T - Z \sin \delta_T$$

$$z' = Y \sin \delta_T + Z \cos \delta_T \qquad (55)$$

using Eqs. (26). We next convert these direction cosines to rectangular coordinates by setting $z' = R$:

$$x'' = x' \left(\frac{R}{z'}\right) \quad ,$$

$$y'' = y' \left(\frac{R}{z'}\right) \quad ,$$

$$z' = z' \left(\frac{R}{z'}\right) = R \quad . \qquad (56)$$

We now translate the origin to the center of the Moon and rotate about z to make the y, z-plane contain the lunar polar axis:

$$x = -x'' \cos C_T + y'' \sin C_T \quad ,$$

$$y = x'' \sin C_T + y'' \cos C_T \quad ,$$

$$z = R - z'' = 0 \quad . \qquad (57)$$

At this point, we have the rectangular coordinates of the point at which the line of sight intersects the plane passing through the center of the Moon and perpendicular to the line joining the observer to the center of the Moon. We wish to have the point at which the

line of sight intersects the unit sphere in this coordinate system, rather than the x,y-plane.

Clearly, the adopted arbitrary z-distance R is greater than the true distance from the observer to the point at which the line of sight intersects the lunar surface. If we express the true z-distance by

$$D = R(1 - \Delta) \quad , \tag{58}$$

then the correct values of x and y are

$$\begin{aligned} x_o &= x(1 - \Delta) \quad , \\ y_o &= y(1 - \Delta) \quad , \end{aligned} \tag{59}$$

and

$$z_o = R\Delta \quad . \tag{60}$$

The requirement that the Moon be spherical is

$$1 = x_o^2 + y_o^2 + z_o^2 = (1 - \Delta)^2 (x^2 + y^2) + \Delta^2 R^2 \quad . \tag{61}$$

If we write

$$r^2 = x^2 + y^2 \quad , \tag{62}$$

we have

$$\Delta^2 (r^2 + R^2) - 2\Delta r^2 + (r^2 - 1) = 0 \quad , \tag{63}$$

whose solution is

$$\Delta = \frac{r^2 \pm \sqrt{r^4 - (r^2 + R^2)(r^2 - 1)}}{r^2 + R^2} \quad . \tag{64}$$

The solution required is the one with the positive sign in this equation, since we want the largest value of Δ (the near side of the Moon). If we write

$$r_1 = r^2/R^2 \quad , \tag{65}$$

then

$$\Delta = \frac{r_1 + \sqrt{(r_1 + 1 - r^2)/R^2}}{1 + r_1} \quad . \tag{66}$$

Since $r_1 \leq 2 \times 10^{-5}$ and Δ is of the same order, and we need at most an accuracy of 10^{-4} in Δ, we can drop terms of order r_1^2 and take the value

$$\Delta \approx r_1 + \sqrt{(r_1 + 1 - r^2)/R^2} \quad . \tag{67}$$

We cannot drop the r_1 inside the radical, because near the limb $1 - r^2 \approx 0$ and the value of the radical, like r_1, is of order $1/R^2$.

The radicand

$$r_2 = (r_1 + 1 - r^2)/R^2 \tag{68}$$

also provides a critical test, for if the line of sight does not intersect the Moon, $r_2 < 0$. Therefore the criterion r_2 is calculated first and, if $r_2 > 0$, the value of

$$\Delta = r_1 + \sqrt{r_2} \tag{69}$$

is used to obtain x_o, y_o, and z_o from Eqs. (59) and (60).

If $r_2 < 0$ the calculation is stopped, and a message is printed to indicate that the detector was located off the lunar disk.

The remaining transformation to orthographic lunar coordinates uses the auxiliary quantity

$$c = z_o \cos b_T - y_o \sin b_T \quad . \tag{70}$$

We then have for the coordinates of the detector at the time t, the values

$$\xi = x_o \cos \ell_T + c \sin \ell_T \quad ,$$

$$\eta = y_o \cos b_T + z_o \sin b_T \quad ,$$

$$\zeta = c \cos \ell_T - x_o \sin \ell_T \quad . \tag{71}$$

The auxiliary geometrical quantities referring to the relative positions of Earth and Sun are calculated from Eqs. (37) - (45) just as they were for each photographed point. The results are printed and also punched on cards for further analysis. Figures 5a, b, c show the printed computer output for a typical scan during the eclipse of December 18-19, 1964. Radiometric data from this scan are discussed later.

LUNAR SCAN GEOMETRY

1964 DEC U.T.				FRAME NO.	XI	ETA	HOUR ANGLE	DECLINATION	AIR MASS	ELEVATION OF EARTH	ELEVATION OF SUN	EARTH AZIMUTH FROM SUN	PHASE ANGLE	SCAN NO.
D	H	M	S											
19	1	21	50.18	181	0.828	0.178	-3 19 27.2	23 19 11.2	1.419	31.6	32.0	0.2	0.5	37
19	1	22	11.26	182	0.547	0.183	-3 19 27.4	23 19 18.7	1.419	54.3	54.6	0.4	0.4	37
19	1	22	34.21	183	0.242	0.177	-3 19 27.8	23 19 15.0	1.419	72.2	72.4	0.8	0.3	37
19	1	22	55.18	184	-0.032	0.177	-3 19 27.8	23 19 17.0	1.419	79.7	79.6	1.0	0.2	37

NOTE -- 'EARTH' MEANS OBSERVER (AGASSIZ STA)

COORDINATES AT MID-SCAN, 1 22 22.7 U.T.

SUBSOLAR POINT XI	SUBSOLAR POINT ETA	CENTER OF DISC XI	CENTER OF DISC ETA	HOUR ANGLE H M S	DECLINATION ° ' "
-0.002	-0.002	-0.006	0.001	-3 19 27.5	23 19 15.4
DIFFERENTIAL REFRACTION CORRECTIONS				0.1	0.5

R.M.S. RESIDUAL IN POSITION 4.76 ARCSEC FROM DRIFT

RESIDUALS IN H.A. (H) AND DEC (D) FOLLOW

FIG. 5a. Computer read-out of the astrometric analysis of the photographs of a scan during the eclipse of December 18-19, 1964.

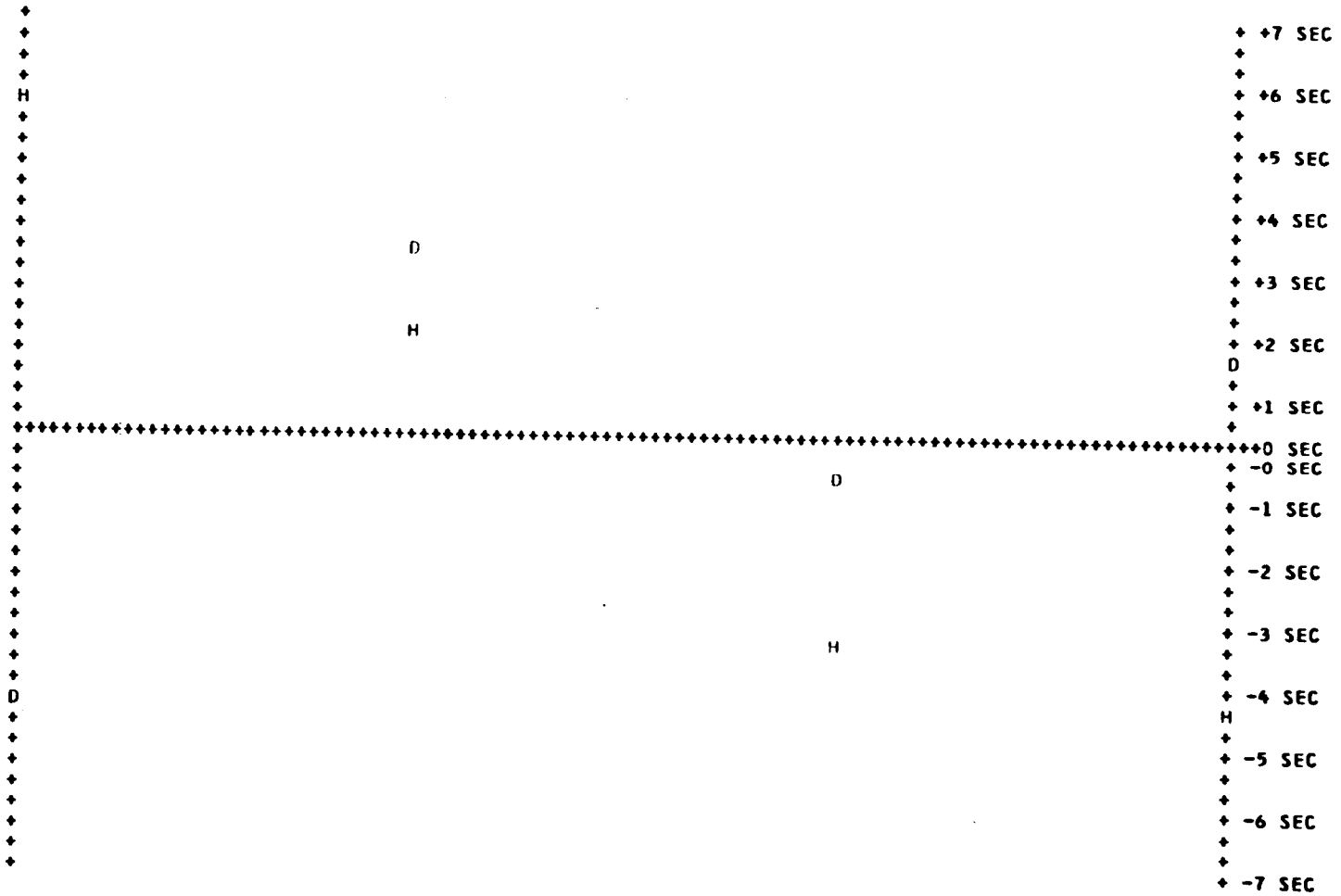

FIG. 5b. Plot of the residuals in Hour Angle and Declination as a function of time.

EPHEMERIS FOR SCAN 37, USING DRIFT METHOD BASED ON 4 POINTS.

1964 DEC U.T. D	H	M	S	XI	ETA	AIR MASS	ELEVATION OF EARTH	ELEVATION OF SUN	EARTH AZIMUTH FROM SUN	PHASE ANGLE	
19	1	21	37.51	0.989	0.185	1.419	0.	0.	0.	0.	OFF LIMB
19	1	21	37.72	0.986	0.185	1.419	0.	0.	0.	0.	OFF LIMB
19	1	21	37.92	0.984	0.185	1.419	0.	0.	0.	0.	OFF LIMB
19	1	21	38.13	0.981	0.185	1.419	0.	0.	0.	0.	OFF LIMB
19	1	21	38.33	0.978	0.185	1.419	0.	0.	0.	0.	OFF LIMB
19	1	21	38.54	0.981	0.184	1.419	3.1	3.6	0.2	0.5	
19	1	21	38.74	0.978	0.184	1.419	5.2	5.7	0.2	0.5	
19	1	21	38.90	0.975	0.184	1.419	6.4	6.9	0.2	0.5	
19	1	21	39.10	0.972	0.184	1.419	7.7	8.1	0.2	0.5	
19	1	21	39.36	0.969	0.184	1.419	8.9	9.4	0.2	0.5	
D	H	M	S								
19	1	24	3.33	-0.913	0.171	1.419	21.8	21.8	0.1	0.1	
19	1	24	3.59	-0.917	0.171	1.419	21.3	21.3	0.1	0.1	
19	1	24	3.79	-0.919	0.171	1.419	20.9	20.9	0.1	0.1	
19	1	24	3.95	-0.921	0.171	1.419	20.5	20.6	0.1	0.1	
19	1	24	4.15	-0.924	0.171	1.419	20.1	20.2	0.1	0.1	
19	1	24	4.36	-0.926	0.171	1.419	19.7	19.7	0.1	0.1	
19	1	24	4.56	-0.929	0.171	1.419	19.2	19.3	0.1	0.1	
19	1	24	4.77	-0.932	0.171	1.419	18.7	18.8	0.1	0.1	
19	1	24	4.97	-0.935	0.171	1.419	18.3	18.3	0.1	0.1	
19	1	24	5.13	-0.937	0.171	1.419	17.9	17.9	0.1	0.1	
19	1	24	5.33	-0.939	0.171	1.419	17.4	17.5	0.1	0.1	
19	1	24	5.54	-0.942	0.171	1.419	16.9	17.0	0.1	0.1	
19	1	24	5.74	-0.944	0.171	1.419	16.4	16.4	0.1	0.1	
19	1	24	5.95	-0.947	0.171	1.419	15.8	15.9	0.1	0.1	
19	1	24	6.15	-0.950	0.171	1.419	15.3	15.3	0.1	0.1	
19	1	24	6.41	-0.953	0.171	1.419	14.5	14.6	0.1	0.1	
19	1	24	6.56	-0.955	0.171	1.419	14.1	14.1	0.1	0.1	
19	1	24	6.77	-0.958	0.171	1.419	13.4	13.5	0.1	0.1	
19	1	24	6.97	-0.961	0.171	1.419	12.7	12.8	0.1	0.1	
19	1	24	7.18	-0.963	0.171	1.419	12.0	12.1	0.1	0.1	
19	1	24	7.38	-0.966	0.171	1.419	11.3	11.4	0.1	0.1	
19	1	24	7.59	-0.969	0.171	1.419	10.5	10.6	0.1	0.1	
19	1	24	7.79	-0.971	0.171	1.419	9.6	9.7	0.1	0.1	
19	1	24	8.00	-0.974	0.171	1.419	8.7	8.7	0.1	0.1	
19	1	24	8.21	-0.977	0.171	1.419	7.6	7.7	0.1	0.1	
19	1	24	8.41	-0.979	0.171	1.419	6.3	6.4	0.1	0.1	
19	1	24	8.62	-0.982	0.171	1.419	4.8	4.8	0.1	0.1	
19	1	24	8.77	-0.984	0.171	1.419	3.2	3.3	0.1	0.1	
19	1	24	8.97	-0.987	0.171	1.419	0.	0.	0.	0.	OFF LIMB
19	1	24	9.18	-0.989	0.171	1.419	0.	0.	0.	0.	OFF LIMB
19	1	24	9.38	-0.992	0.171	1.419	0.	0.	0.	0.	OFF LIMB
19	1	24	9.59	-0.995	0.171	1.419	0.	0.	0.	0.	OFF LIMB
19	1	24	9.79	-0.998	0.171	1.419	0.	0.	0.	0.	OFF LIMB
19	1	24	10.00	-1.000	0.171	1.419	0.	0.	0.	0.	OFF LIMB
19	1	24	10.21	-1.003	0.171	1.419	0.	0.	0.	0.	OFF LIMB
19	1	24	10.41	-1.006	0.171	1.419	0.	0.	0.	0.	OFF LIMB
19	1	24	10.62	-1.008	0.171	1.419	0.	0.	0.	0.	OFF LIMB
19	1	24	10.82	-1.011	0.171	1.419	0.	0.	0.	0.	OFF LIMB

FIG. 5c. Sample of the astrometric reduction of data points near each limb. All the computations pertain to the observational data shown in Figure 7a, b.

V. Temperature Measurements

The equations that we will use to reduce our radiant power measurements into actual temperatures are obtained for the radiation pyrometer developed at Harvard College Observatory, but our general conclusions will apply to the technique more than to the specific instrument. To obtain the heat transfer equations we refer to Figure 6 which shows a schematic of the radiation pyrometer. The calibration blackbody is introduced only during the calibration periods.

When the chopper closes the entrance stop of the reference blackbody, the detector will exchange radiation with the reference blackbody by reflection on the gold-coated side of the chopper. Under this condition the irradiance on the detector flake is

$$S_R = (1 - \bar{\rho}_G)S(T_G) + \bar{\rho}_G[\bar{\varepsilon}_R S(T_R) + (1 - \bar{\varepsilon}_R)S(T_F)] \quad , \quad (72)$$

where

$$S(T) = \int_0^\infty N_\lambda(T)\tau_F(\lambda)\tau_D(\lambda)\varepsilon_D(\lambda)d\lambda \quad , \quad (73)$$

and

$N_\lambda(T)$ = spectral irradiance of a blackbody at temperature T,

$\tau_F(\lambda)$ = spectral transmittance of the filters,

$\tau_D(\lambda)$ = spectral transmittance of the detector's window,

$\varepsilon_D(\lambda)$ = spectral emittance of the detector (thermal detector),

$\bar{\rho}_G$ = radiant reflectance of the gold mirror,

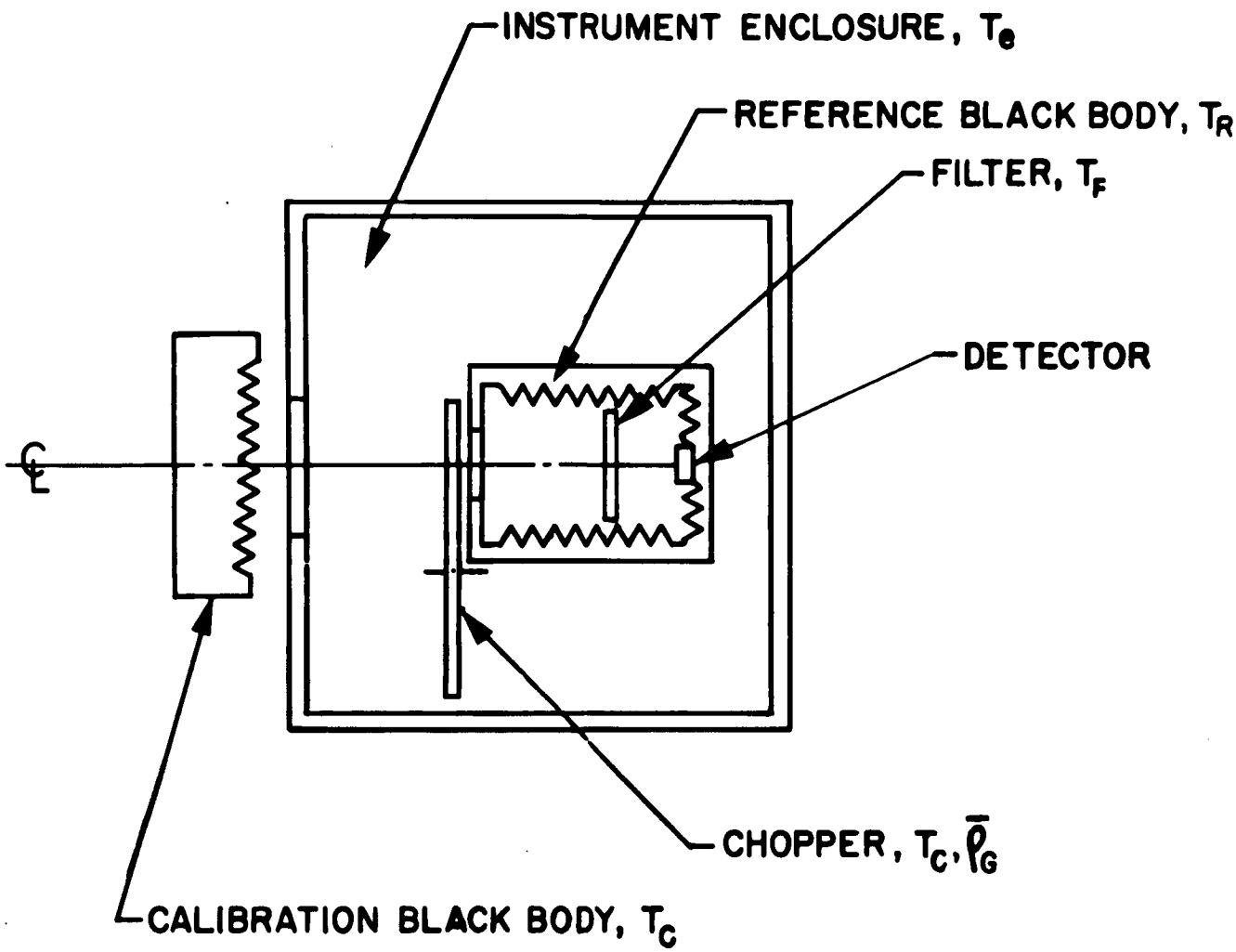

FIG. 6. Heat transfer equations are obtained from this simplified schematic diagram of the radiation pyrometer.

T_G = temperature of the chopper,

T_R = temperature of the reference blackbody,

T_F = temperature of the filter slide,

$\bar{\varepsilon}_R$ = radiant emissivity of the reference blackbody.

The first term in Eq. (72) represents the emission from the gold mirror; the second, the emission from the reference blackbody; and the third, the emission from the filter slide reflected by the walls of the reference blackbody.

When the chopper opens, the detector will exchange radiation with the calibration blackbody. The irradiance on the detector is then

$$S_o = \bar{\varepsilon}_c S(T_c) + (1 - \bar{\varepsilon}_c) S(T_e) \quad , \tag{74}$$

where

$\bar{\varepsilon}_c$ = radiant emissivity of the calibration blackbody,

T_c = temperature of the calibration blackbody,

T_e = temperature of the instrument enclosure.

The first term represents the emission from the calibration blackbody, and the second represents the environmental radiation reflected by it.

The net calibration signal is the difference

$$S_c = S_o - S_R \quad . \tag{75}$$

If all parts of the instrument are at the same temperature, $T_G = T_R = T_F = T_e$. Replacing all these symbols

by T_R, we find that Eq. (72) reduces to

$$S_R = S(T_R) \quad , \tag{76}$$

and Eq. (74) becomes

$$S_o = \bar{\varepsilon}_c S(T_c) + (1 - \bar{\varepsilon}_c) S(T_R) \quad . \tag{77}$$

Substituting these values into Eq. (75) we obtain

$$S_c = \bar{\varepsilon}_c [S(T_c) - S(T_R)] \quad . \tag{78}$$

In general, T_G, T_R, T_F, and T_e will all be slightly different. If the differences are small, we may expand S(T) in a Taylor series about T_R and retain only the first-order term:

$$S(T) = S(T_R) + \frac{dS}{dT_R} (T - T_R) \quad . \tag{79}$$

Substituting (79) into Eqs. (72) and (74), and applying Eq. (75), we find that

$$S_c = \bar{\varepsilon}_c [S(T_c) - S(T_R)] + \frac{dS}{dT_R} [(1 - \bar{\varepsilon}_c)(T_e - T_R)$$

$$- (1 - \bar{\rho}_G)(T_G - T_R) - \bar{\rho}_G (1 - \bar{\varepsilon}_R)(T_F - T_R)] . \tag{80}$$

The term in dS/dT_R represents the error incurred by using Eq. (78) and neglecting the temperature differences between different parts of the instrument. The relative error of this approximation is obtained by dividing Eq. (80) by Eq. (78):

$$\frac{\Delta S_c}{S_c} = \frac{1}{\bar{\varepsilon}_c [S(T_c) - S(T_R)]} \frac{dS}{dT_R} \quad . \tag{81}$$

To get an idea of the size of $\Delta S_c / S_c$ it is sufficient to extend the approximation (79) to T_c; we then have

$$\frac{\Delta S_c}{S_c} = \frac{1}{\bar{\varepsilon}_c} \left| (1 - \bar{\varepsilon}_c) \frac{(T_e - T_R)}{(T_c - T_R)} - (1 - \bar{\rho}_G) \frac{(T_G - T_R)}{(T_c - T_R)} \right.$$

$$\left. - \bar{\rho}_G (1 - \bar{\varepsilon}_R) \frac{(T_F - T_R)}{(T_c - T_R)} \right| \quad . \tag{82}$$

We can estimate the maximum possible error by placing absolute value signs around each term. Typical values may be $|T_e - T_R|$ $|T_G - T_R|$ $|T_F - T_R|$ 1°K, and $(T_c - T_R)$ 10°K. For our instrument, $\bar{\varepsilon}_c = 0.96$, $\bar{\rho}_G = 0.99$, $\bar{\varepsilon}_R = 0.98$, so that

$$\frac{\Delta S_c}{S_c} \leq 0.7\% \quad . \tag{83}$$

In fact, if $T_F = T_e$, then $|\Delta S_c / S_c| \leq 0.3\%$. This source of error in calibration is so small that we shall neglect it and adopt the relation (78) for the rest of the discussion.

The radiance received from the Moon is given by

$$S_M = S_{M+S} - S_S = \bar{\varepsilon}_M \bar{\rho}_A^2 \left(\frac{F_c}{F_{eff}} \right)^2 \bar{\tau}_A(m, T_M) S(T_M) \quad , \tag{84}$$

where

$\bar{\varepsilon}_M$ = radiant emissivity of the Moon,

$\bar{\rho}_A$ = reflectance of the aluminum telescope mirrors,

$\left(F_c/F_{eff}\right)^2$ = ratio of the solid angles of Moon and calibration blackbody seen by the detector; i.e., the F's are the effective f-numbers for the calibration blackbody and the Moon,

$\bar{\tau}_A(m,T_M)$ = atmospheric radiant transmittance for radiation at temperature T_M through m air masses (see Chapter VI).

If we record the power signals and designate the amplitudes d_S, d_{M+S}, and d_c as sky, Moon plus sky, and calibration, and combine Eqs. (78) and (84), we obtain:

$$S(T_M) = \frac{F_{eff}^{\,2}\,(d_{M+S}-d_S)\,\bar{\varepsilon}_c}{F_c^{\,2}\,d_c\,\bar{\rho}_A^{\,2}\,\bar{\varepsilon}_M\,\bar{\tau}_A(m,T_M)}\left[S(T_c) - S(T_R)\right] \quad . \tag{85}$$

Equation (85) is the basic relationship by which to reduce the power measurements into actual values of lunar temperature.

a) Error Analysis in Absolute Measurements

Let us examine the accuracy with which some of the instrumental parameters can be measured, and the maximum error we should expect in the absolute measurement of the temperature.

Equation (85) expresses the radiance on the detector due to the Moon's signal and can be written as:

$$AT_M^{\,B} = S(T_M) \quad , \tag{86}$$

where A and B are constants for a small range in T_M.

From Eq. (86) we obtain

$$B = \frac{dS(T_M)}{dT_M}\left(\frac{T_M}{S(T_M)}\right), \tag{87}$$

and

$$\frac{\Delta T_M}{T_M} = \left[\frac{S(T_M)}{T_M}\left(\frac{dT_M}{dS(T_M)}\right)\right]\frac{\Delta S(T_M)}{S(T_M)} . \tag{88}$$

From Eq. (85) we obtain the expression for $\Delta S(T_M)/S(T_M)$ which, introduced into Eq. (88), gives the following expression for the maximum error:

$$\left|\frac{\Delta T_M}{T_M}\right| = \left[\left(\frac{S(T_M)}{T_M}\right)\frac{dT_M}{dS(T_M)}\right]\left[2\left|\frac{\Delta F_{eff}}{F_{eff}}\right| + 2\left|\frac{\Delta F_c}{F_c}\right|\right.$$

$$+ \left|\frac{\Delta(d_{M+S} - d_S)}{(d_{M+S} - d_S)}\right| + \left|\frac{\Delta d_c}{d_c}\right| + 2\left|\frac{\Delta\bar{\rho}_A}{\bar{\rho}_A}\right| + \left|\frac{\Delta\bar{\varepsilon}_M}{\bar{\varepsilon}_M}\right|$$

$$+ \left|\frac{\Delta\bar{\tau}_A(m,T_M)}{\bar{\tau}_A(m,T_M)}\right| + \left|\frac{\Delta\bar{\varepsilon}_c}{\bar{\varepsilon}_c}\right| + \left|\left(\frac{dS(T_c)}{dT_c}\right)\frac{\Delta T_c}{S(T_c) - S(T_R)}\right|$$

$$\left. + \left|\left(\frac{dS(T_R)}{dT_c}\right)\frac{\Delta T_R}{S(T_c) - S(T_R)}\right|\right] . \tag{89}$$

To compute the coefficients of propagation of errors we will assume $T_M = 400°K$ and the observing conditions to be $T_R = 260°K$ and $T_c = 270°K$.

Introducing the proper values into Eq. (89) we obtain

$$\left|\frac{\Delta T_M}{T_M}\right| = \left[0.56\left|\frac{\Delta F_{eff}}{F_{eff}}\right| + 0.56\left|\frac{\Delta F_c}{F_c}\right| + 0.28\left|\frac{\Delta(d_{M+S} - d_S)}{d_{M+S} - d_S}\right| \right.$$

$$+ 0.28\left|\frac{\Delta d_c}{d_c}\right| + 0.56\left|\frac{\Delta \bar{\rho}_A}{\bar{\rho}_A}\right| + 0.28\left|\frac{\Delta \bar{\varepsilon}_M}{\bar{\varepsilon}_M}\right| + 0.28\left|\frac{\Delta \bar{\tau}_A(m,T_M)}{\bar{\tau}_A(m,T_M)}\right|$$

$$\left. + 0.28\left|\frac{\Delta \bar{\varepsilon}_c}{\bar{\varepsilon}_c}\right| + 0.029|\Delta T_c| + 0.026|\Delta T_R| \right] \quad . \qquad (90)$$

To bracket the error we refer to Table I, which gives the estimated maximum errors in the measurements of the instrumental parameters, the observing conditions, and the data reduction process. The second row in Table I gives the probable errors in the measurements of the same quantities under good observational conditions.

Introducing the proper values into Eq. (90), we obtain

$$\frac{\Delta T_M}{T_M} = \pm 13\%$$

or (91)

$$T_M = \pm 53^\circ K \quad ,$$

which is the <u>maximum</u> error to be expected near the subsolar point under good instrumental and observational conditions. This analysis applies only for signals with very high signal-to-noise ratio.

By taking the square root of the sum of the squares

TABLE I

	$\frac{\Delta F_{eff}}{F_{eff}}$	$\frac{\Delta F_c}{F_c}$	$\frac{\Delta(d_{M+S}-d_s)}{d_{M+S}-d_s}$		$\frac{\Delta d_c}{d_c}$	$\frac{\Delta \bar{\rho}_A}{\bar{\rho}_A}$	$\frac{\Delta \bar{\epsilon}_M}{\bar{\epsilon}_M}$	$\frac{\Delta \bar{\tau}_A(m,400)}{\bar{\tau}_A(m,400)}$	$\frac{\Delta \bar{\tau}_A(m,175)}{\bar{\tau}_A(m,175)}$	$\frac{\Delta \bar{\epsilon}_c}{\bar{\epsilon}_c}$	ΔT_c	ΔT_R
			(T=400°K)	(T=175°K)								
Maximum Error	±4%	±2%	±1%	±20%	±1%	±5%	±5%	±10%	±12%	±3%	±0.3°K	±0.3°K
Probable Error	±2%	±1%	±1%	±10%	±1%	±2%	±3%	±3%	±5%	±1%	±0.1°K	±0.1°K

of the terms in Eq. (90), we can estimate the size of the systematic error to be expected under these conditions. We now take from the Table I the estimated probable errors, and find that our determination of the subsolar point temperature is as likely as not to be systematically in error by ± 2.1%, or ± 8.5°K.

For T_M = 175°K, typical of temperatures on the eclipsed Moon, the factor $\left[\frac{S(T_M)}{T_M}\left(\frac{dT_M}{dS(T_M)}\right)\right]$ is reduced from 0.28 to 0.13. On the other hand, the atmospheric transmittance is somewhat more uncertain for such low-temperature radiation, and instrumental noise introduces an additional uncertainty in the measured signal $(d_{M+S} - d_S)$. Allowing for these two effects, we estimate that the maximum error of one measurement at 175°K, including a 20% instrumental noise contribution, is ± 15°K, while the probable systematic error of the mean of 10 data points is ± 2.1°K.

b) Error Analysis in Relative Measurements

Let us assume that we want to measure the ratio of the temperatures of two areas of the Moon; temperature ratios are usually used in studying the heating and cooling of the surface during a lunation and during eclipse.

If we write

$$R = \frac{T_1}{T_2} \quad , \tag{92}$$

then

$$\log R = \log T_1 - \log T_2 \tag{93}$$

and

$$\frac{\Delta R}{R} = \frac{\Delta T_1}{T_1} - \frac{\Delta T_2}{T_2} \quad . \tag{94}$$

The ratio $\Delta T/T$ has been evaluated in Eq. (89). If we write

$$D(T) = \frac{S(T)}{T} \left(\frac{dT}{dS}\right) \quad , \tag{95}$$

then Eq. (88) becomes

$$\frac{\Delta T}{T} = D(T) \left(\frac{\Delta S(T)}{S(T)}\right) \quad . \tag{96}$$

We now substitute Eq. (96) into Eq. (94), and writing out $\Delta S(T)/S(T)$ explicitly and rearranging terms, we have the general expression:

$$\left|\frac{\Delta R}{R}\right| = \left|D(T_1) - D(T_2)\right| \left[2\left|\frac{\Delta F_{eff}}{F_{eff}}\right| + 2\left|\frac{\Delta F_c}{F_c}\right| + 2\left|\frac{\Delta \bar{\rho}_A}{\bar{\rho}_A}\right| + \left|\frac{\Delta \bar{\varepsilon}_c}{\bar{\varepsilon}_c}\right|\right]$$

$$+ D(T_1)\left[\left|\frac{\Delta(d_{M+S} - d_S)_1}{(d_{M+S} - d_S)_1}\right| + \left|\frac{\Delta d_{c,1}}{d_{c,1}}\right| + \left|\frac{\Delta \bar{\varepsilon}_{M,1}}{\bar{\varepsilon}_{M,1}}\right|\right.$$

$$+ \left|\frac{\Delta \bar{\tau}_A(m_1;T_{M,1})}{\bar{\tau}_A(m_1;T_{M,1})}\right| + \left|\left(\frac{dS(T_{c,1})}{dT_{c,1}}\right)\frac{\Delta T_{c,1}}{S(T_{c,1}) - S(T_{R,1})}\right|$$

$$\left. + \left|\left(\frac{dS(T_{R,1})}{dT_{R,1}}\right)\frac{\Delta T_{R,1}}{S(T_{c,1}) - S(T_{R,1})}\right|\right] + D(T_2)\left[\left|\frac{\Delta(d_{M+S} - d_S)_2}{(d_{M+S} - d_S)_2}\right|\right.$$

$$+ \left|\frac{\Delta d_{c,2}}{d_{c,2}}\right| + \left|\frac{\Delta \bar{\varepsilon}_{M,2}}{\bar{\varepsilon}_{M,2}}\right| + \left|\frac{\Delta \bar{\tau}_A(m_2;T_{M,2})}{\bar{\tau}_A(m_2;T_{M,2})}\right|$$

$$\left. + \left|\left(\frac{dS(T_{c,2})}{dT_{c,2}}\right)\frac{\Delta T_{c,2}}{S(T_{c,2}) - S(T_{R,2})}\right| + \left|\left(\frac{dS(T_{R,2})}{dT_{R,2}}\right)\frac{\Delta T_{R,2}}{S(T_{c,2}) - S(T_{R,2})}\right|\right] . \quad (97)$$

For a typical eclipse cooling curve with $T_1 = 175°K$ and $T_2 = 400°K$ and $T_R = 260°K$ and $T_c = 270°K$, we obtain the coefficients of propagation of errors for Eq. (97):

$$\left|\frac{\Delta R}{R}\right| = 0.30\left|\frac{\Delta F_{eff}}{F_{eff}}\right| + 0.30\left|\frac{\Delta F_c}{F_c}\right| + 0.30\left|\frac{\Delta \bar{\rho}_A}{\bar{\rho}_A}\right| + 0.15\left|\frac{\Delta \bar{\varepsilon}_c}{\bar{\varepsilon}_c}\right|$$

$$+ 0.28\left|\frac{\Delta(d_{M+S} - d_S)_1}{(d_{M+S} - d_S)_1}\right| + 0.28\left|\frac{\Delta d_{c,1}}{d_{c,1}}\right| + 0.28\left|\frac{\Delta \bar{\varepsilon}_{M,1}}{\bar{\varepsilon}_{M,1}}\right|$$

$$+ 0.28\left|\frac{\Delta \bar{\tau}_A(m_1;T_{M,1})}{\bar{\tau}_A(m_1;T_{M,1})}\right| + 0.029\left|\Delta T_{c,1}\right| + 0.026\left|\Delta T_{R,1}\right|$$

$$+ 0.13\left|\frac{\Delta(d_{M+S} - d_S)_2}{(D_{M+S} - d_S)_2}\right| + 0.13\left|\frac{\Delta d_{c,2}}{d_{c,2}}\right| + 0.13\left|\frac{\Delta \bar{\varepsilon}_{M,2}}{\bar{\varepsilon}_{M,2}}\right|$$

$$+ 0.13\left|\frac{\Delta \bar{\tau}_A(m_2;T_{M,2})}{\bar{\tau}_A(m_2;T_{M,2})}\right| + 0.014\left|\Delta T_{c,2}\right| + 0.012\left|\Delta T_{R,2}\right| \quad . \quad (98)$$

The maximum error in $\Delta R/R$ is $\pm$ 16%, and the probable error is $\pm$ 2.2% if we assume the values in Table I. These figures are slightly too pessimistic because the systematic errors in atmospheric radiant transmittance and in calibration are likely to be in the same direction during one night, and should probably be put into the first term of Eq. (97) rather than be separated into the second and third terms.

In the case of observations made in a single scan to determine the brightness profile of the Moon, the same calibration will apply to all parts of the scan, and the atmospheric transmittance errors are likely to be in the same

direction at all temperatures. Putting these terms into the $|D(T_1) - D(T_2)|$ term, we have

$$\left|\frac{\Delta R}{R}\right| = |D(T_1) - D(T_2)| \left[2\left|\frac{\Delta F_{eff}}{F_{eff}}\right| + 2\left|\frac{\Delta F_c}{F_c}\right| + 2\left|\frac{\Delta \bar{\rho}_A}{\bar{\rho}_A}\right| + \left|\frac{\Delta \bar{\varepsilon}_c}{\bar{\varepsilon}_c}\right| \right.$$

$$+ \left|\frac{\Delta d_c}{d_c}\right| + \left|\frac{\Delta \bar{\tau}_A(m;T_{M,1})}{\bar{\tau}_A(m;T_{M,1})}\right| + \left| \left(\frac{dS(T_c)}{dT_c}\right) \frac{\Delta T_c}{S(T_c) - S(T_R)} \right|$$

$$\left. + \left| \left(\frac{dS(T_R)}{dT_R}\right) \frac{\Delta T_R}{S(T_c) - S(T_R)} \right| \right]$$

$$+ |D(T_1) + D(T_2)| \left[\left|\frac{\Delta(d_{M+S} - d_S)}{(d_{M+S} - d_S)}\right| + \left|\frac{\Delta \bar{\varepsilon}_M}{\bar{\varepsilon}_M}\right| \right] . \qquad (99)$$

Taking $T_1 = 250°K$ and $T_2 = 400°K$ we have

$$\left|\frac{\Delta R}{R}\right| = 0.19\left|\frac{\Delta F_{eff}}{F_{eff}}\right| + 0.19\left|\frac{\Delta F_c}{F_c}\right| + 0.19\left|\frac{\Delta \bar{\rho}_A}{\bar{\rho}_A}\right| + 0.094\left|\frac{\Delta \bar{\varepsilon}_c}{\bar{\varepsilon}_c}\right|$$

$$+ 0.094\left|\frac{\Delta d_c}{d_c}\right| + 0.094\left|\frac{\Delta \bar{\tau}_A(m,T)}{\bar{\tau}_A(m,T)}\right| + 0.010|\Delta T_c|$$

$$+ 0.009|\Delta T_R| + 0.46\left|\frac{\Delta(d_{M+S} - d_S)}{d_{M+S} - d_S}\right| + 0.46\left|\frac{\Delta \bar{\varepsilon}_M}{\bar{\varepsilon}_M}\right| . \qquad (100)$$

Adopting the usual values for high temperatures, we find that the maximum relative error is $\pm$ 6.7%, and the probable error is $\pm$ 1.6%. Finally, for observations made over both a short time-interval and a very small temperature-range (say 10°K), we can neglect $|D(T_1) - D(T_2)|$, and we have

$$\left|\frac{\Delta R}{R}\right| = D(T_M)\left[2\left|\frac{\Delta(d_{M+S} - d_S)}{d_{M+S} - d_S}\right| + 2\left|\frac{\Delta\bar{\varepsilon}_M}{\bar{\varepsilon}_M}\right|\right] \quad . \tag{101}$$

Setting $T_M = 400°K$, we find

$$\left|\frac{\Delta R}{R}\right| = 0.56\left|\frac{\Delta(d_{M+S} - d_S)}{d_{M+S} - d_S}\right| + 0.56\left|\frac{\Delta\bar{\varepsilon}_M}{\bar{\varepsilon}_M}\right| \quad , \tag{102}$$

which gives maximum and probable relative errors of $\pm$ 3.4% and $\pm$ 1.8%, assuming the values in Table I. We note that most of the uncertainty comes from possible variations in lunar emissivity.

Often we wish to deal with temperature <u>differences</u> in such cases. We can write

$$T_1 - T_2 = T_2\left[\left(\frac{T_1}{T_2}\right) - 1\right] = T_2(R - 1) \quad . \tag{103}$$

The error in $(T_1 - T_2)$ is then

$$\Delta(T_1 - T_2) = |T_2 \Delta R| + |(R - 1)\Delta T_2|$$

$$= T_2 D(T_2) \left[2 \left| \frac{\Delta(d_{M+S} - d_S)}{d_{M+S} - d_S} \right| + 2 \left| \frac{\Delta \bar{\varepsilon}_M}{\bar{\varepsilon}_M} \right| \right] + |(R - 1)\Delta T_2| \quad ; \tag{104}$$

at $T_2 = 400°K$, this becomes

$$\Delta(T_1 - T_2) = 222 \left| \frac{\Delta(d_{M+S} - d_S)}{d_{M+S} - d_S} \right| + 222 \left| \frac{\Delta \bar{\varepsilon}_M}{\bar{\varepsilon}_M} \right| + 53|R - 1| \quad . \tag{105}$$

For $(T_1 \quad T_2) = 10°K$, we have maximum and probable errors of $\pm$ 14.6°K and $\pm$ 7.1°K, respectively.

If we assume that the lunar emissivity is constant and that the precision of measurement is limited only by the noise/signal ratio r of the pyrometer, we have for $R \simeq 1$:

$$\Delta(T_1 - T_2) = 2T_2 D(T_2) r \quad . \tag{106}$$

Equation (106) gives the minimum detectable temperature difference: for our equipment, operating with 4 seconds post-detection integration time and for $T_2 = 400°K$, this value is 0.67°K.

Finally, we may remark that the Eqs. (101), (102), (104), and (105) may be written with $2\Delta(d_{M+S} - d_S)$ and $2\Delta\bar{\varepsilon}_M$ replaced by the equivalent expressions $\Delta(d_{M,1+S} - d_{M,2+S})$ and $\Delta(\bar{\varepsilon}_{M,1}, \bar{\varepsilon}_{M,2})$, respectively. This change makes explicit the dependence of the temperature differences on the differences in signals and emissivities.

c) Error Analysis for Relative Temperature Measurements during the Umbral Phase

Since the differences between lunar surface models are more evident in the cooling curve during the umbral phase of an eclipse, we will apply the previous analysis to bracket the maximum errors and to determine whether we will be able to distinguish between models solely on the basis of the cooling curve in the umbral phase.

For this analysis we will use Eq. (97) but since the lunar area is invariant, the emissivities can be grouped together. Taking $T_1 = 255°K$, $T_2 = 225°K$, which will apply for Tycho during total eclipse conditions, and the errors given in Table I, we see that the errors of measurement are effectively somewhat smaller than the value given for 175°K in Table I. The reasons are that in fact we are averaging together several successive data samples in determining a mean temperature, and that the signal-to-noise ratio is higher at the crater temperature than at 175°K. We find that the maximum error in the measurements of $\frac{T_1}{T_2}$ is ± 0.061 and the probable error ± 0.018, corresponding to maximum and probable errors in $\frac{T}{T_{Max}}$ of ± 0.037 and ± 0.011 respectively. The main contribution to the error in this case comes from the uncertainties in the measurements of d_M and $\bar{\tau}_A(m, T_M)$.

We conclude that a model of the lunar surface must predict the observed decline in the normalized temperature

$\frac{T}{T_{Max}}$ during total eclipse within a very few percent, if we are to accept the model as satisfactory.

d) Instrumental Conclusion

One instrumental conclusion from the previous error analysis is to have the calibration blackbody in front of the telescope entrance stop. This arrangement will eliminate the contribution in the uncertainty of the measurement by the errors in the value of F_{eff}, F_c, and $\bar{\rho}_A$. When this instrumental modification is taken into account the terms $\frac{\Delta F_{eff}}{F_{eff}}$, $\frac{\Delta F_c}{F_c}$ and $\frac{\Delta \bar{\rho}_A}{\bar{\rho}_A}$ will drop out of Eq. (89). In this case the value given in (91) is reduced to $\frac{\Delta T_M}{T_M} = \pm 7\%$. If we apply the above considerations to the relative measurements, the maximum relative error for temperature ratios, for the coefficients of propagation of errors given in Eq. (100) and for $T_2 = 400°K$, will be $\pm 4.6\%$. We can carry out the same analysis for other observing conditions with this instrumental modification to see what reduction in the maximum error can be achieved with this technique.

To fill the entrance stop of a telescope of 60 inches or bigger with a blackbody is not a simple problem, but it is not an insoluble one. We suggest to have a Fresnel blackbody slightly bigger than the telescope aperture. This blackbody should be, for example, hanging from the upper part of the telescope dome so that by pointing the telescope to the

zenith, a calibration signal will be introduced into the telescope. The major problem of such a blackbody is to keep the temperature gradients across the opening to a value of the order of $\pm$ 0.1°K or less. We are working on a design of such a blackbody.

e) Observational Data

The radiation pyrometer and observational technique are fully described by Ingrao and Menzel.[1]

In order to validate the data presented in this report we will describe the observational conditions and parameters of the equipment for the scans shown in Figures 7 and 8.

The scan shown in Figure 7a-b was obtained at the Newtonian focus of the 61-inch telescope at Agassiz Station during the lunar eclipse, December 18-19, 1964. The telescope was stopped down to f/5.58 by an entrance stop in the pyrometer to ensure that the detector did not "see" anything but the mirror objective. The amount of precipitable water, measured from sounding balloons, was 1.4 mm for one air mass, an exceptionally low value for this observing site.

The post-detection time constant of the pyrometer was 0.2 seconds, and the size of the resolution element was 9" x 9" between half-power points. As the scan shows, the temperature anomalies in Copernicus, Milichius, Galilaei, and an unnamed crater, first become evident as a plus ΔT.

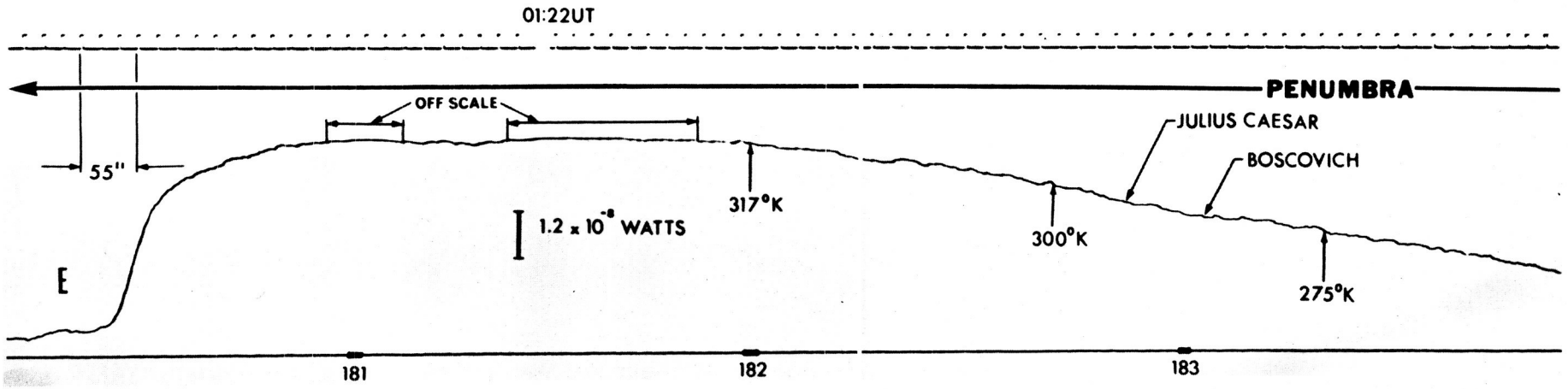

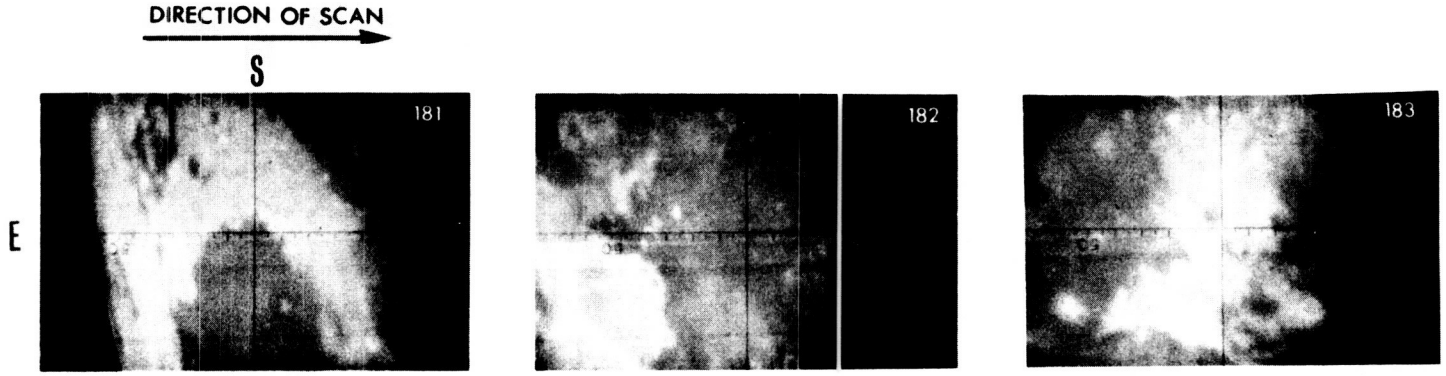

FIG. 7a. First part of a complete lunar scan, time identifying pictures, signal marks, and marks indicating when a picture has been secured. Data obtained during the Lunar Eclipse, December 18-19, 1964, with the 61-inch telescope at Agassiz Station. The total amount of precipitable water in the Earth's atmosphere was 1.4 mm. This part of the scan went through an area in penumbra.

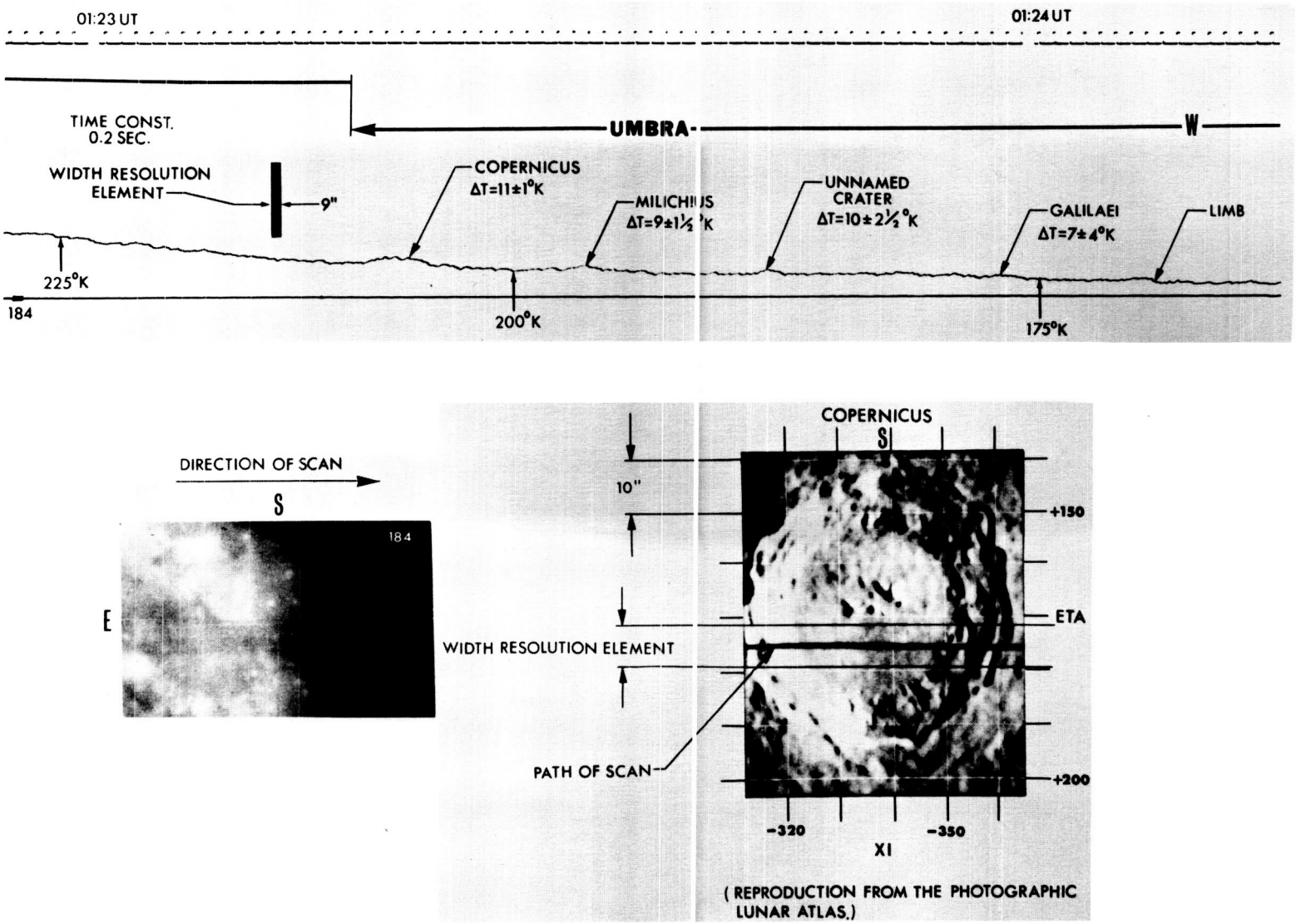

FIG. 7b. Continuation of data and scan shown in 7a. This part of the scan passed almost through the center of Copernicus during the umbral phase. The ΔT's are not corrected by instrumental profile.

The incremental temperatures ΔT shown in the scan are not corrected for the instrumental profile of the pyrometer. This correction will be important for Milichius, the unnamed crater and Galilaei. The power calibration (1.2×10^{-8} watts) of the record was obtained with a blackbody calibration.

Figure 8 shows a scan from Mare Crisium through Manilius, which was obtained a few hours before the lunar eclipse of June 24-25, 1964, at the Newtonian focus of the 74-inch telescope at the Radcliffe Observatory (Pretoria, Rep. of South Africa). The amount of precipitable water for one air mass, measured from sounding balloons, was 2.5 millimeters.

The post-detection time constant of the pyrometer was 0.2 seconds and the size of the resolution element was 8" x 8" between half-power points.

To verify that the structure of the scan shown in Figure 8 has astrophysical meaning, we reverse the sense of scanning at the point indicated by the arrow. The second part of the scan clearly is almost a perfect mirror image of the first part; the small differences are due to the change in declination of the Moon (0.114" per second of time), which over a minute of time amounts to almost 80% of the size of the resolution element. The record shows very clearly the negative increment ΔT for the temperature anomalies in Proclus, Plinius and Manilius.

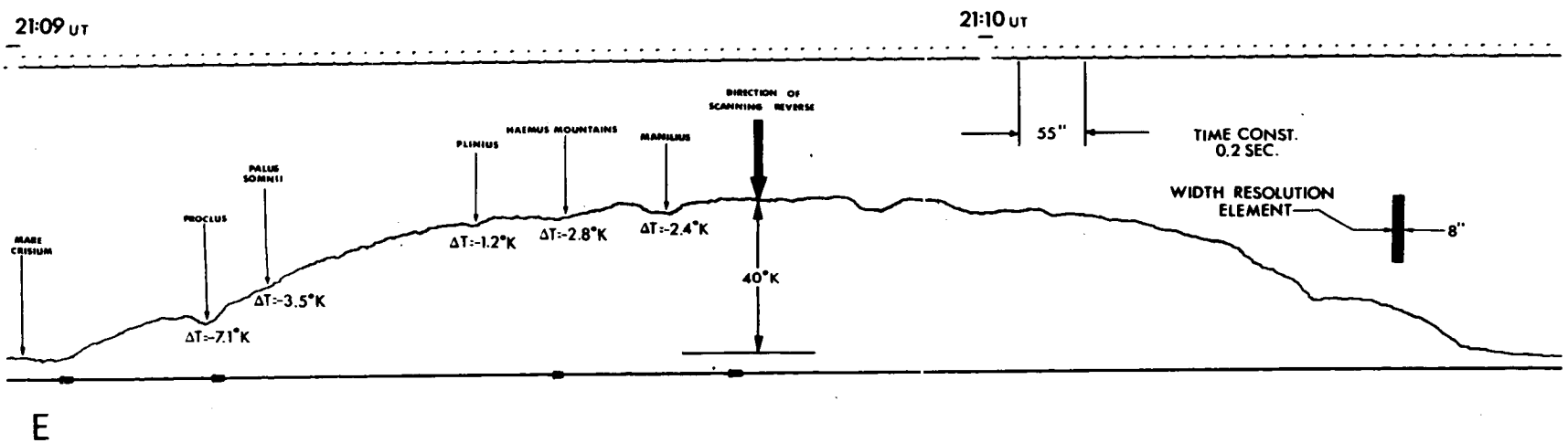

FIG. 8. Scan and time marks a few hours before the Lunar Eclipse of June 24-25, 1964, observed from Pretoria (Rep. of South Africa) with the 74-inch telescope. The scan shows several temperature anomalies. To show the validity of the measurements, the direction of scanning was reversed. The second scan shows an almost perfect mirror image of the first scan. The ΔT's are not corrected by instrumental profile.

Each one of the event marks indicated at the bottom of the scan shown in Figure 8 represents the time at which a picture was secured. The first mark from the left gives the values $\xi = + .879$ and $\eta = + .276$ as the orthographic coordinates of the center of the resolution element on the Moon; at the second mark, $\xi = + .700$, $\eta = + .270$; at the third mark, $\xi = + .285$, $\eta = + .253$; at the fourth mark $\xi = + .065$, $\eta = + .251$.

The root-mean square residual in position for this particular scan is 3.68".

Figure 9 shows the relative radiant emittance of the lunar surface as a function of the zenith distance of the Sun. The observational data were obtained from three scans made a few hours before the lunar eclipse of December 18-19, 1964. The observing conditions for these scans are similar to the conditions for the scan shown in Figure 7; the times indicated in Figure 9 are for mid-scan.

If a smooth lunar surface is assumed, the radiant emittance W of the surface at full Moon will follow the law $W = W_o \cos \alpha$, where W_o is the radiant emittance at the point where the Sun is at the local zenith and α is the zenith distance of the Sun. This curve has been plotted in Figure 9 to show the departure from the assumed cos α dependence.

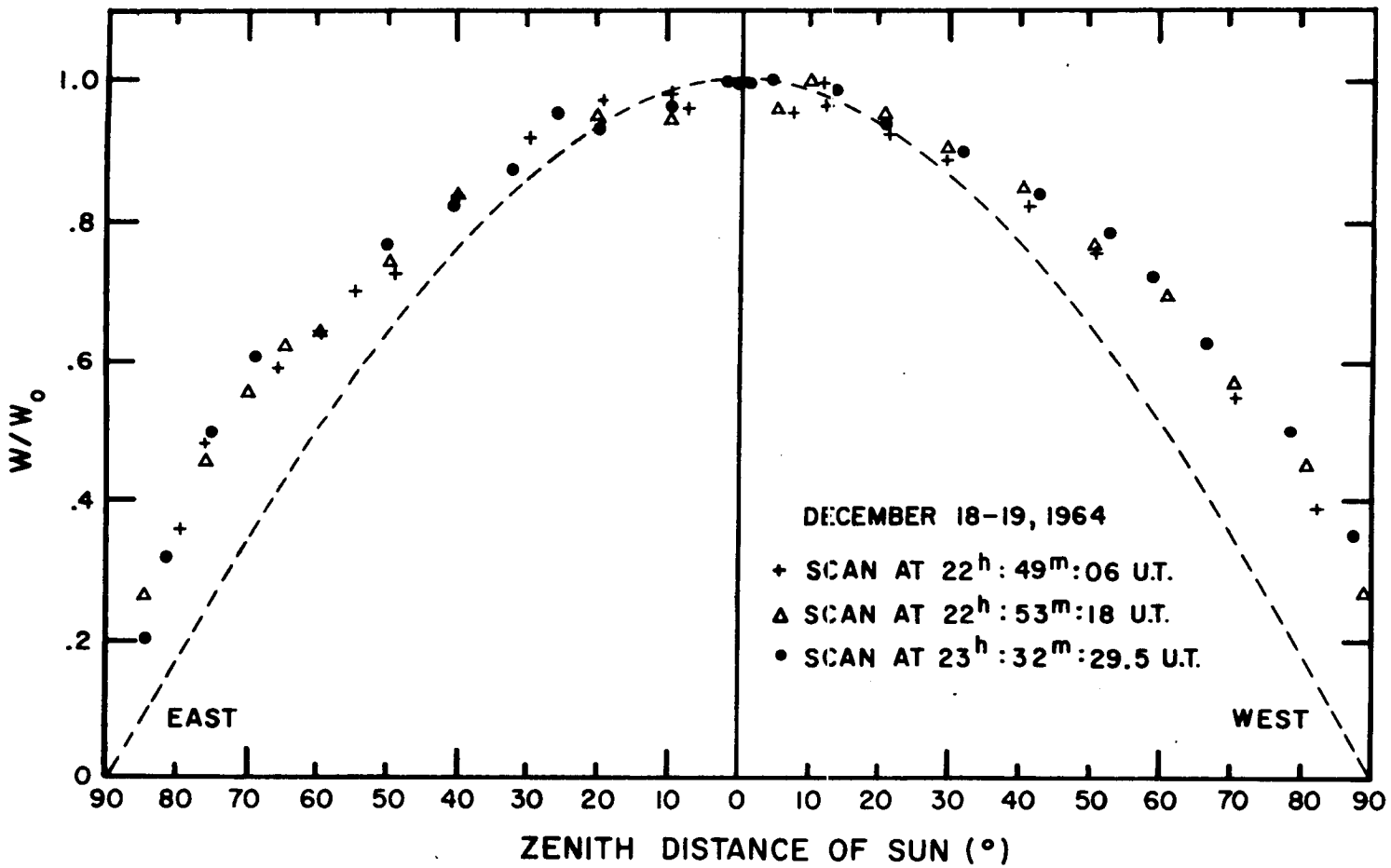

FIG. 9. Relative radiant emittance obtained from scans across the lunar disk. The dashed curve gives the relative radiant emittance as a function of the solar zenith distance for an ideal smooth lunar surface.

The data indicated with crosses in Figure 9 were obtained from a scan that passed at 7° 36' from the sub-solar point, the one indicated with triangles 5° 42' and the one given with dots only 18'. We did not try to fit a curve to these data points since the scans went through areas of completely different physical nature. In a future report, we will analyze our temperature data as a function of the zenith distance of the Sun for specific areas.

VI. Atmospheric Transmittance

Although the opacity of various molecular bands in the infrared has been investigated under idealized and experimental conditions, the cumulative effect of these bands in determining the transmittance of the terrestrial atmosphere in the 8-14 micron "window" has not been adequately treated. The complexity of the many absorption processes and the variability of their importance from day to day preclude a definitive discussion of the problem; however, the incomplete data now available do allow a quantitative investigation of the way in which atmospheric transmittance depends upon water vapor and air mass in the line of sight, and upon the temperature of the extra-terrestrial object observed. From the form of these dependencies we can consider the validity of simple analytical approximations and the limitations they place upon the accuracy of infrared measurements of lunar and planetary temperatures.

Let us first consider qualitatively the manner in which the atmospheric radiant transmittance $\bar{\tau}_A$ is dependent upon the incident radiation field. Radiation is absorbed and re-emitted in each narrow wavelength region of the "window" containing a small part of one or more overlapping bands, each consisting of lines of well-defined shape at each level in the atmosphere. It is usually assumed that the incident radiation field is so weak that re-emission

and scattering into the line of sight may be ignored; and that, in computing the transmittance in this narrow region, one therefore need consider only the pressure and temperature dependence of line profiles and the effects of overlapping lines at each height in the atmosphere, and integrate along the line of sight. For narrow regions of the spectrum Gates and Harrop[5], Sinton and Strong[6,7], and others have shown that the observed radiant transmittance τ_A may be accurately represented in many cases by a dependence of the form $\ln \tau_A(\lambda, m) = k\,m$ or $k\sqrt{m}$ where k is an empirical parameter and m is the air mass. The first case is usually designated a weak line or band, and the second a strong line or band. Such a dependence is analogous to that produced by a line at constant temperature and pressure, and implies that for each such region of the spectrum one can define an effective temperature and pressure.

When one considers a broad region of the spectrum such as that between 8 and 14 microns, the situation becomes more complicated. One can take the idealized example of an incident radiation field independent of wavelength, and can assume that each such narrow region of the spectrum obeys the relationship $\ln \tau_A = k\sqrt{m}$ but has a different parameter even so, the mean transmittance through the whole spectral interval will not obey a $\sqrt{m}$ law. In actual fact, the large portion of this interval at wavelengths longer than 12.9 microns lies within the ν_2 bands of CO_2, in which the overlap

of individual lines produces large deviations from a $\sqrt{m}$ dependence. Thus one would expect that the square root law should not, in general, be obeyed. Furthermore, departures from it should depend upon the temperature of the extra-terrestrial object observed, since for objects hotter than 400°K the short-wavelength region of the spectral interval is more highly weighted by the Planckian distribution, while for temperatures less than 300°K the long-wavelength portion is more important. Finally, the atmospheric radiant transmittance must depend upon the filter used, since it determines the relative contribution of each region of the spectrum.

In general, the radiance from a blackbody of temperature T observed through the terrestrial atmosphere will be given by the expression

$$S(m, T) = \int_0^\infty N_\lambda(T)\tau_o(\lambda)\tau_A(m, \lambda)d\lambda \quad , \tag{107}$$

where $\tau_o(\lambda)$ is the instrumental spectral transmittance, $\tau_A(m, \lambda)$ the atmospheric spectral transmittance, $N_\lambda(T)$ the spectral radiance of the emitting surface, and m the air mass along the line of sight. From measured values of $\tau_o(\lambda)$ one can evaluate this integral directly as Murray and Wildey[8] and Sinton and Strong have done to obtain a table relating S(m) to T. In order to investigate the effects of atmospheric transmittance more directly one can rewrite Eq. (107) as follows:

$$S(m, T) = \bar{\tau}_A(m, T) \int_0^\infty N_\lambda(T) \tau_o(\lambda) d\lambda \quad , \tag{108}$$

$$\text{where } \bar{\tau}_A(m,T) = \frac{\int_0^\infty N_\lambda(T) \tau_o(\lambda) \tau_A(m, \lambda) d\lambda}{\int_0^\infty N_\lambda(T) \tau_o(\lambda) d\lambda} \quad . \tag{109}$$

By writing the transmitted radiance in this manner, one separates the rapidly varying integral in Eq. (108), which needs be evaluated for a large number of temperatures only once, from $\bar{\tau}_A(m, T)$, which depends weakly on T for most temperatures and must be evaluated for different sets of observing conditions. If the object observed is not a blackbody, the atmospheric radiant transmittance will not be affected unless the spectral emissivity of this object deviates appreciably from grayness. In either case the temperature obtained from power measurements will be a brightness temperature, analogous to that obtained at radio wavelengths, which must be corrected to obtain the true surface temperature.

If one were to observe with no filter to isolate portions of the 8 to 14-microns "window," other than one to block radiation at shorter and longer wavelengths, then the radiant transmittance would be given by the equation

$$\bar{\tau}_A(m, T_r) = \frac{\int_{8\mu}^{14\mu} N_\lambda(T)\tau_A(m, \lambda)d\lambda}{\int_0^\infty N_\lambda(T)d\lambda} . \qquad (110)$$

In neither case would the atmospheric radiant transmittance be the unweighted mean transmittance over the spectral interval.

We may proceed further in either of two directions. First, one can obtain high dispersion spectra of the Sun or a small portion of the Moon over a range of air masses each night to obtain values of $\tau_A(m, \lambda)$ necessary for the evaluation of the integral in Eq. (107). This is a difficult procedure, but the more accurate of the two. Alternatively, one can use high quality empirical or computed values of $\tau_A(m, \lambda)$ for a range of m and w, the amount of precipitable water at the zenith, or an analytical expression describing the dependence of $\tau_A(m, \lambda)$ upon m and w. We have chosen the latter approach because it is convenient and it is useful for evaluating both the dependence of $\bar{\tau}_A(m, T_r)$ upon observing conditions and the validity of analytical expressions for this quantity. In making this choice, we lose information about highly variable opacity sources such as aerosol continuous absorption, and the dependence of $\tau_A(m, \lambda)$ on the vertical distribution of water vapor, deviations of pressure and temperature with height in the atmosphere from their mean values, etc.

As a first step in the evaluation of atmospheric radiant transmittance, we must consider what approximate

expressions characterize the zenith angle and water vapor dependence of absorption due to molecular bands in this region of the spectrum. Goody[9,10] has shown that the transmittance through a randomly arranged group of lines of arbitrary shape takes the form

$$\tau_a = \exp\left[-\frac{\Sigma a}{2\pi\delta\left(1 + \frac{\Sigma w}{\pi\alpha}\right)}\right], \qquad (111)$$

where a is the quantity of absorbing material along the line of sight, Σ is the average line intensity per spectral interval, α is the mean Lorentz half-width of the lines, and δ is their mean spacing. Although originally derived for water vapor lines with a = w·m, this model should be applicable to any molecular band or superimposed bands, provided the condition of disorderliness is obeyed. In particular, the work of Gates and Harrop[5] shows this to be a good approximation for most of the spectrum between 8.0 and 12.54 microns, where randomly arranged H_2O lines are superposed upon the more regularly arranged lines of O_3, CO_2, NO_2 and CH_4.

Equation (111) reduces to

$$\ln \tau_a = -c_1\sqrt{a} \qquad (112)$$

in the limit of strong lines or large optical depth, and to

$$\ln \tau_a = -c_2 a \qquad (113)$$

in the limit of weak lines or the wings of stronger lines where the optical depth is small.

When the overlap of neighboring lines in a band becomes sufficiently large that an appreciable fraction of the wing of one line falls in the core of its neighbors, as for example in the ν_2 band of CO_2 beyond 12.9 microns, the transmittance must decrease less rapidly than a square root dependence. Elsasser[11] has shown that for such a band of regularly distributed lines the transmittance can be written in the form

$$\tau_a = \int_{-\frac{1}{2}}^{\frac{1}{2}} \exp\left[-\frac{a \sin(2\pi\alpha/\delta)}{\delta \cosh(2\pi\alpha/\delta) - \cos \nu/\delta}\right] \frac{d\nu}{\delta} \quad , \tag{114}$$

which in the limit of strong lines, $\nu = \frac{\Sigma a}{2\pi\alpha} \gg 1$,

reduces to the form

$$\tau_a \approx 1 - \mathrm{erf}(c_3\sqrt{a}) \quad . \tag{115}$$

In addition to the selective band absorption there is also a continuous component to the infrared opacity. Elsasser[12] originally suggested that the far wings of very strong pure-rotation water-vapor lines at wavelengths centered at 50 microns should contribute to the opacity near 10 microns. Measurements by Saiedy[13,14] and Bignell, Saiedy, and Sheppard[15] corroborate this effect and suggest a dependence of the form (113), with c_2 increasing from

0.00545 per mm of water vapor at 8.66 microns to 0.01144 at 12.0 microns, according to Saiedy, and slightly lower values according to Bignell et al. They also consider the minor effect of aerosol scattering but this will be ignored for the present discussion.

To construct an atmospheric transmittance model with which calculations of the transmittance for a variety of observing conditions may be made, it is important to use a homogeneous set of data obtained at many narrow wavelength intervals throughout the "window," for a wide range of m and w, clearly delineating what analytical form can best describe $\tau_A(m, \lambda)$. To our knowledge no such data exist.

Gates and Harrop[5] have observed the solar spectrum at 80 wavelengths between 8.037 and 12.542 microns over path lengths ranging between 2 and 20 air masses. From these data, the most comprehensive yet obtained, they have subtracted a constant continuous opacity term obtained by extrapolating measurements at 11.032 microns* to zero air mass. They then computed for each wavelength the coefficients c_1, c_2, and c_3 in expressions (112), (113), and the small argument approximation to (115). In almost all cases the strong line random model (112) is the best approximation. Since their data were obtained on one day only, and are expressed in terms of a dependence upon water vapor in the line of sight and not upon air mass, the values of c_1 and c_2 obtained

*At 11.032 microns, atmospheric molecular absorption is nearly absent.

for spectral intervals in which water vapor is not a major constituent must be corrected. To eliminate the water vapor dependence, we have multiplied these coefficients by $\sqrt{3.0}$ mm$^{1/2}$ of H_2O, and 3.0 mm of H_2O, respectively, the mean value of w on their day of measurements, and replaced w by m. Gates and Harrop obtain a value of 0.0175 per mm of H_2O for the continuum absorption coefficient at 11.082 microns, in reasonable agreement with the previously cited measurements, but they consider a continuum coefficient of 0.06195 per air mass, the slope of $-\ln \tau_A(m,\lambda)$ vs. air mass, to be a more accurate fit to their data.

Beyond 13 microns, absorption by CO_2 so dominates the spectrum that other selective opacity sources may be neglected with respect to it. Drayson[16] has recently calculated the transmittances through these CO_2 bands by considering the pressure and temperature dependence of mixed Lorentz-Doppler profiles of the individual lines, and integrating through the atmosphere along a line of sight. For these calculations he has assumed the atmospheric temperature and pressure structure as given by the US Standard Atmosphere,[17] (1962). For the present calculations his zenith transmittance change been used to compute coefficients c_3 in the error function approximation Eq. (115). Although this approximation leads to errors of less than four percent with respect to the exact model expressed by Eq. (114), subsequent versions of the program will incorporate Drayson's direct calculations at a variety of zenith angles.

The evaluations of atmospheric radiant transmittances were carried out by a computer program written in FORTRAN II for the IBM-7094 computer of the Harvard Computation Center. This program is so flexible that it can accept any new atmospheric transmittance data as they become available, and compute the integrals of Eq. (109) for any filter and any region of the infrared spectrum. Evaluating these integrals to a high degree of accuracy involves special problems because of the often discontinuous and rapidly varying nature of the $\tau_A(m, \lambda)$ data. Quite satisfactory results have been obtained by using the subroutine ICE 3 written by N. Moroff of Westinghouse Air Arm, involving an integration procedure which automatically adjusts the increment of the independent variable to keep extrapolation errors within specified limits. Computations of the integrals in Eq. (109) have been performed for the wide-band and narrow-band filters with spectral transmittances shown in Figure 10 and for a rectangular bandpass filter for the spectral range 8-14 microns. The wide-band filter, which includes the whole spectral interval 8-14 microns, was used for eclipse observations on the night of December 18-19, 1964, at Agassiz Station. The narrow-band filter eliminates the CO_2 bands and much of the O_3. We have used the parameters of Gates and Harrop which best fit their measurements, and the data of Drayson as previously described. Since a gap remains between 12.54 microns and the CO_2 bands in which no homogeneous

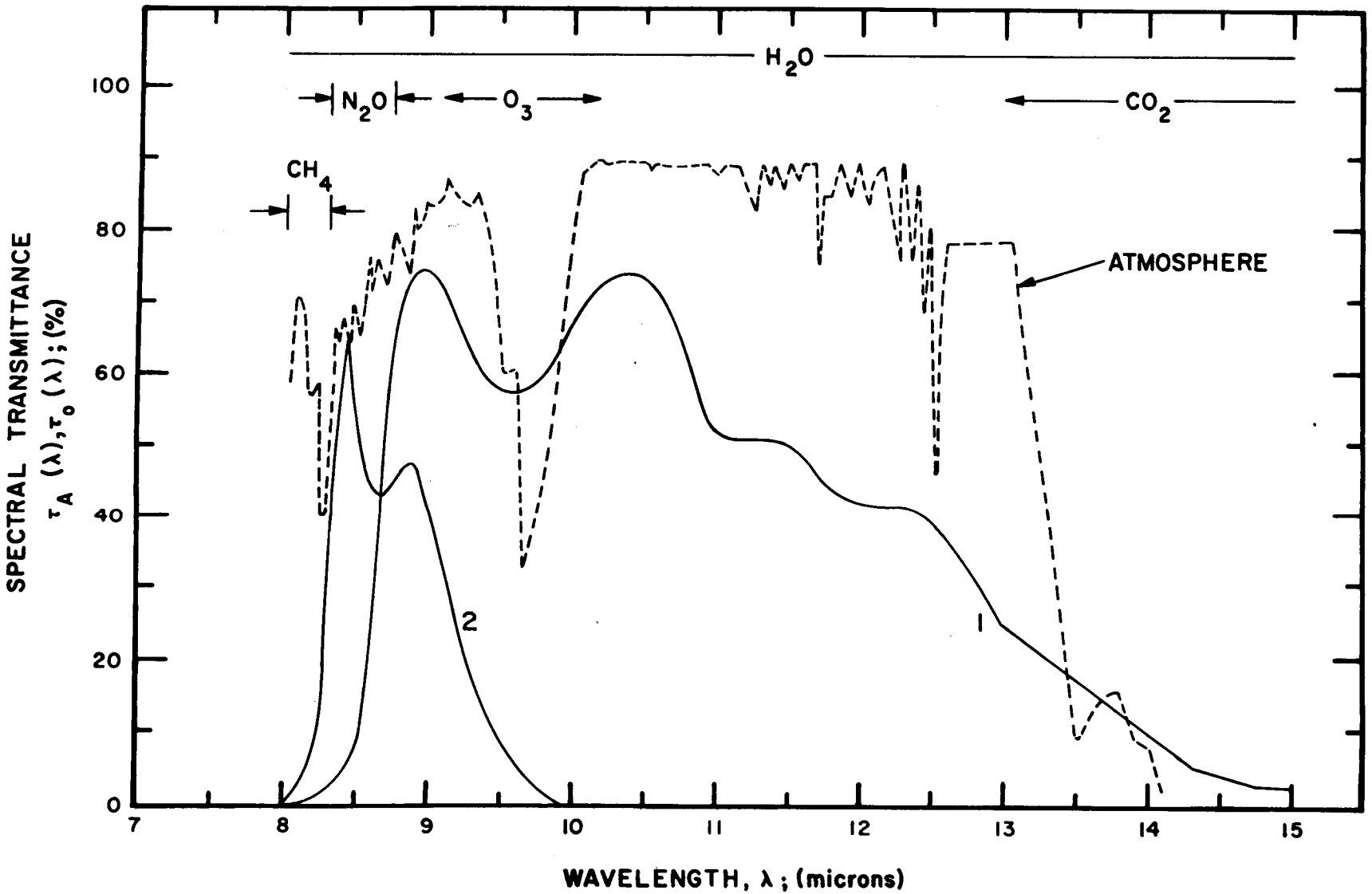

FIG. 10. Spectral transmittances $\tau_o(\lambda)$ of 1) wide-bandpass filter detector window combination, and 2) narrow-bandpass filter detector window combination. Predicted spectral atmospheric transmittance $\tau_A(\lambda)$ based upon our model for 10 mm of precipitable water and m = 1. Regions of the spectrum with the important absorbing constituents are marked. (The region between 12.54 and 13.0 microns has been interpolated.)

quantitative data exists, we have extrapolated the mean $\tau_A(m, \lambda)$ between 12 and 12.54 microns to the wavelength at which the CO_2 absorption becomes comparable. The Jungfrau high dispersion spectra in this region taken by Migeotte, Neven, and Swensson[18] suggest that this is not an unreasonable procedure. Both continuous opacity models have been tried, but no attempt has been made to incorporate surface pressure and temperature dependencies for the present. We will discuss the limitations imposed by these latter assumptions presently.

Typical results of the form of $\bar{\tau}_A(m, T)$ are shown in Figure 11 for the case of the wide-band filter and a continuous absorption coefficient 0.01075 per mm of H_2O. For these and all the other observing conditions considered, only a very small change occurs in the radiant transmittance between 400°K and 200°K; but for incident radiation colder than this, the Wien tail of the Planckian distribution strongly weights the long-wavelength portion of the window, where the opacity is greatest, thereby decreasing $\bar{\tau}_A(m, T)$. With no filter, the effect is more pronounced.

As a first attempt to find a general two-or three-parameter expression relating $\bar{\tau}_A(m, T)$ to m, T, and w, we might try the form

$$\bar{\tau}_A(m, T) = \exp\left[-k(w, T)m^{n(w,T)}\right] \quad , \tag{116}$$

where n(w, T) is the effective power law for the given filter,

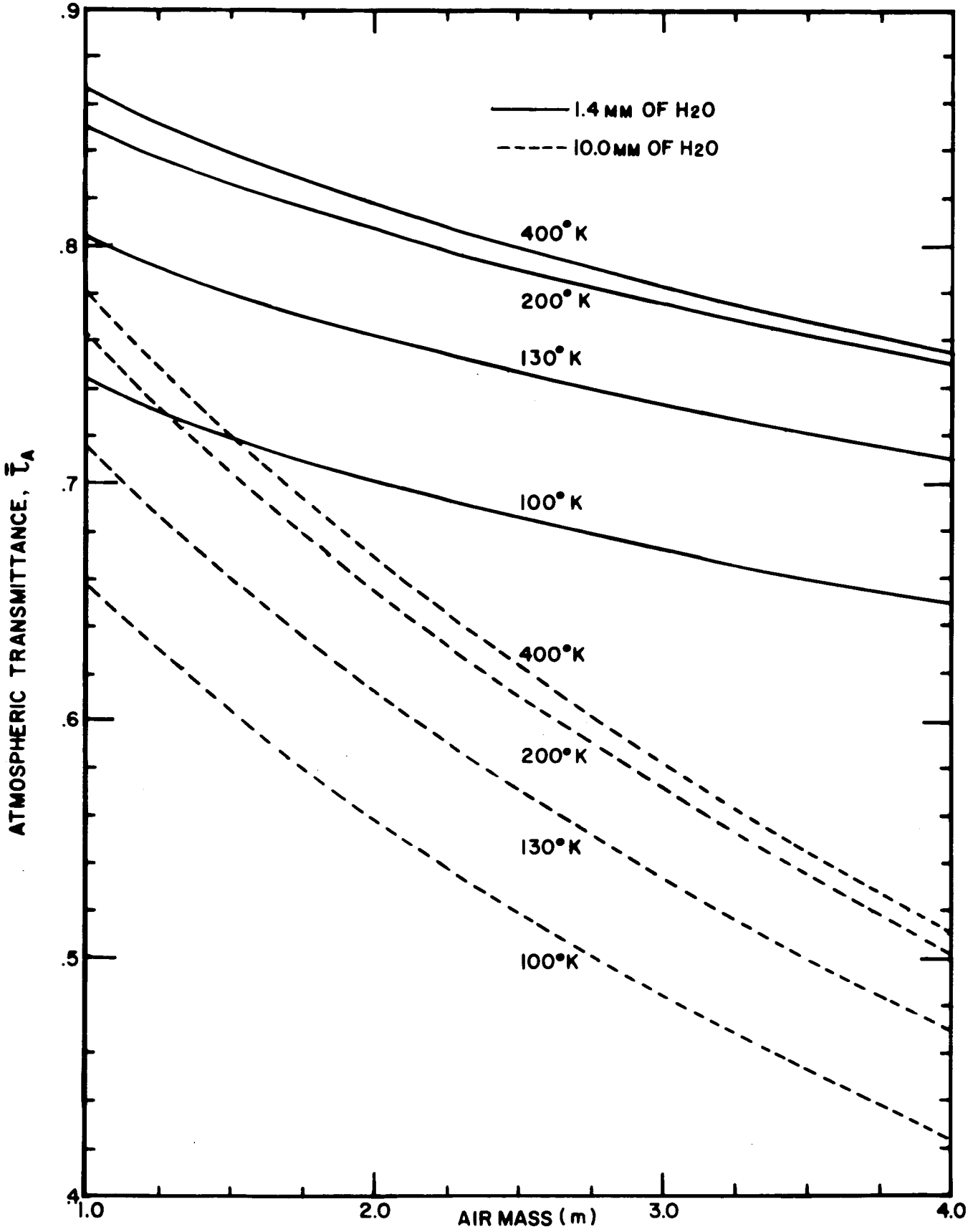

FIG. 11. Atmospheric transmittance versus air mass; the parameters are the temperature of the surface observed and the amount of precipitable water at one air mass. These transmittances are applicable only to the wide-bandpass filter shown in Figure 10.

amount of water vapor at the zenith, and temperature radiation. We may solve for n(w, T) directly by taking logarithms, and obtain

$$n(w, T) = \frac{\log_{10}\left\{-\log_{10}[\bar{\tau}_A(m, T)]\right\}}{\log_{10}(m)} \quad . \tag{117}$$

Three of the cases shown in Figure 12 show that indeed the slope n(w, T) is often nearly independent of the air mass and is thus a good parameter to characterize the problem. The computer program fits a parabola to such points by the method of least squares for each computed model, obtaining the parameters A and B and k(w, T) for

$$n(w, T) = A \log_{10} m + B \quad . \tag{118}$$

Thus, k(w, T) is the absorption coefficient, B the slope at the zenith, and A is a measure of the variations of the slope with air mass.

We have assembled computed parameters under a wide variety of conditions with the wide-bandpass filter, in Table II; with the rectangular-bandpass filter for the spectral interval 8 microns to 14 microns, in Table III; and for the narrow-bandpass filter in Table IV. As a check on the errors involved in the procedure of assuming n to be 0.5 and extrapolating observations to zero air mass to obtain the extra-terrestrial irradiance, the computed values of $\bar{\tau}_A(m, T)$ between 1 and 2 air masses have been extrapolated in this manner. The values obtained on the assumption of unit irradiance are also presented in these tables.

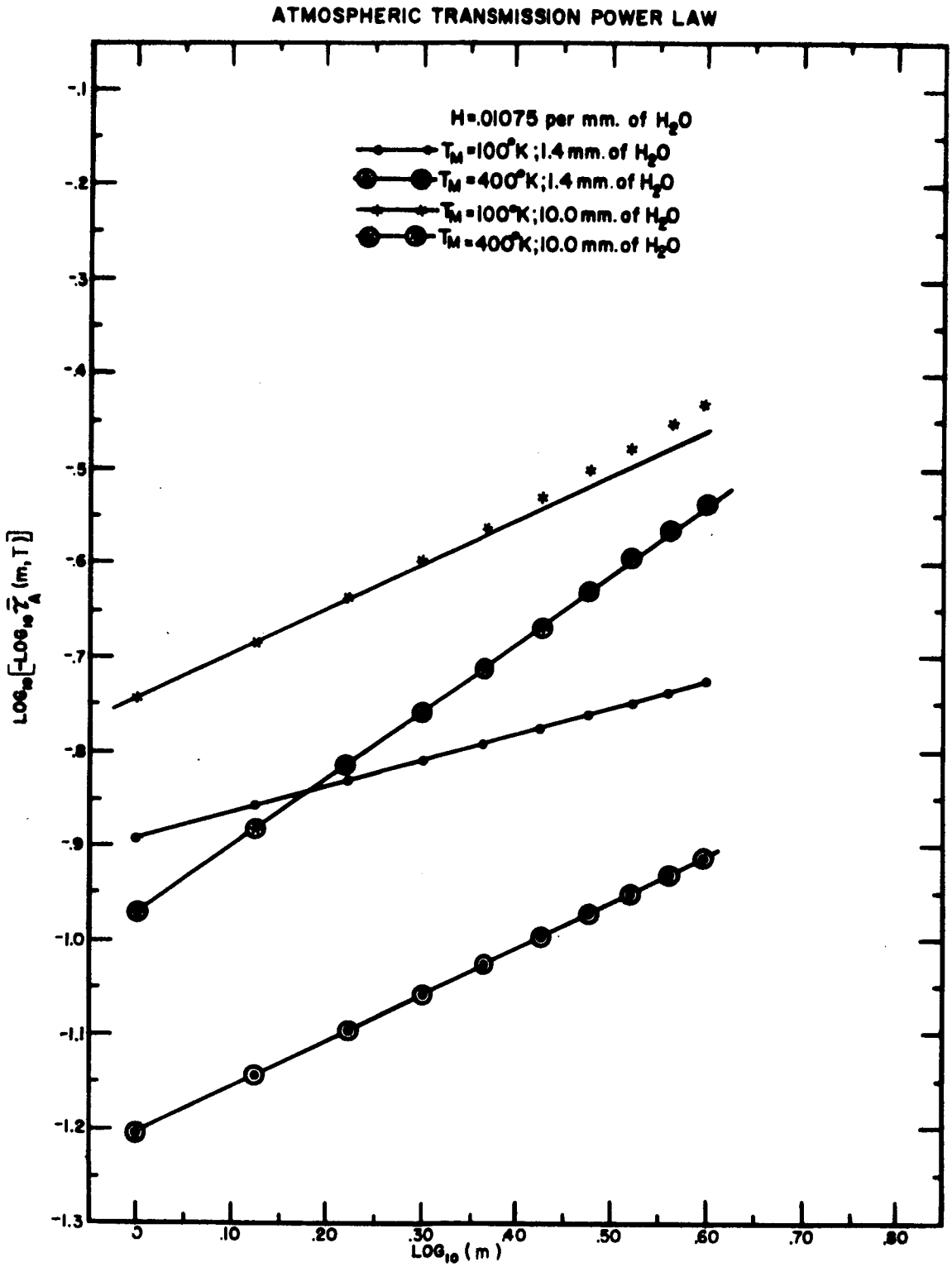

FIG. 12. The power n(w,T) in the equation characterizing the atmospheric transmittance

$$\bar{\tau}_A(T,m) = \exp\left[-K(w,T)m^{n(w,T)}\right]$$

is given by the slopes of these plots for two amounts of precipitable water at one air mass and two lunar surface temperatures. An approximation of n(w,T) independent of air mass is valid except for the upper plot where significant deviations at large air masses are apparent.

TABLE II

ATMOSPHERIC TRANSMITTANCE PARAMETERS WITH WIDE-BANDPASS FILTER

w(mm of H_2O)	Continuous Absorption Coefficient	Temperature (°K)	$\bar{\tau}_A(T,m=1)$	$\Delta\bar{\tau}_A/\Delta w$	A	B	k	Q**
1.4	0.01075 per mm of H_2O	100	.7478	-.0119	+.00306	.273	.291	.850
		130	.8056	.0120	.0204	.316	.216	.929
		160	.8328	.0119	.0259	.357	.183	.943
		200	.8489	.0116	.0147	.402	.164	.967
		400	.8622	.0109	.00560	.467	.148	.988
5.0	0.01075 per mm of H_2O	100	.7085	.0099	.0830	.364	.345	.918
		130	.7655	.0102	.0957	.423	.267	.969
		160	.7929	.0102	.0883	.475	.232	.999
		200	.8096	.0101	.0808	.515	.211	1.018
		400	.8248	.0103	.0657	.575	.193	1.042
10.0	0.01075 per mm of H_2O	100	.6621	.0086	.1214	.450	.413	.984
		130	.7173	.0090	.1181	.521	.332	1.038
		160	.7439	.0091	.1156	.567	.296	1.067
		200	.7612	.0091	.0993	.610	.273	1.093
		400	.7778	.0089	.0800	.665	.251	1.137
1.4	0.060* per air mass	100	.7149	.0038	.0978	.367	.335	.924
		130	.7702	.0033	.1121	.430	.261	.977
		160	.7962	.0029	.1088	.481	.228	1.000
		200	.8116	.0025	.0926	.528	.209	1.030
		400	.8243	.0016	.0711	.589	.193	1.051
5.0	0.060* per air mass	100	.7041	.0023	.0911	.375	.351	.926
		130	.7607	.0020	.1024	.436	.274	.977
		160	.7879	.0017	.0940	.489	.238	1.007
		200	.8046	.0015	.0858	.529	.218	1.027
		400	.8197	.0009	.0697	.588	.199	1.051

*Gates & Harrop Suggest .06195

**Q is the ratio (for m=0) between the irradiance computed by use of a square-root law and the irradiance computed from Equations (116)and (118).

TABLE III

ATMOSPHERIC TRANSMITTANCE PARAMETERS WITH RECTANGULAR BANDPASS FILTER FOR SPECTRAL RANGE 8 - 14 MICRONS

w(mm of H_2O)	Continuous Absorption Coefficient	Temperature (K°)	$\bar{\tau}_A(T,m=1)$	$\Delta\bar{\tau}_A/\Delta w$	A	B	k	Q**
1.4	0.01075 per mm H_2O	100	.6581	-.0106	-.0996	.349	.419	.856
		130	.7190	.0111	.0725	.354	.330	.888
		160	.7537	.0113	.0547	.366	.283	.917
		200	.7784	.0114	.0407	.385	.251	.935
		400	.8027	.0111	.0209	.430	.220	.964
5.0	0.01075 per mm of H_2O	100	.6234	.0088	.0246	.406	.473	.905
		130	.6822	.0093	+.0055	.424	.382	.942
		160	.7161	.0095	.0227	.444	.334	.966
		200	.7405	.0097	.0359	.466	.301	.986
		400	.7655	.0096	.0491	.510	.267	1.015
10.0	0.01075 per mm of H_2O	100	.5822	.0076	.0308	.463	.541	.972
		130	.6382	.0082	.0547	.491	.499	.991
		160	.6708	.0094	.0676	.517	.399	1.030
		200	.6947	.0086	.0744	.543	.364	1.054
		400	.7199	.0086	.0778	.589	.329	1.088
1.4	0.060* per air mass	100	.6291	.0034	-.0103	.404	.464	.908
		130	.6874	.0033	+.0215	.424	.375	.946
		160	.7206	.0032	.0385	.447	.328	.971
		200	.7442	.0030	.0485	.473	.296	.992
		400	.7674	.0024	.0544	.522	.265	1.022
5.0	0.060* per air mass	100	.6195	.0021	-.0157	.413	.479	.912
		130	.6775	.0016	+.0142	.432	.389	.947
		160	.7117	.0019	.0309	.454	.340	.974
		200	.7359	.0018	.0433	.480	.307	.994
		400	.7607	.0014	.0551	.521	.274	1.023

*Gates & Harrop Suggest .06195

**Q is the ratio (for m=0) between the irradiance computed by use of a square-root law and the irradiance computed from Equations (116) and (118).

TABLE IV

ATMOSPHERIC TRANSMITTANCE PARAMETERS WITH NARROW-BANDPASS FILTER

w(mm of H_2O)	Continuous Absorption Coefficient	Temperature (°K)	$\bar{\tau}_A(T,m=1)$	$\Delta\bar{\tau}_A/\Delta w$	A	B	k	Q**
1.4	0.01075 per mm of H_2O	100	.8329	-.0084	+.0193	.540	.183	1.019
		130	.8298	.0083	-.0001	.547	.187	1.023
		160	.8271	.0089	.0017	.548	.190	1.021
		200	.8239	.0097	+.0208	.533	.194	1.016
		400	.8180	.0098	.0044	.541	201	1.020
5.0	0.01075 per mm of H_2O	100	.8009	.0088	.0330	.635	.222	1.077
		130	.7977	.0087	.0370	.626	.226	1.075
		160	.7937	.0089	.0383	.620	.231	1.074
		200	.7913	.0088	.0226	.628	.234	1.078
		400	.7842	.0091	.0428	.610	.243	1.072
10.0	0.01075 per mm of H_2O	100	.7583	.0082	.0464	.707	.277	1.156
		130	.7550	.0082	.0529	.699	.281	1.154
		160	.7509	.0083	.0557	.689	.287	1.152
		200	.7485	.0082	.0478	.694	.290	1.157
		400	.7413	.0081	.0602	.677	.299	1.149
1.4	0.060* per air mass	100	.7963	.0005	.0579	.630	.228	1.082
		130	.7933	.0005	.0438	.633	.233	1.086
		160	.7908	.0001	.0425	.633	.235	1.084
		200	.7877	.0008	.0594	.620	.239	1.079
		400	.7820	.0010	.0466	.623	.246	1.082
5.0	0.060* per air mass	100	.7959	.0002	.0365	.645	.228	1.086
		130	.7927	.0001	.0405	.636	.232	1.084
		160	.7887	.0003	.0418	.630	.237	1.082
		200	.7864	.0004	.0266	.637	.240	1.087
		400	.7793	.0005	.0462	.620	.249	1.081

*Gates & Harrop Suggest .06195.

**Q is the ratio (for m=0) between the irradiance computed by use of a square-root law and the irradiance computed from Equations (116) and (118).

Several observations may be drawn immediately from these calculations. First, the rapid decrease in the atmospheric radiant transmittance at low temperatures cannot be avoided unless one completely filters out radiation in the CO_2 bands. Second, under certain circumstances a square-root power law is a very good approximation: for example, when observing the Sun or the lunar subsolar point with a wide-band filter under very dry conditions, assuming the water-dependent continuous absorption model, or when observing any object through a filter excluding the CO_2 and O_3 bands, under the same conditions. In this connection, we note that Strong's[19] observations of the Sun corroborate the square root law. However, under many circumstances such an approximation leads to significant errors in the extrapolated extra-terrestrial radiance even at high temperatures. Since the 8-14 micron "window" lies almost entirely in the Rayleigh-Jeans domain of the Planck distribution at 400°K, but in the Wien approximation at 100°K, the sensitivity of the inferred temperature to errors in radiance depends in an important manner upon the temperature itself. In Figure 13 we show the increment in lunar brightness temperature per 1% change in observed irradiance versus lunar brightness temperatures. The three curves are for three different filters. Thus, to measure the subsolar point temperature to within ± 1°K, the atmospheric transmittance needs to be determined to better than 1%; during an eclipse, for temperatures close to 160°K, 5% accuracy is sufficient for ± 1°K temperature measurements.

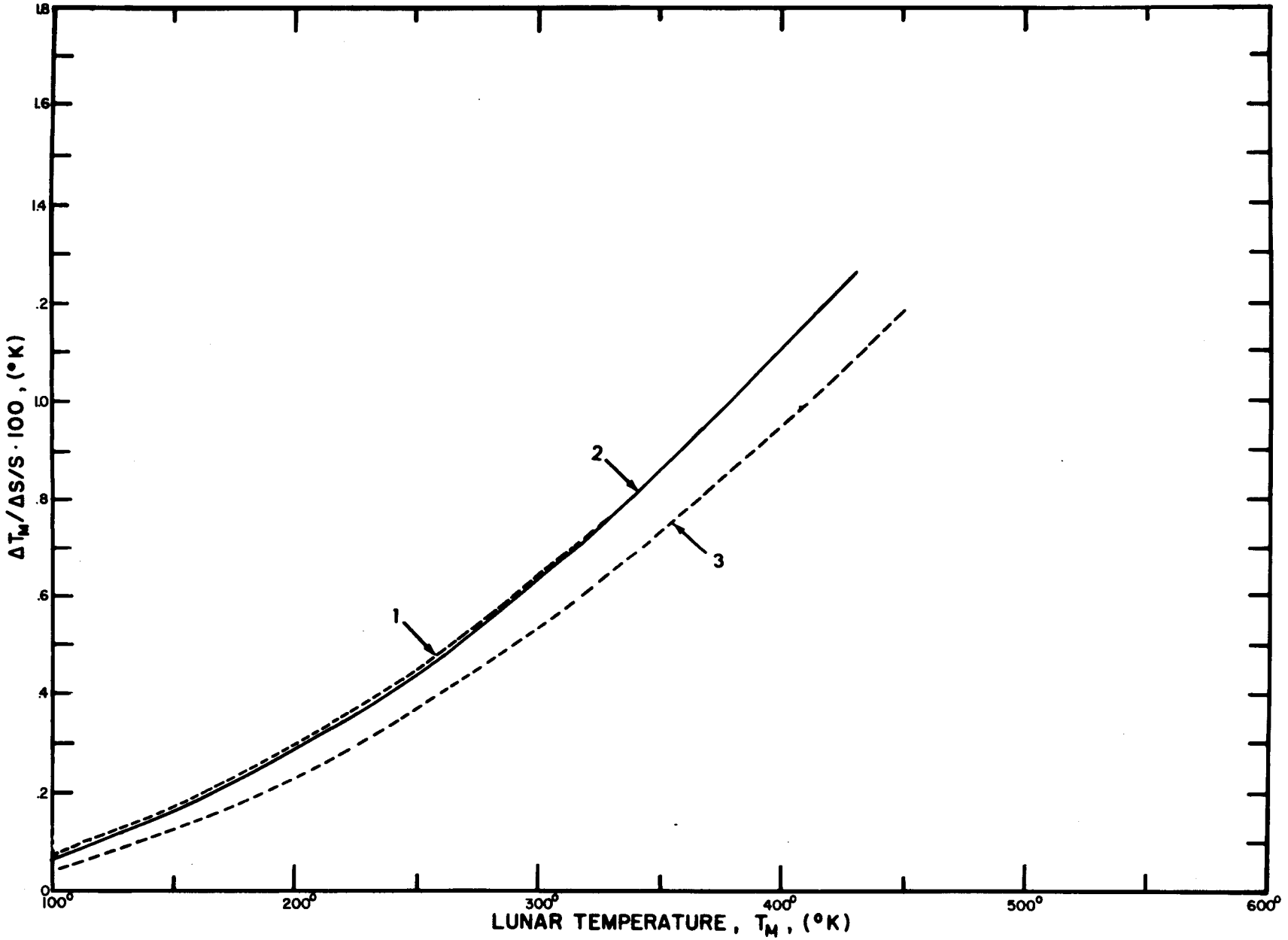

FIG. 13. Increment in lunar brightness temperature per 1% change in observed irradiance versus brightness temperature of the lunar surface. Curve 1 applies for a 8-14 microns rectangular-bandpass filter, curve 2 for the wide-bandpass filter, and curve 3 for a narrow-bandpass filter, the last two with spectral transmittances shown in Figure 10.

We note further that for models in which the continuous absorption component is small, the curvature parameter A is small, and an approximation of n independent of air mass is good. When the continuous absorption component is not small, it acts throughout the spectrum as an opacity source with a power of one and becomes more important relative to the band absorption as the air mass increases, increasing the value of n.

To judge the applicability of these calculations to other filters, one should note that the wide-band filter modifies the atmospheric radiant transmittance in two ways. First, it reduces the importance of the CO_2 absorption bands between 13 and 14 microns. Since these act as opacity sources with a power law less than one-half, the resultant n will in general be larger and less dependent upon the air mass than if no filter is used. Secondly, the filter transmits some radiation between 14 and 15.2 microns. Thus, the values of n at the lowest temperatures are less than if the rectangular bandpass filter (8-14 microns) is present.

As a final consideration, we can use this computer program to predict how errors in the measurement of w will affect $\bar{\tau}_A(T, m)$. These changes in transmittance $\Delta\bar{\tau}_A/\Delta w$ given in Tables II, III, and IV were computed by comparing the transmittances for the previously computed cases with those for atmospheres with 1 mm more water vapor at the zenith. The changes vary from a high of 1.6% for dry

atmospheres with continuous opacity due to water vapor to essentially zero in some cases. Again these errors affect temperature determinations mainly when one observes surfaces at high temperatures.

Since the present program is based on inadequate data, it has limited applicability for the routine determinations of accurate transmittances. To adequately distinguish dependencies upon w from those on air mass, one must have empirical high-resolution atmospheric-absorption parameters similar to those of Gates and Harrop, but for the whole window or at least up to 13 microns, and obtained over many days of observing. Drayson's CO_2 band data appear to be useful since they involve determinations of transmittances at a variety of zenith angles and pressures. However, they were computed assuming the US Standard Atmosphere temperature and pressure distribution, which has a sea level temperature of 15°C. The computations of Sasamori[20], for the transmittance of a homogeneous slab of CO_2 in which the Lorentz half-width is assumed independent of T, imply a variation of the transmittance of 0.8 percent per °K between 13 and 14 microns. Surely this will be a realistic upper limit to variations, since temperature changes will be mainly near the surface. Drayson's data imply a variation of $\pm$ 1 to 2% in the CO_2 band transmittance over typical variations in surface pressure, for example, between 1013.25 mbars and 1000 mbars. Finally, Saiedy has obtained an approximate

variation of 1% in the water-vapor dependent continuum absorption coefficient per °K surface temperature change.

Until such problems are solved and surface temperature and atmospheric pressure effects have been adequately investigated and considered, the procedure described here should be taken as a first attempt to investigate the validity of various approximations in describing the atmospheric absorption.

VII. Lunar Surface Models Based on Infrared Measurements

Careful consideration of cooling curves of the craters Tycho and Copernicus, which we obtained during the lunar eclipse of December 18-19, 1964, and of infrared lunation data obtained by Murray and Wildey,[8] strongly suggests that the idealized one- and two-layer models of the lunar surface are not adequate for the unique interpretation of infrared eclipse and lunation measurements. These data suggest that the one- and two-layer models which assume temperature-independent thermal properties have not been properly applied to correspond with the actual conditions on the lunar surface, and that the effects of temperature-dependent properties should be more thoroughly investigated.

The sensitive infrared detectors used by Murray and Wildey to measure lunar nighttime temperatures provide a new tool for investigating the thermal properties of the lunar material a few millimeters beneath the surface. Because of these observations, and because the predicted structure of the lunar surface depends on the assumptions embodied in the models, we believe it important to rediscuss the thermal conduction problem and to emphasize the physics of energy transport as postulated in the several models. By varying each assumed property of a given model, one at a time, we can discover how a particular factor affects both the eclipse and the lunation cooling curves obtained and can ascertain which are the simplest models, and what are the range of values of their parameters that are consistent with the observed data.

The thermal properties of various types of lunar-surface models that we will discuss may be characterized in terms of four criteria:

(1) depth dependence,

(2) temperature dependence,

(3) horizontal surface variations,

(4) extent of the lunar surface over which averages are made.

Since infrared measurements usually resolve a region on the lunar surface over which the local solar zenith angle at a given time is nearly constant, several investigators (e.g., Wesselink,[21] Jaeger,[22] Jaeger and Harper[23]) have calculated surface temperatures which, strictly speaking, pertain only to one point, usually the subsolar point. Levin[24] has noted that measurements of thermal radio emission obtained with very low spatial resolution on the lunar disk can be misinterpreted when compared with predictions of models which apply only to a point. In particular, he suggests that when the emission from a large region of the lunar surface, which has a significant variation in solar zenith angle and thermal history, is averaged by an antenna with a large beam-width, the characteristic properties of multilayer models will be lost. Piddington and Minnett,[25] using an antenna which at 1.25 cm has a half-width to half-power points of 23', obtained a condition, based upon their phase lag measurements, which relates the temperature-independent thermal properties of the

upper and lower layers of two-layer models to the depth of the upper layer. Until this or some other condition is verified by radio observations of high spatial resolution, we cannot use it as a basis for discussion.

As a first step we shall generalize the horizontally homogeneous models with temperature-independent properties, that is, those in which the thermal properties are a function of depth only. Then we will consider in the light of our data the possible importance of horizontal inhomogeneities such as a fraction of the surface consisting of "exposed rock." In Section c we will discuss what happens to the surface temperature when we also consider radiative transport of energy inside the surface and a linear temperature dependence of the thermal properties.

a) Basic Equations and Computing Methods

Under the assumption of a plane-parallel lunar surface in which the thermal properties are only a function of depth x, measured positively inwards, the flux conducted outward in a solid material would be

$$F_c = K_o\left(\frac{\partial T}{\partial x}\right) , \qquad (119)$$

where K_o is the bulk thermal conductivity of the material. Between two planes each with radiant emissivity $\bar{\varepsilon}_M$, separated by a distance s', the radiated flux is given by the equation

$$F_R = 4\varepsilon'\sigma\bar{T}^3 s'\left(\frac{\partial T}{\partial x}\right) , \qquad (120)$$

where the effective emissivity ε', corrected for multiple reflection, is

$$\varepsilon' = \bar{\varepsilon}_M^2 [1 + (1 - \bar{\varepsilon}_M)^2 + (1 - \bar{\varepsilon}_M)^4 + \ldots] \quad .* \qquad (121)$$

In Eq. (120) σ is the Stefan-Boltzmann constant and $\bar{T}$ the mean temperature between the two planes. The very uppermost material on the lunar surface may be porous or composed of finely-divided material. In this case the total heat flux in this material would consist in part of thermal conduction, where the material is solid, and in part of radiative transfer across the empty spaces. If we consider a porous structure which contains holes of characteristic size a, and if we further assume that the ratio R of radiated flux to conducted flux is not so large that significant departures of the temperature occur at any point from the mean temperature at that depth, the total upward flux will be given by the equation

$$F = [(1 - p)K_o + 4\varepsilon'\sigma T^3 pa]\frac{\partial T}{\partial x} \quad , \qquad (122)$$

where p is the fraction of the structure occupied by the spaces. Since we have no prior knowledge of p and there is no direct way of measuring this quantity from earth-based observations, it is useful to rewrite this expression in terms of the effective conductivity K and effective spacing s, where

---

*A further discussion of radiative conductivity relevant to this problem may be found in Wesselink[21] and Whipple.[26]

$$F = (K + 4\bar{\varepsilon}_M \sigma \bar{T}^3 s)\frac{\partial T}{\partial x} \quad , \tag{123}$$

$$s = pa\frac{\varepsilon'}{\bar{\varepsilon}_M} \quad , \tag{124}$$

$$K = (1 - p)K_o . \tag{125}$$

One could, of course, consider any of a number of small-scale geometrical configurations, for example, spheres in contact, but in all such cases the flux could be written in the form given above, except that K and s would have different meanings. The following arguments in no way depend upon this assumed porous structure, since only the thermal properties can be ascertained by infrared measurement, and a fuller discussion of such structures would be pointless.

Before proceeding, let us consider whether radiative transfer could indeed play an important role. For a typical value of K, such as 5×10^{-6} cal $cm^{-1}{}^{\circ}K^{-1}$ considered below, and a temperature of 350°K, the conductive flux and radiative flux become equal for a separation $s \approx 200$ microns. This distance scale is not inconsistent with that measured by Wechsler and Glaser[27] for powdered rocks deposited under high vacuum, and may be appropriate for large regions of the lunar surface.

The heat conduction equation now assumes the form

$$\rho c\frac{\partial T}{\partial t} = \frac{\partial}{\partial x}\left[(K + 4\bar{\varepsilon}_M \sigma T^3 s)\frac{\partial T}{\partial x}\right] \quad , \tag{126}$$

with ρ the density, c the specific heat, and t the time. At a point with orthographic coordinates (ξ, η) and bolometric albedo A_b, the flux into the surface is given by the difference between the absorbed insolation $(1 - A_b)\, I(\xi, \eta, t)$ and the energy radiated into space. Neglecting physical libration and the inclination of the Moon's equator to the ecliptic, we find that the surface boundary condition becomes

$$(K + 4\bar{\varepsilon}_M \sigma T_o^3 s)\left(\frac{\partial T}{\partial x}\right)_{x=o} = \bar{\varepsilon}_M \sigma T_o^4 - (1 - A_b) I(\xi, \eta, t) \quad , \qquad (127)$$

where during the lunar day

$$I(\xi, \eta, t) = f(t)\sigma T_s^4 \left[-\xi \sin\left(\frac{2\pi t}{P}\right) + \sqrt{1 - \eta^2 - \xi^2}\cos\left(\frac{2\pi t}{P}\right)\right] \; ; \qquad (128)$$

P is the synodic period of revolution, $\bar{\varepsilon}_M$ the radiant emissivity in the observed wavelength region, T_o the surface temperature, and T_S the theoretical subsolar point temperature. With the value of 1.99 ± 0.02 cal cm^{-2} min^{-1} for the solar constant as given by Allen,[28] T_S is $395 \pm 1°K$. Wesselink has noted that the subsolar surface temperature for reasonable values of surface conductivity never reaches this theoretical limit, since a small fraction of the incident flux is conducted inwards. For example, for a homogeneous model with temperature-independent thermal properties and surface thermal parameter of $\gamma \equiv (K\rho c)^{-1/2} = 1000$ in cal cgs units, which closely fits our data for the environs of Tycho, the calculated subsolar temperature is 393.2°K for $\bar{\varepsilon}_M = 0.93$ and varies only by $\pm$ 0.1°K for $\pm$ 0.05 changes in $\bar{\varepsilon}_M$.

We shall assume that the radiant emissivity at visual wavelengths ($1 - A_V$), commonly given as 0.932 (Astrophysical Quantities), is equal to the radiant emissivity in the infrared. We have assumed a value of 0.93 for the subsequent calculations, and will discuss below how a change in this quantity affects the theoretical cooling curves during an eclipse and a lunation.

During the penumbral eclipse, the insolation is reduced by a factor f(t) determined by the portion of the solar disk occulted by the Earth and by solar limb darkening. For this latter quantity the values at 6000 Å given in Astrophysical Quantities have been used.

In the light of Jaeger and Harper's success with two-layer models, we consider a multilayered model, which will better approximate to a more realistic situation in which thermal parameters continuously vary with depth, if the data should warrant adding this complication. At the boundary of two layers, L and L + 1, the temperature is continuous,

$$T_L = T_{L+1} \tag{129}$$

and the heat conduction equation may be written as

$$\left(\frac{\rho_L c_L + \rho_{L+1} c_{L+1}}{2}\right)\left(\frac{\partial T_L}{\partial t}\right) = \lim_{\Delta x \to o}\left[\frac{(K_{L+1} + 4\bar{\varepsilon}_M \sigma T_L^{\,3} s_{L+1})(\partial T/\partial x)_{L+1}}{(\Delta x)_L} - \frac{(K_L + 4\bar{\varepsilon}_M \sigma T_L^{\,3} s_L)(\partial T/\partial x)_L}{(\Delta x)_L}\right] \tag{130}$$

At the present time we are interested in a method of solving Eqs. (126) and (130), both for an eclipse and for a lunation, which will readily allow computation with an arbitrary form of temperature dependencies of the thermal properties. Fourier techniques, despite their elegance, are clearly unsuited for such nonperiodic phenomena as an eclipse. Solutions utilizing Laplace transform techniques have been attempted, but for mathematical simplicity one must often oversimplify or even ignore the relevant temperature dependencies of each parameter. For these reasons and for its ready adaptability to machine computation, we have adopted the difference-equation approach throughout.

Using first and second forward and central differences, and writing the temperature at a time $n(\Delta t)$ and depth $m(\Delta x)$ as T_m^n, we write Eqs. (126), (127), and (128) in the forms:

$$T_m^n = T_m^{n-1} + A_L \left\{ \left[K_L + 4\bar{\varepsilon}_M \sigma s_L (T_m^{n-1})^3 \right] \left[T_{m+1}^{n-1} - 2T_m^{n-1} + T_{m-1}^{n-1} \right] + 3\bar{\varepsilon}_M \sigma s_L (T_m^{n-1})^2 \left[(T_{m+1}^{n-1})^2 - 2T_{m+1}^{n-1} T_{m-1}^{n-1} + (T_{m-1}^{n-1})^2 \right] \right\} , \quad (131)$$

$$A_L = \frac{\Delta t}{\rho_L c_L (\Delta x)_L^2} , \quad (132)$$

$$K_1 \left[\frac{-T_2^n + 4T_1^n - 3T_o^n}{2(\Delta x)_1} \right] + 4\bar{\varepsilon}_M \sigma s_1 \left(\frac{T_1^n + T_o^n}{2} \right)^3 \left(\frac{T_1^n - T_o^n}{(\Delta x)_1} \right)$$

$$= \bar{\varepsilon}_M \sigma (T_o^n)^4 - \bar{\varepsilon}_M I(\xi, n, t) , \quad (133)$$

$$T^{n}_{m,L+1} = T^{n}_{m,L} \quad , \tag{134}$$

$$T_m^{\,n} = T_m^{n-1} + B\left\{\left[K_{L+1} + 4\bar{\varepsilon}_M \sigma s_{L+1}\left(\frac{T^{n-1}_{m+1} + T^{n-1}_{m}}{2}\right)^3\right]\left[\frac{T^{n-1}_{m+1} - T^{n-1}_{m}}{(\Delta x)_{L+1}}\right]\right.$$

$$\left. - \left[K_L + 4\bar{\varepsilon}_M \sigma s_L\left(\frac{T^{n-1}_{m} + T^{n-1}_{m-1}}{2}\right)^3\right]\left[\frac{T^{n-1}_{m} - T^{n-1}_{m-1}}{(\Delta x)_L}\right]\right\} , \tag{135}$$

and

$$B = \frac{4\Delta t}{(\rho_L c_L + \rho_{L+1} c_{L+1})\left[(\Delta x)_L + (\Delta x)_{L+1}\right]} \quad . \tag{136}$$

In the absence of radiative conductivity, the well-known stability criterion of $A_L \leq 0.5$, as described, for example, by Hildebrand[29] or Richtmyer,[30] limits the time interval Δt between successive temperature distributions. We have found that when at a given temperature the radiative flux is greater than the conductive flux, the stability criterion can be 0.25 or even less.

In each of our calculations, an initial temperature distribution has been assumed for a given position on the lunar surface. The deepest point in the Moon is chosen so far in that it does not affect the surface temperature at any time, and is held at a constant value, usually 230°K when not far from the subsolar point. After the integration of a complete lunation is performed, which usually takes about one minute on the IBM 7094 at the Harvard Computing

Center, the temperature distribution is accurate, as calculations for several lunations show, to within 1°K to depths in excess of that to which the thermal wave can propagate during an eclipse. Using this initial temperature distribution and computed values of f(t), we compute the temperature distributions during the penumbral and umbral stages of eclipse.

Unless otherwise stated, our cooling curves are computed for the crater Tycho ($\xi = -0.685$, $\eta = -0.140$), and on the assumption that $\bar{\varepsilon}_M = 0.93$. In computing each model we have specified the diffusivity $\alpha = K/\rho c$, rather than the more familiar thermal parameter $\gamma = (K\rho c)^{-1/2}$, since α is the relevant parameter in the heat conduction Eq. (126), if one wishes to specify the distance scale of layers in dimensional terms.* For comparison with previous work the values of α were chosen to give convenient values of γ when c is assumed to be 0.20 cal $gm^{-3}{}^{\circ}K^{-1}$ and ρ to be 1 gm cm^{-3}, typical values from Wechsler and Glaser. Table V presents the values of the diffusivities, conductivities, and thermal parameters used for the various cooling curves.

---

*In a discussion of homogeneous models, where the depth variable is arbitrary, it is advantageous to rewrite the above equation in terms of a new depth variable $y = x/\ell_T$, where $\ell_T = \sqrt{4\pi K_D/\rho c}$ is the wavelength of the first harmonic in a Fourier expansion of the thermal wave in the lunar surface. Wesselink has shown that when this transformation is made, the relationships among the relevant parameters are homologous.

TABLE V

THERMAL PROPERTIES FOR COMPUTED COOLING CURVES

Diffusivity, $cm^2\ sec^{-1}$	Assumed conductivity, K $cal\ cm^{-1}{}^{\circ}K^{-1}\ sec^{-1}$	Thermal parameter $cal^{-1}\ cm^2\ {}^{\circ}K\ sec^{-1/2}$
1.11×10^{-3}	2.22×10^{-4}	150
4.00×10^{-4}	8.00×10^{-5}	250
2.05×10^{-4}	4.10×10^{-5}	350
1.00×10^{-4}	2.00×10^{-5}	500
4.44×10^{-5}	8.92×10^{-6}	750
3.91×10^{-5}	7.81×10^{-6}	800
3.09×10^{-5}	6.17×10^{-6}	900
2.50×10^{-5}	5.00×10^{-6}	1000
1.90×10^{-5}	3.79×10^{-6}	1150
1.60×10^{-5}	3.21×10^{-6}	1250
1.11×10^{-5}	2.22×10^{-6}	1500

For direct comparison with observed temperatures, all of the calculated surface temperatures have been reduced to brightness temperatures by considering the decrease in apparent blackbody temperature that results from a change in irradiance by a factor of $\bar{\varepsilon}_M$ through our wide-bandpass filter (Figure 10). We have plotted these cooling curves as a ratio of temperatures to initial temperatures, $T_M/T_{M,max}$, as a function of t/t_o, with t_o the duration of the penumbral phase (56 minutes for the crater Tycho in the December 18-19, 1964 eclipse).

b) Discussion of Two-Layer Temperature-Independent Models

The simplest model of the lunar surface, that which assumes thermal properties independent of depth and temperature, as well as horizontal homogeneity and high spatial resolution, was originally investigated by Wesselink and Jaeger. Although this completely homogeneous model is an obvious over-simplification, it does provide a convenient reference with which to compare observations and suggest the manner in which the model should be improved. We have computed such a family of cooling curves (presented in Figure 14,) using time intervals Δt between 120 and 360 seconds, and 30 points inside the surface ranging from a maximum depth of 25 cm for $\gamma = 1500$ to 70 cm for $\gamma = 250$. Figure 14 includes the computed pre-eclipse brightness temperatures $T_{M,max}$ as an indication of the manner in which they depend upon the models. Enough significant figures are given to show the dependence of these temperatures on the model, but the differences are much smaller than the uncertainties in their absolute values because of uncertainties in lunar emissivity, solar constant, etc.

The observed temperatures inside Tycho are also presented in Figure 14, along with an average of the observed temperatures 30" east and west of the crater

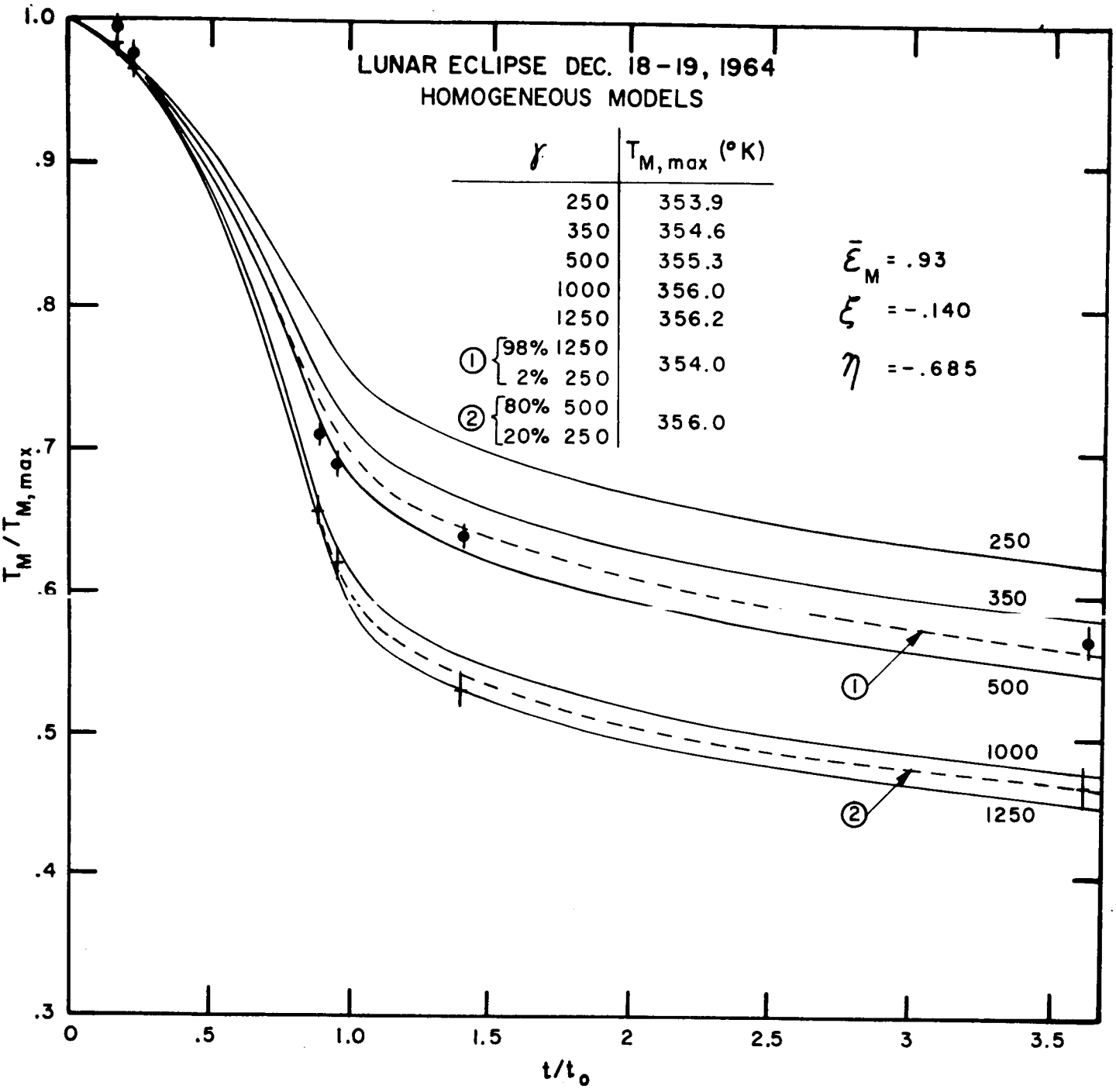

FIG. 14. Observed brightness temperatures inside the crater Tycho (·), and the average of temperatures 30" east and west of Tycho (+) are compared with a family of cooling curves for homogeneous models with temperature-independent thermal properties. The curves are computed for the orthographic coordinates of the center of Tycho (ξ = -.140, η = -.685) and for the indicated radiant emissivity. The resulting theoretical pre-eclipse temperatures $T_{M,max}$ given in the Table are given to much higher accuracy than is warranted by the measured values of absorbed insolation, in order to show the dependence of $T_{M,max}$ upon the particular model. Estimated time errors are less than 1.5 minutes.

(hereafter called "the environs of Tycho"). The path of each scan through Tycho is shown in Figure 15. Our deduced relative temperatures are systematically 3.5 to 4% higher than those obtained by Sinton[31]. In part this may result from the use of different methods of determining the atmospheric transmittance, but more probably it results from his larger resolution element of 27.9" and the concomitant smearing of significant detail.

As previous investigations have shown, the completely homogeneous model produces cooling curves which decrease more rapidly during the umbral phase of eclipse for anomalous craters than is observed. Our data for Tycho and its environs tend to corroborate this generalization although a completely homogeneous model for the environs of Tycho is not ruled out. This suggests that we must reconsider one or more of these simpliciations if we are to obtain a more realistic model for the lunar surface.

As a simple refinement upon these completely homogeneous models, we relax the condition of horizontal homogeneity. Such models as, for example, that shown in Figure 14 show that when we consider a fraction of the lunar surface composed of "bare rock" of higher diffusivity, the slope of the cooling curve throughout totality is changed only very slightly. Therefore simple models that are homogeneous in depth but postulate a variety of surface materials will not fit our data for Tycho or its environs.

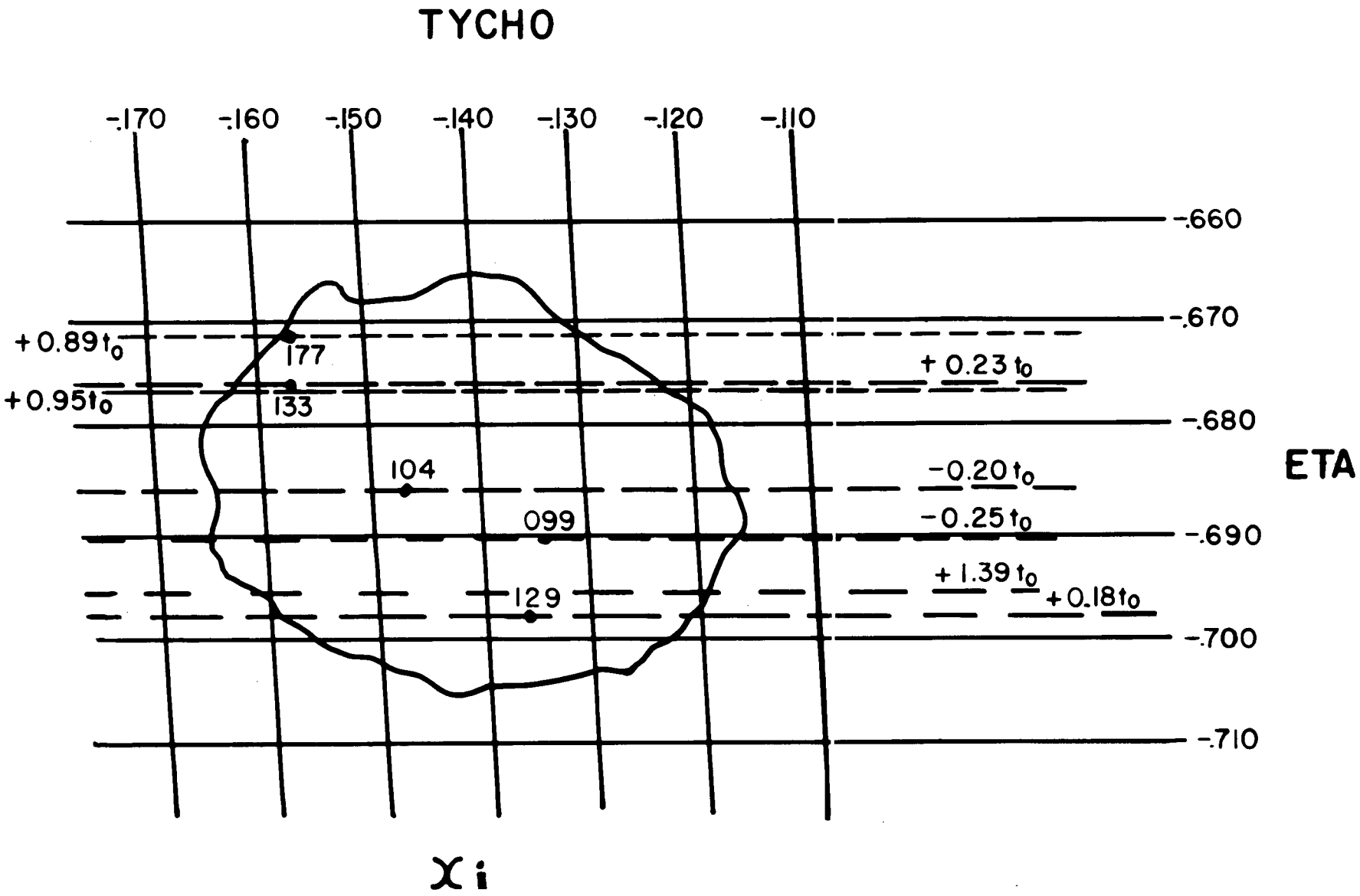

FIG. 15. Paths of seven scans (dashed lines) through the crater Tycho during the lunar eclipse of December 18-19, 1964. The positions labeled with photographic frame numbers on five of these scans correspond to coordinates determined from identified photographs. The paths of the other two scans are defined by photographs taken elsewhere along these scans. The orthographic coordinate grid is superimposed. For each scan, the time of passage through Tycho is given in terms of t_o, the duration of penumbral eclipse at Tycho. Photographs taken during the final scan ($t = 3.65\ t_o$) do not allow a precise determination of the path but do place the scan within the crater.

Jaeger and Harper have computed a family of cooling curves using two-layer models, with each layer characterized by different thermal properties, assuming the relationship between the top layer depth d and the temperature-independent thermal properties of the top and bottom layers (primed quantities) derived by Piddington and Minnet:

$$d = 610\ K(K'\rho'c')^{-1/2} \quad . \tag{137}$$

One of Jaeger and Harper's curves comes close to fitting the data obtained by Pettit[32] for an upland area on the edge of Mare Vaporum ($\xi = 0.0$, $\eta = 0.17$).

The addition of a substrate of higher diffusivity affects the eclipsed surface temperature in two ways. First, its higher thermal inertia and consequently greater thermal phase lag with respect to insolation increases the phase lag at the base of the top layer. For regions of the lunar surface in which the interface is heating up, that is, primarily West* of the subsolar meridian, the interface will be colder than at a similar depth for a homogeneous model consisting of upper-layer material. Since the radiating boundary demands a specified outward flux which, with the heat capacities, determines the thermal gradient in both

---

*According to the astronomical convention, West is defined as the direction perpendicular to the lunar axis of rotation from the lunar sub-earth point towards Mare Crisium. Thus the sun rises in the West on the Moon.

layers, the surface temperature must be colder for two-layer models in which the source of heat is the internal energy of the upper layer. This effect is readily apparent in Figure 16 for those models with thick upper layers, and especially in Figure 17 where the temperature distribution beneath the surface is plotted for three models at three times: at the beginning and at the end of penumbral eclipse, and near the end of umbral eclipse.

On the other hand, when the advancing thermal wave reaches the interface, heat is withdrawn from a region of high thermal conductivity and the surface temperature falls more slowly. For thin upper layers this manifests itself in an abrupt levelling out of the cooling curves at the end of penumbral eclipse, while for a very thick upper layer (a centimeter or more deep) such an effect cannot manifest itself during an eclipse but is observable during a lunation.

If one ignores the condition expressed by equation (137), the existence of three independent variables (the diffusivities α_U and α_L of the upper and lower layers, and the thickness of the upper layer) introduces the possibility that a great many models can exhibit very similar eclipse cooling curves. It is also possible that the curves may be insensitive to values of one or more of the parameters. For the case of a moderately thick upper layer, that is, one for which the cooling curve deviates

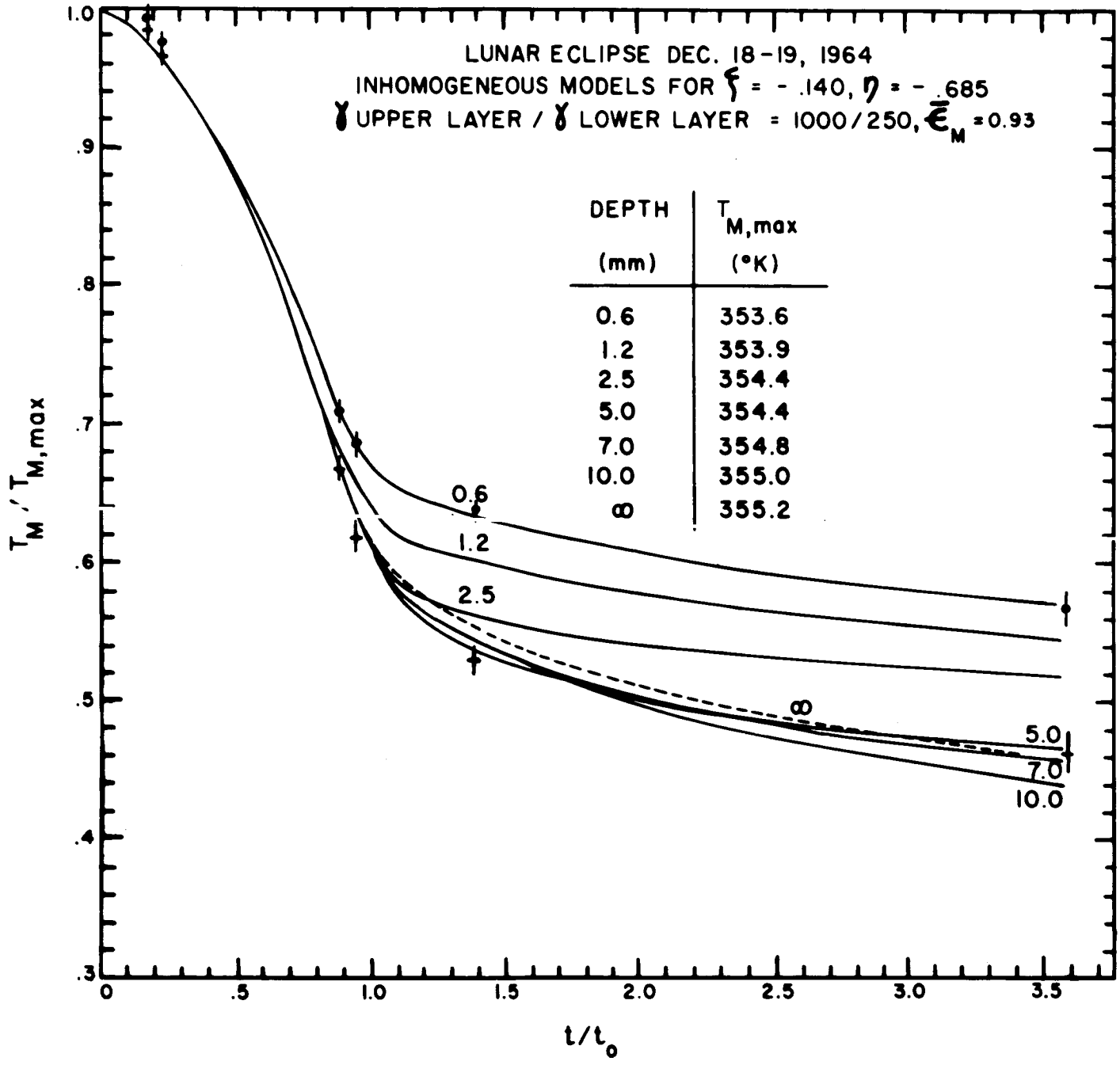

FIG. 16. Observed temperature ratios for the crater Tycho and its environs; (·) inside the crater, (+) environs of crater. The family of theoretical cooling curves is computed for two-layer models with temperature-independent thermal properties. The thermal parameters γ, radiant emissivity $\bar{\epsilon}_M$, and upper layer depths are indicated.

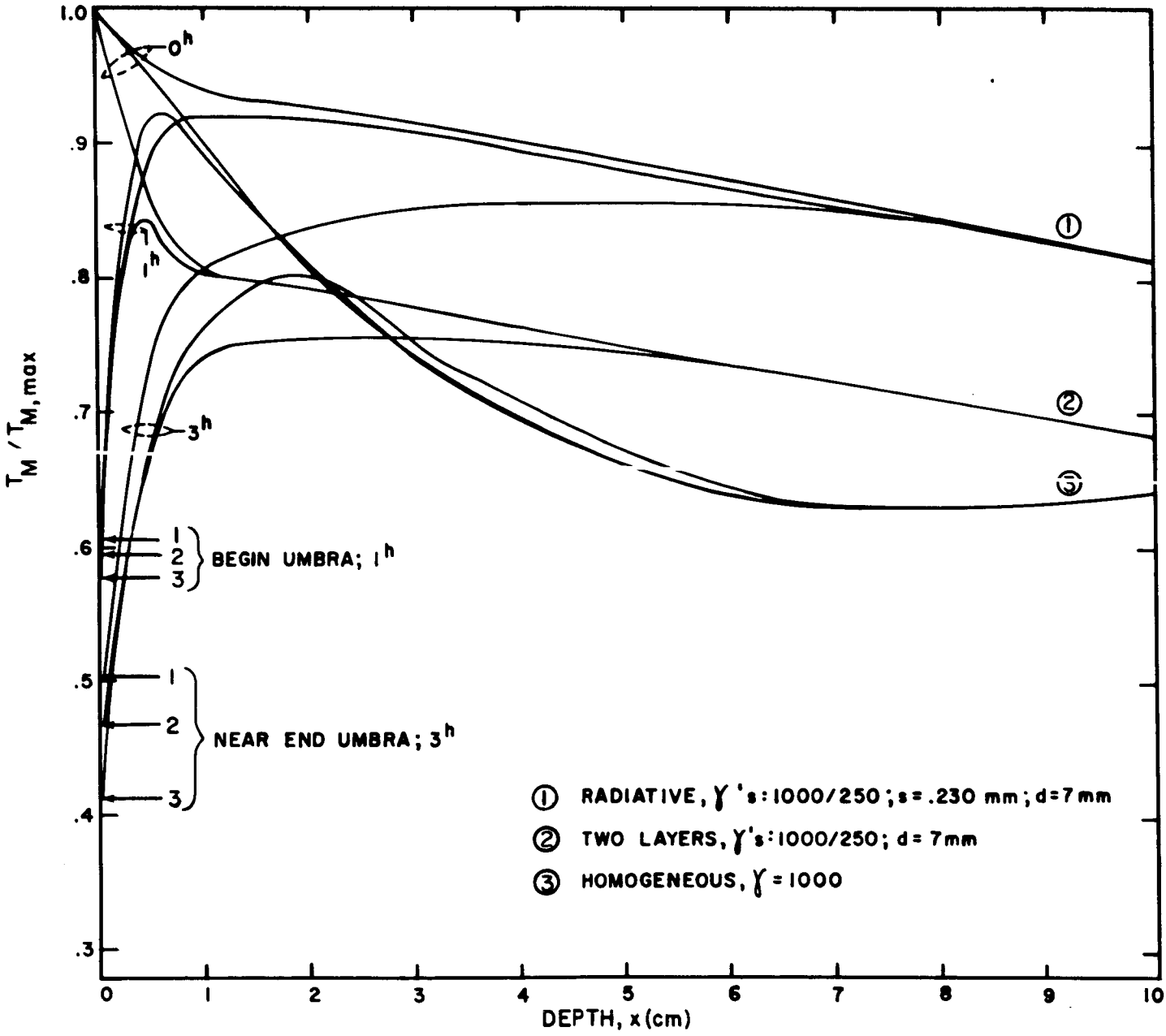

FIG. 17. A comparison of the predicted internal temperature distribution for three different models, during a lunar eclipse. The temperature distributions are given as ratios to the pre-eclipse surface temperatures. The thermal properties are taken to be temperature-independent except that a radiative component to the conductivity is included in the upper layer of the radiative model. These models are computed for the lunar coordinates of Tycho and for $\bar{\varepsilon}_M = 0.93$. The temperature distributions are given at $t = 0.00t_o$, $1.07t_o$, and $3.22t_o$ in order of decreasing surface temperature.

from the homogeneous case mainly during the umbral phase of eclipse, allowed values of α_U are bounded by the two conditions that the cooling curve for a homogeneous surface of the same thermal properties must be the same as or slightly above the observed temperature at the beginning of umbral eclipse, but significantly below it at the end of total eclipse. The data we have obtained for the environs of Tycho may be described in terms of such a model with the thermal parameter of the upper layer between 1000 and 1250. Figure 16 shows curves for two-layer models, which assume thermal parameters of 1000 and 250 for the upper and lower layers respectively, but assume variation in the thickness d of the upper layer. The data for Tycho itself may be described in terms of a model of the same materials but with a much thinner upper layer.

To investigate how the theoretical surface temperatures depend upon modifications of the model, we may take as standards the two models which agree well with the observational temperatures of Tycho and its environs, and systematically study the effect of changing each of the relevant parameters one at a time.

Our attention will be focused primarily upon models involving a moderately thick upper layer, which present and previous data indicate may characterize the anomalous craters and their environs.

Variations of α_U manifest themselves in a significant manner for models of moderate thickness and for completely homogeneous models, since it is only α_U which prevents a rapid decrease to very low temperature at the end of the penumbral phase of eclipse. The cooling curves for such models, shown in Figure 18, are parallel but are significantly displaced during totality with respect to one another, as a result of different thermal gradients in the upper layers required to support roughly the same conducted outward flux. Very thin layers exhibit this effect, but it is decreased in magnitude almost proportionally to the depth of the layer.

Models with the same α_U but different α_L are very interesting, in that the qualitative behavior shown in Figure 19 depends upon the upper layer thickness, d. If the layer is so thick that the thermal wave does not advance much farther into the surface than the interface, the effect of the lower-layer thermal inertia upon the material immediately above is important. Consequently, the curves for larger values of α lie below those for lower values. When the upper layer is so thin that the major source for radiance during total eclipse is the lower layer material, the curves for greater α_L lie above. In addition, for models with small d, α_L manifests itself directly in the slopes of the umbral cooling curves; the slope decreases as α_L increases, and the lower layer approaches the condition of a constant-

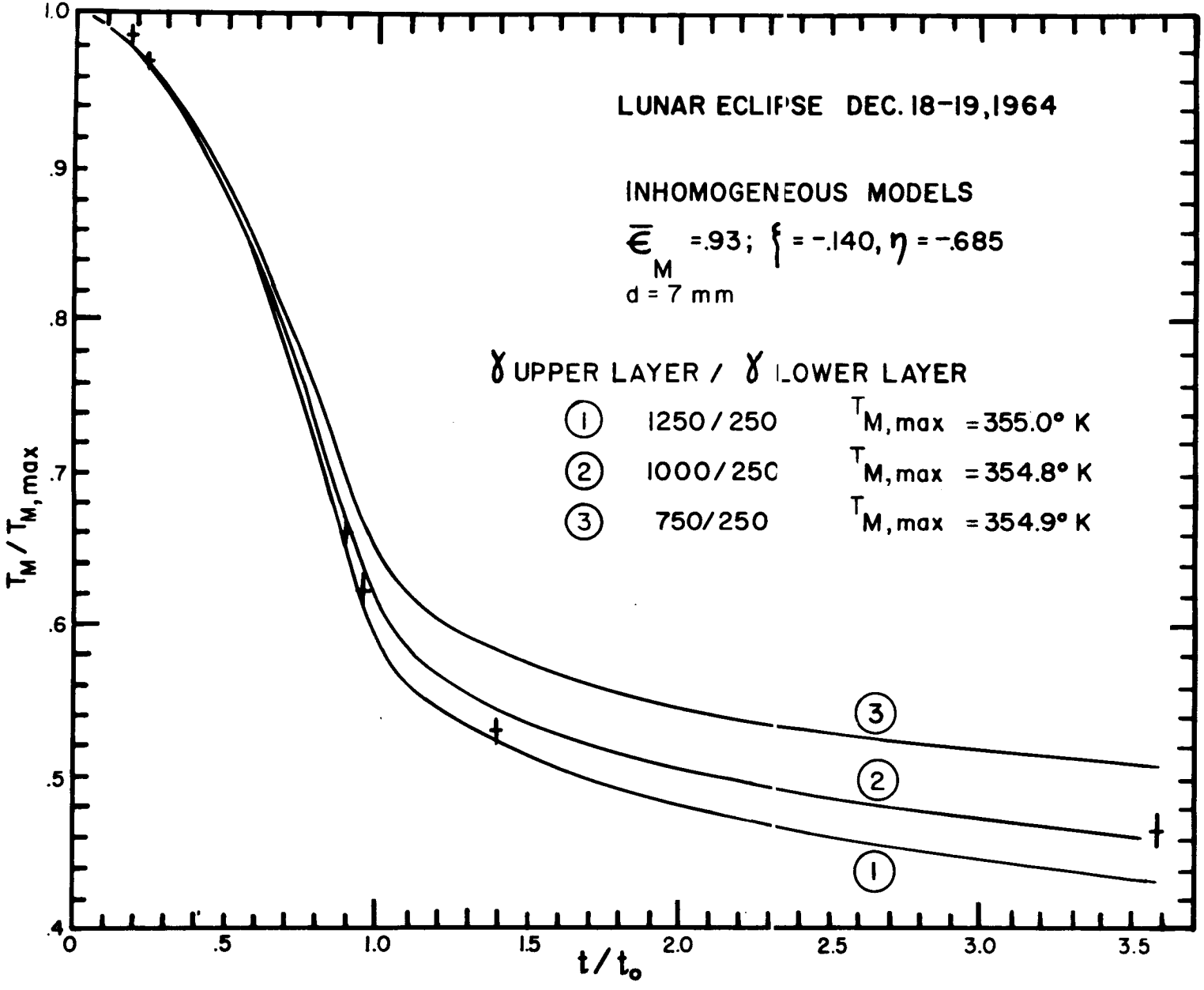

FIG. 18. Effect of varying the upper layer thermal parameter γ upon the two-layer theoretical eclipse cooling curves computed for the coordinates of the center of Tycho. Data obtained during the lunar eclipse of December 18-19, 1964 are plotted for the environs of Tycho (+).

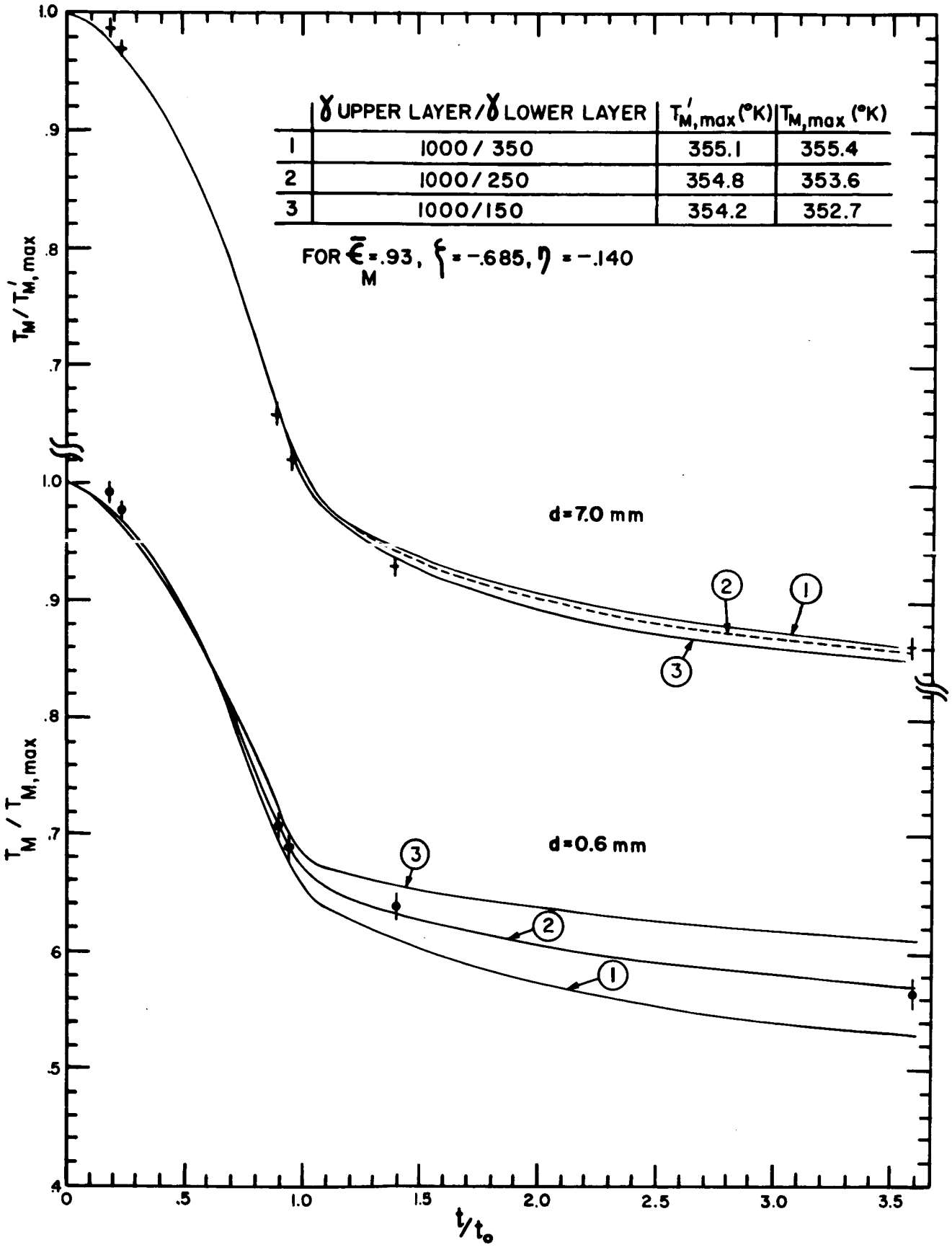

FIG. 19. Theoretical eclipse cooling curves for lower layers with different thermal parameters γ and for two different upper layer depths d. The plotted data pertain to Tycho (·) and its environs (+) and were obtained during the lunar eclipse of December 18-19, 1964.

temperature heat source. Thus for such anomalous regions as Tycho, with sufficiently accurate data one may be able to determine the diffusivity of the lower layer directly from relative measurements alone.

From these considerations, we conclude that the surface structure both in and around Tycho may be adequately, but not of necessity uniquely, described in terms of two different two-layer models, both of which consist of the same two materials (thermal parameters of 1000 and 250). and which differ only in the thickness of the upper layer. As is apparent from Figure 16, the data for the environs of Tycho are consistent with upper-layer depths between 5 and 10 mm, but it is interesting to note that these parameters and an upper-layer depth of 7 mm satisfy the conditions of Piddington and Minnett. Further calculations show that only a limited range of α_U and depth can fit our data for the environs of Tycho, for example the values γ_U = 1150 and d = 4 mm also give a reasonable fit.

In order to apply these models to other features on the lunar surface, we must consider how changes in the initial temperature distribution and surface temperatures before eclipse affect the surface temperatures during eclipse. Since the loss of energy at the surface by radiation decreases rapidly with temperature, the relative umbral phase temperatures increase to the east and west of the

subsolar point. Thus we would expect that the crater Aristarchus, at 48°E selenographic longitude (ξ = -.685), would exhibit relatively higher umbral brightness temperatures than a crater of similar structure near the subsolar point. As we have already seen, significant changes in the cooling curve of two-layer models can result from changes in the interface temperature. The cooling curves for similar models east and west of the subsolar point should not be precisely the same. These effects, demonstrated in Figure 20, apparently have not been considered in previous studies, a fact that may in part explain the inability of Saari and Shorthill[33] to interpret eclipse temperatures inside Aristarchus.

A similar relative increase in umbral-phase surface temperatures occurs toward high latitudes (see Figure 21). This results from an initial temperature distribution which approaches a constant value independent of depth, and from the less efficient radiating boundary. Thus, for comparison of infrared eclipse data with theoretical predictions, one must compute cooling curves for the particular lunar region investigated. The very slight differences in many cases between umbral-phase temperatures of radically different models do not permit the use of one set of models computed for the subsolar point for comparison with data obtained elsewhere.

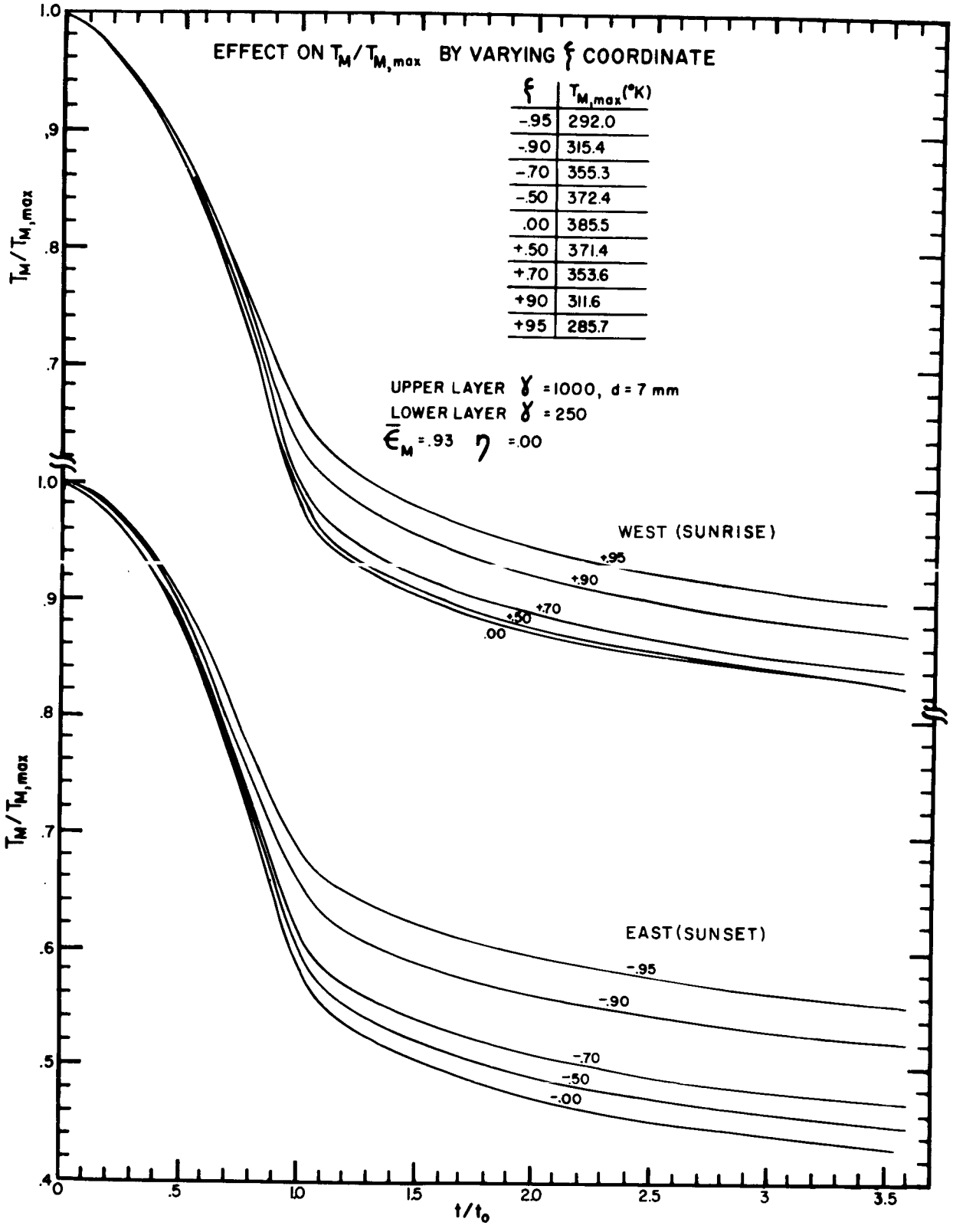

FIG. 20. Theoretical eclipse cooling curves for a two-layer model are given for a range of lunar orthographic coordinate ξ. Note that umbral temperatures east of the subsolar point are significantly higher than those west.

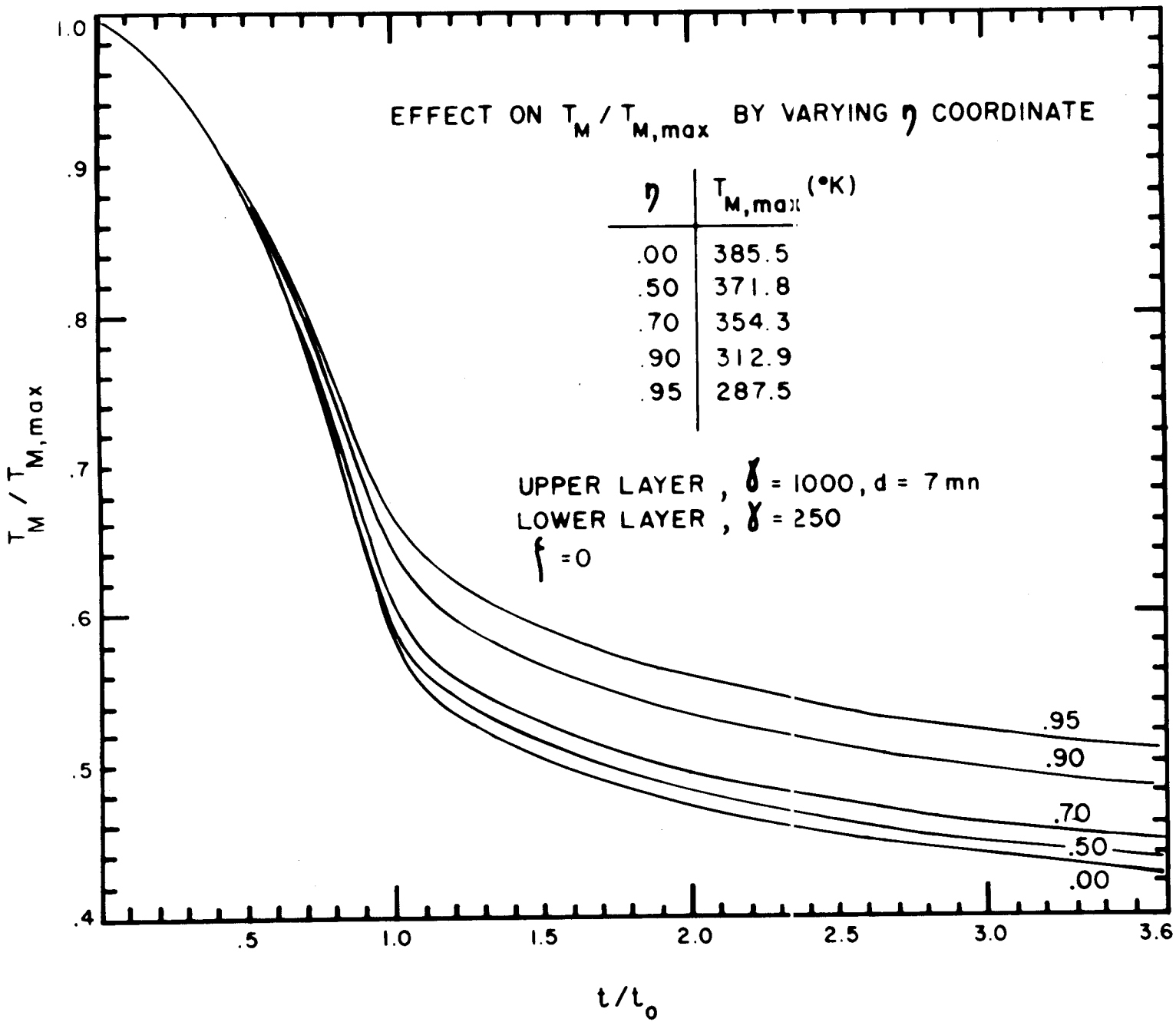

FIG. 21. Theoretical eclipse cooling curves for a two-layer model are given for a range of lunar orthographic coordinate η.

We have computed cooling curves for another region of the lunar surface, the crater Copernicus. These curves, together with the measured temperature of Copernicus and its environs, are presented in Figure 22, and the path of each scan is shown in Figure 23. Unfortunately, no measurements were made far into totality, where a more precise distinction between different models is possible.

In investigating the degree to which absolute as opposed to relative temperature measurements are necessary for obtaining the thermal properties of the lunar surface, we must distinguish among three effects. A positive error in the assumed temperature of the subsolar point, resulting from inaccurate values of the absorbed solar flux, is analogous to the effect of displacing the observed lunar feature in η toward the equator. A negative error has the reverse effect. As we have seen, a decrease in the absolute value of η displaces the relative umbral temperature downwards.

Secondly, systematic errors in the measured irradiance do not appear in a one-to-one manner in the derived temperatures, but are more significant at 350°K than at 200°K, as shown previously in Figure 13. Thus, systematically low flux measurements will increase the relative umbral temperatures, but the increase will not be as great as that produced if we assume an absorbed solar flux that is correspondingly low. For example, a relatively large

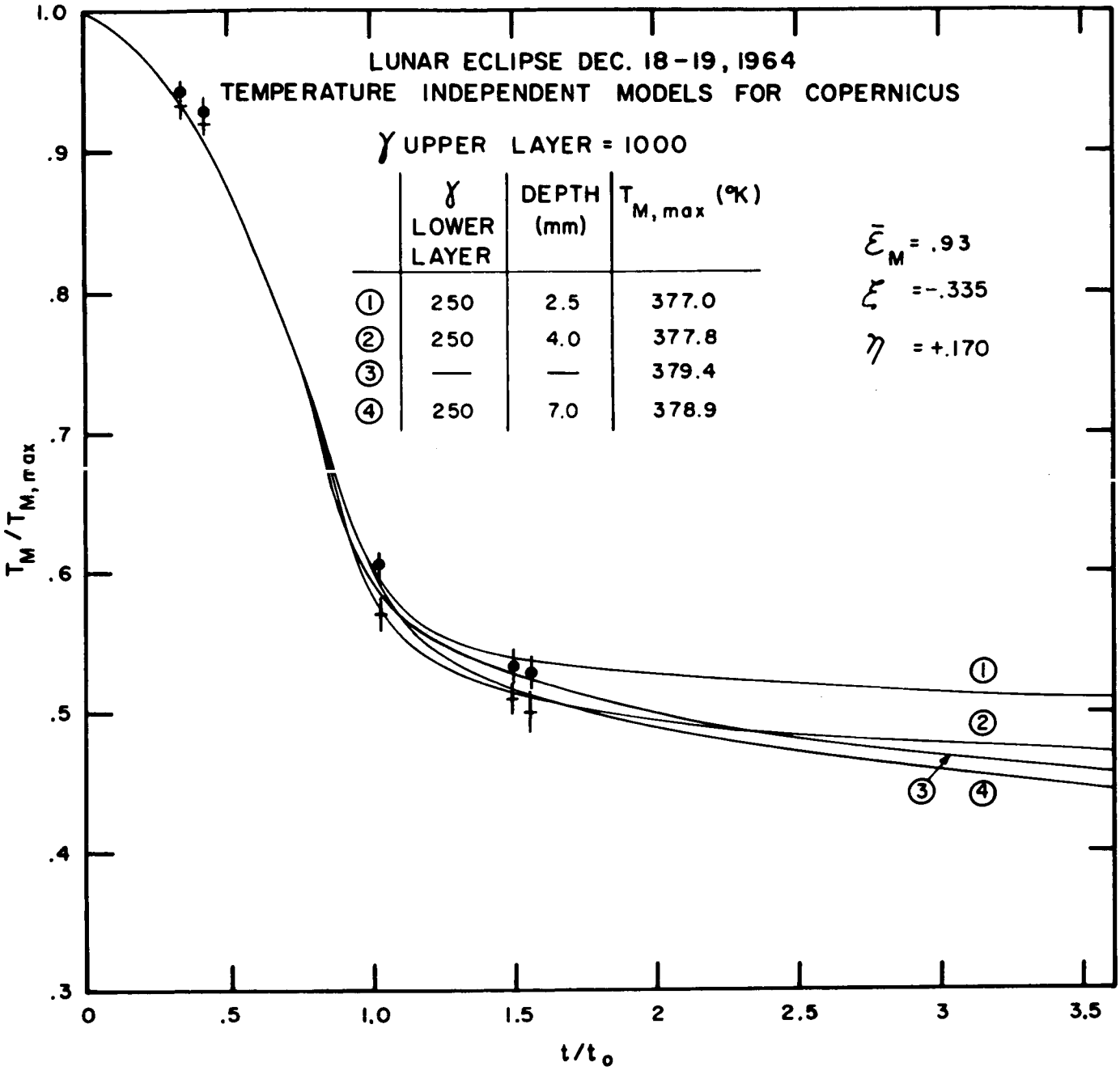

FIG. 22. Data obtained during the lunar eclipse of December 18-19, 1964, for the crater Copernicus (·) and its environs (+), with theoretical eclipse cooling curves for homogeneous and two-layer models, both with temperature-independent properties.

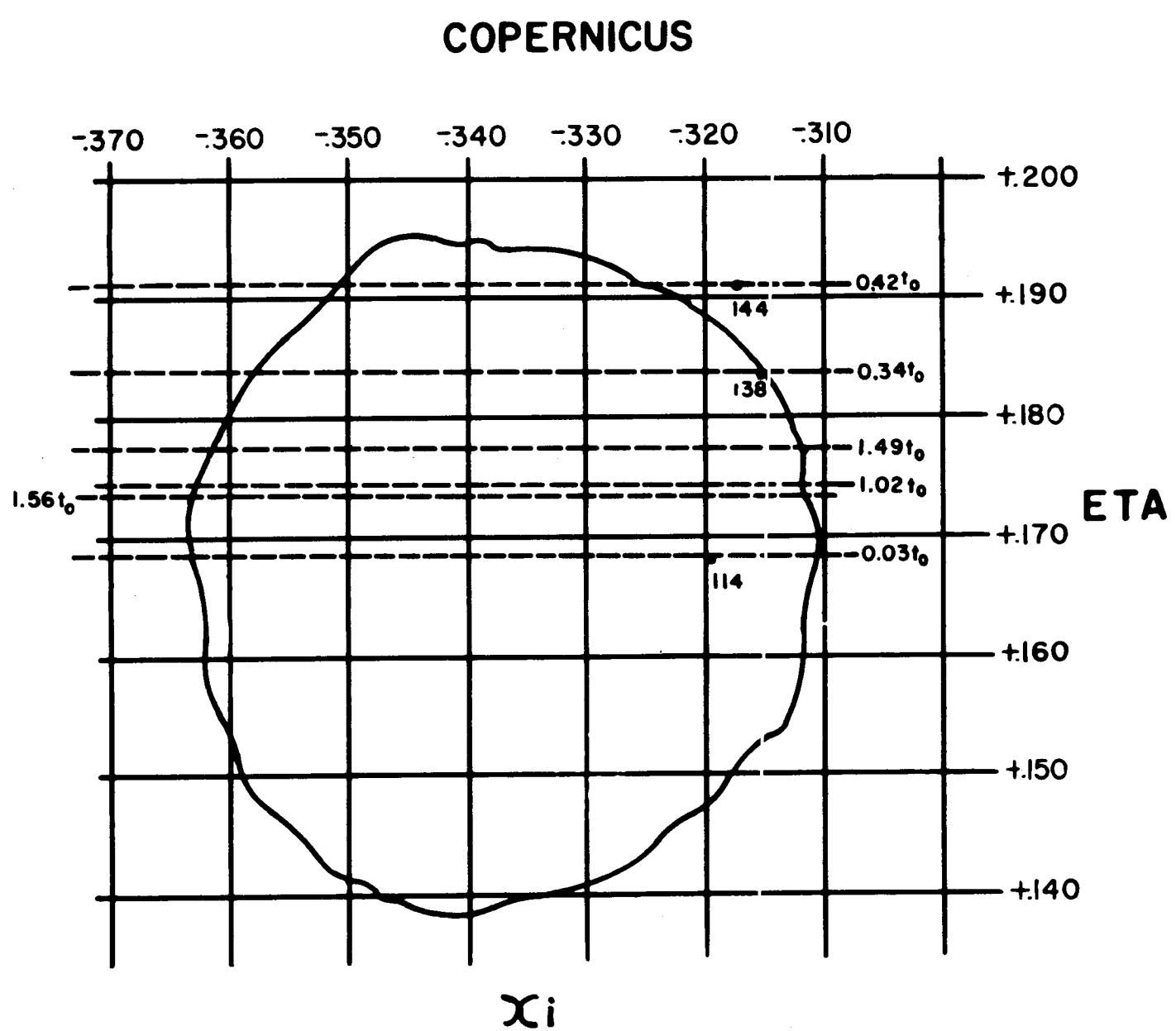

FIG. 23. Paths of six scans (dashed lines) through the crater Copernicus during the lunar eclipse of December 18-19, 1964. The positions labeled with photographic frame numbers on three of these scans correspond to coordinates determined from identified photographs. The paths of the other three scans are defined by photographs taken elsewhere along these scans. The orthographic coordinate grid is superimposed. For each scan, the time of passage through Copernicus is given in terms of t_o, the duration of penumbral eclipse at Copernicus.

error in the subsolar point temperature, reducing it from 395°K to 380°K, which is a 13.3% error in assumed incident solar flux, increases the relative temperature from 0.463 to 0.477 at $t = 3.22\ t_o$ for our standard two-layer model. A similar systematic error in measured lunar irradiance, with the same model, increases this relative temperature from 0.463 to 0.469, about half as much. The discrepancy is about 3°K or 15% in lunar irradiance during the umbral phase.

While the incident solar flux may be accurate to about 1%, the bolometric albedo for typical and anomalous regions of the lunar surface is not known with this accuracy. A further complication is that the change in radiant emissivity with observation angle, as investigated by Geoffrion, Korner, and Sinton[34] for the subsolar point, leads to an 11% increase in radiant emittance for this region at full moon relative to the mean radiant emittance. Thus, an error in theoretical temperature for the subsolar point of 10 or 15°K is not inconceivable, and the resulting inaccuracies in lunar thermal properties should be taken into account.

The third effect is that for the same surface temperature but different mean emissivity of the surface material in the infrared, the rate of thermal emission varies. A 0.05 change in this emissivity causes a change of 0.0083 in relative temperatures at the end of umbral

eclipse for the standard model. The change is negative for $\bar{\varepsilon}_M = 0.98$, corresponding to temperature differences of $\pm$ 3°K or, again, a $\pm$ 15% change in observed umbral irradiance.

c) Temperature-Dependent Properties

Since one-and two-layer temperature-independent models have apparently been successful in accounting for eclipse and radio observations, and since a multitude of plausible mechanisms have been postulated to account for the formation of an upper "dust" layer of variable thickness across the lunar surface, there has been little motivation for introducing the mathematical complications of temperature-dependent thermal properties.

Murray and Wildey have recorded brightness temperature down to their instrumental noise level of 105°K, in the course of many scans up to 8 days into lunar darkness. They are unable to fit the observed rate of decrease of temperature with time, the quantity most nearly independent of systematic errors, to any completely homogeneous models they have calculated. They speculate instead that horizontal variations in the conductivity such as "bare outcrop of boulders on the surface" might give a better fit. As is apparent in their Figure 8 and from our calculations in Figure 24, such completely homogeneous models have cooling curve slopes which are slightly less steep than is consistent with the data. If a few percent

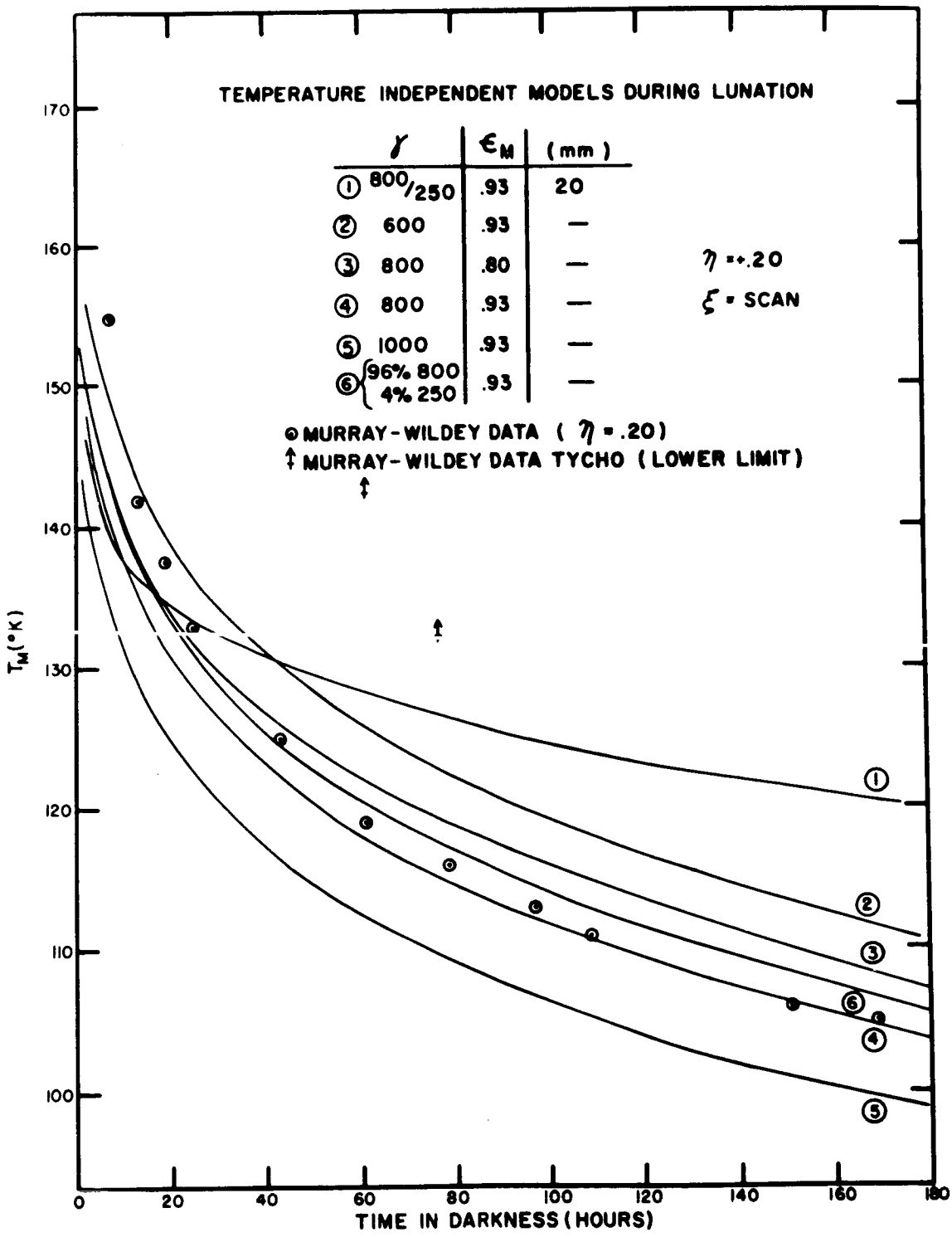

FIG. 24. Computed surface brightness temperatures for models with temperature-independent thermal properties are compared with the data of Murray and Wildey. These temperatures are computed for a point at the mean orthographic coordinate of their scans, η = +.20, in terms of the number of hours after the passage of the evening terminator. In accordance with the suggestion of Wildey, these data points have been shifted 5 hours closer to the terminator. The brightness temperatures for the crater Tycho are lower limits, because of uncertainties in position determination on the lunar surface.

of the surface material is of higher diffusivity (see Figure 24), the slope of the nighttime cooling curve decreases further. In addition, two-layer models in which the depth of the upper layer is shallow enough to be apparent during a lunation, that is, less than 6 cm, also have slopes which are less steep than single-layer models, and thus are inconsistent with the data.

Before we proceed we should consider alternative explanations for the observed steepness of lunation cooling curves. With Murray and Wildey's spatial resolution of 26" and a probable positioning error of two or three times this resolution limit, their data for regions within 12 hours of the sunset line should not be given much weight. Wildey[35] suggests that their determination of the terminator is probably in error by 5 hours in the sense of reducing the observed brightness temperature at the terminator. When such a time correction is applied to their data, it approximates better the predictions of homogeneous models.

Their final temperatures were measured very close to the limb and should be revised upward if limb darkening is important. An upper limit to this revision can be estimated from the observed 30% reduction (Geoffrion, Korner, and Sinton) in the measured radiant emittance from the subsolar point when it is at the limb as compared to its mean value. At 105°K and for our wide-bandpass filter,

this corresponds to about a 3°K surface temperature increase at the end of their scans. The data would then be brought into agreement with two-layer temperature-independent models that have upper and lower thermal parameters γ of roughly 800 and 250 and a depth of 4 centimeters. However, the effect of limb darkening is probably much less than 3°K near the limb. The effect of small-scale surface roughnesses upon the insolation is probably the major cause of limb darkening at the subsolar point, and a rough unilluminated surface should approximate a blackbody. It should also be noted that Murray and Wildey's scans covered both upland and mare regions, but they find no large-scale selenographic variations to suggest that their data should be interpreted other than in terms of the "time variation of temperatures at a single point."

Assuming that none of these postulated mechanisms is able to explain away the rapid decrease of temperature that occurs between 12 and 160 hours into lunar night, we are forced to construct models with temperature-dependent thermal properties. Radiative conductivity is one mechanism that would account for a decrease in conductivity at low temperatures, which in turn would produce the more rapid decrease in temperature during lunar night. At the same time, however, such a model would have high conductivity during the lunar day, and thus temperatures between 2 and

10 cm below the surface that are significantly higher than if this heat transfer mechanism were unimportant. This is shown in Figures 17 and 25. This excess internal heat is almost entirely lost just before sunset and so plays no role in explaining nighttime observations, but it produces high surface temperatures near the sunset terminator, which should be observable.

In Figure 26 we have plotted the surface temperatures, again reduced for an assumed emissivity $\bar{\epsilon}_M$ = 0.93 for several models with different K, and R, the ratio of radiative flux to conducted flux at 350°K. Each model exhibits the requisite slope: thus if radiative conduction is important for lunar surface materials, it is difficult to separate the effects of the conductivity from those of the effective spacing, s. An increase in s mimics a decrease in K. As in the temperature-independent models, the introduction of a lower layer of higher diffusivity decreases the rate of surface cooling when heat begins to be withdrawn from the lower layer itself. Thus we can say that if such a lower layer exists, it is probably more than 6 cm down. Considering γ to be defined in terms of the thermal conductivity excluding its radiative component, we find that values of γ between 900 with s between 300 and 600 microns, and 1000 with s about 1000 microns, could be considered consistent with the Murray and Wildey data. Measurements of the thermal conductivity of crushed

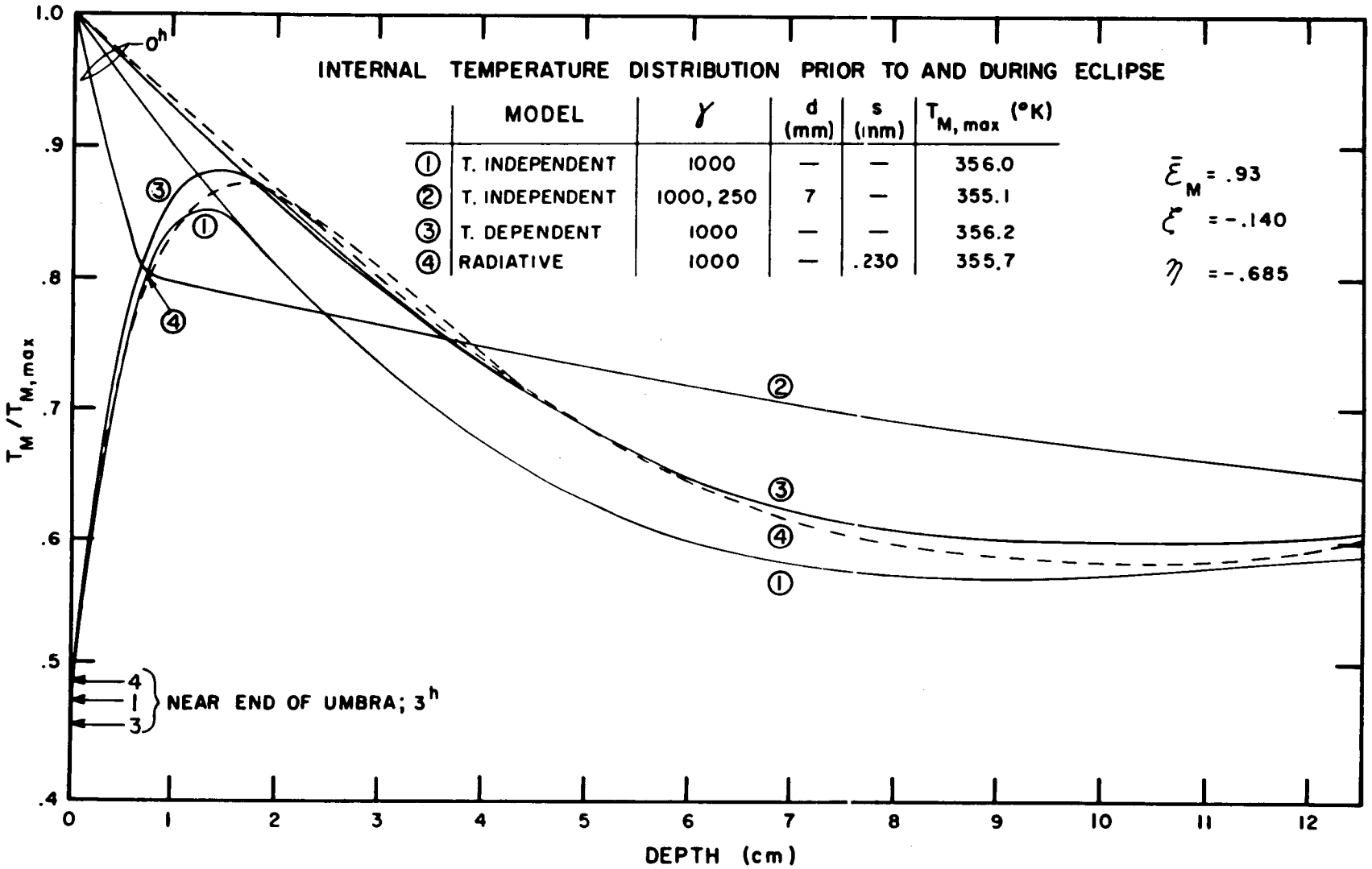

FIG. 25. A comparison of the predicted internal temperature distribution for four models prior to and near the end of the umbral eclipse at the crater Tycho. Note that the differences of temperature beneath the surface are larger than those at the surface, and that a high internal temperature and a low surface temperature are not inconsistent.

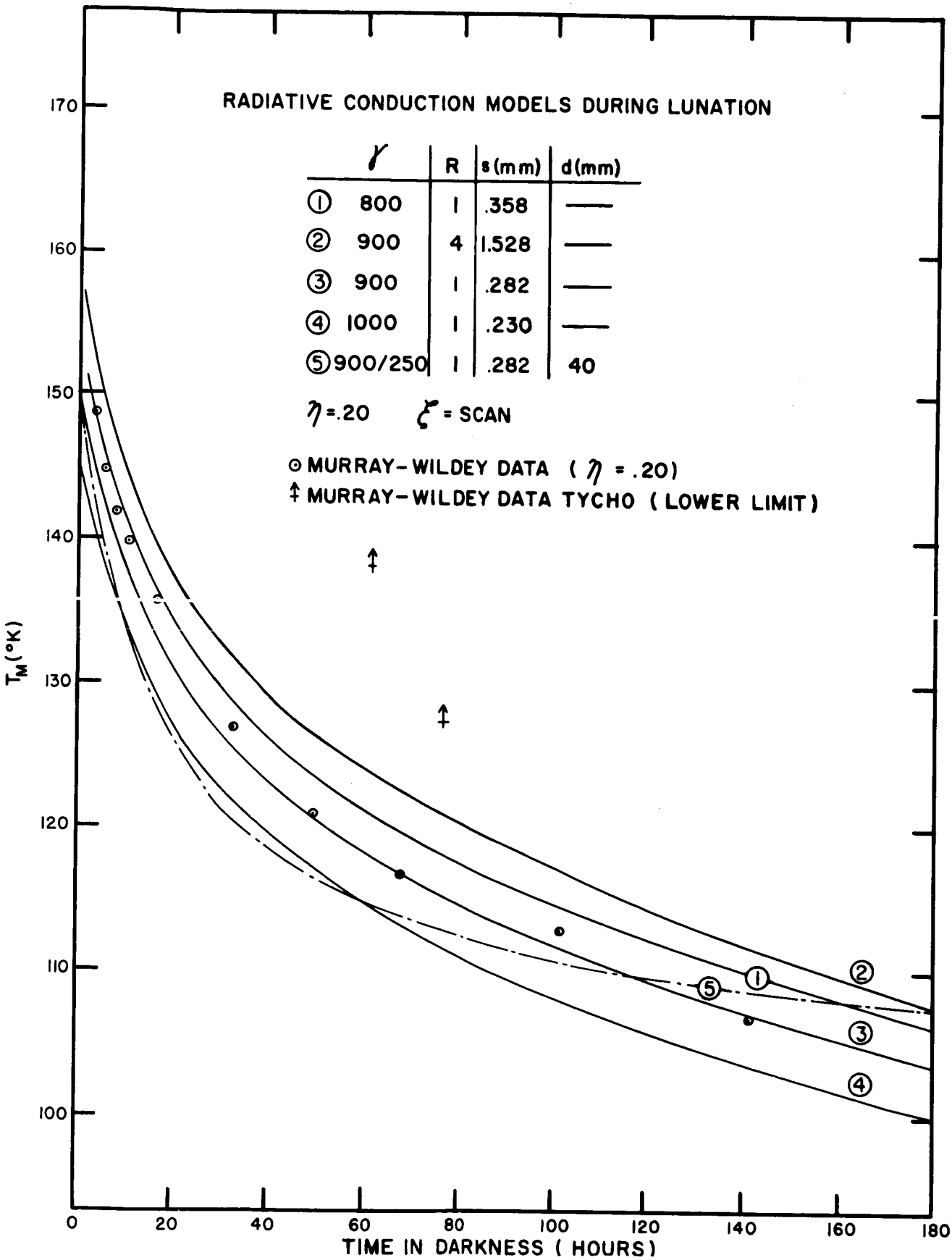

FIG. 26. Computed surface brightness temperatures for models including a radiative component to the conductivity. R is the ratio of radiative to conductive flux at 350°K, s is the effective mean spacing for radiative transfer beneath the surface, and d is the upper layer depth for a two-layer model. The value of γ characterizes the thermal parameters if there is no radiative transfer.

basalt powder, cited by Buettner[36], support the assumption of a T^3 term in the conductivity with a distance scale s = 1000 microns. With our assumed values of ρ and c, his results suggest values of γ near 750.

Eclipse cooling curves, shown in Figure 27, computed using homogeneous radiative models fit the data for Tycho and its environs about as well as do homogeneous temperature-independent models. The internal temperature distributions, shown in Figure 25, for these two models are significantly different, however. In order to match precisely the observed cooling curve slopes again, two-layer models are necessary.

To our knowledge the only attempt in the literature to investigate the effects of temperature-dependent thermal properties other than radiative conductivity is the work of Muncey[37,38]. He has assumed that both the specific heat and the conductivity are directly proportional to the absolute temperature. His assumption is suggested by the tendencies of the specific heats of silicates to increase with temperature and by the measurements by Scott[39] of the thermal conductivity of 80-mesh powdered perlite under vacuum conditions.* The measurements of the thermal

---

*These measurements are clearly inadequate for our case since they consist of two sets of observations, the mean conductivity between 20°K and 76°K (below lunar temperatures) and the mean conductivity between 76°K and 304°K (a range of temperatures large enough to render the resulting number meaningless for our purposes).

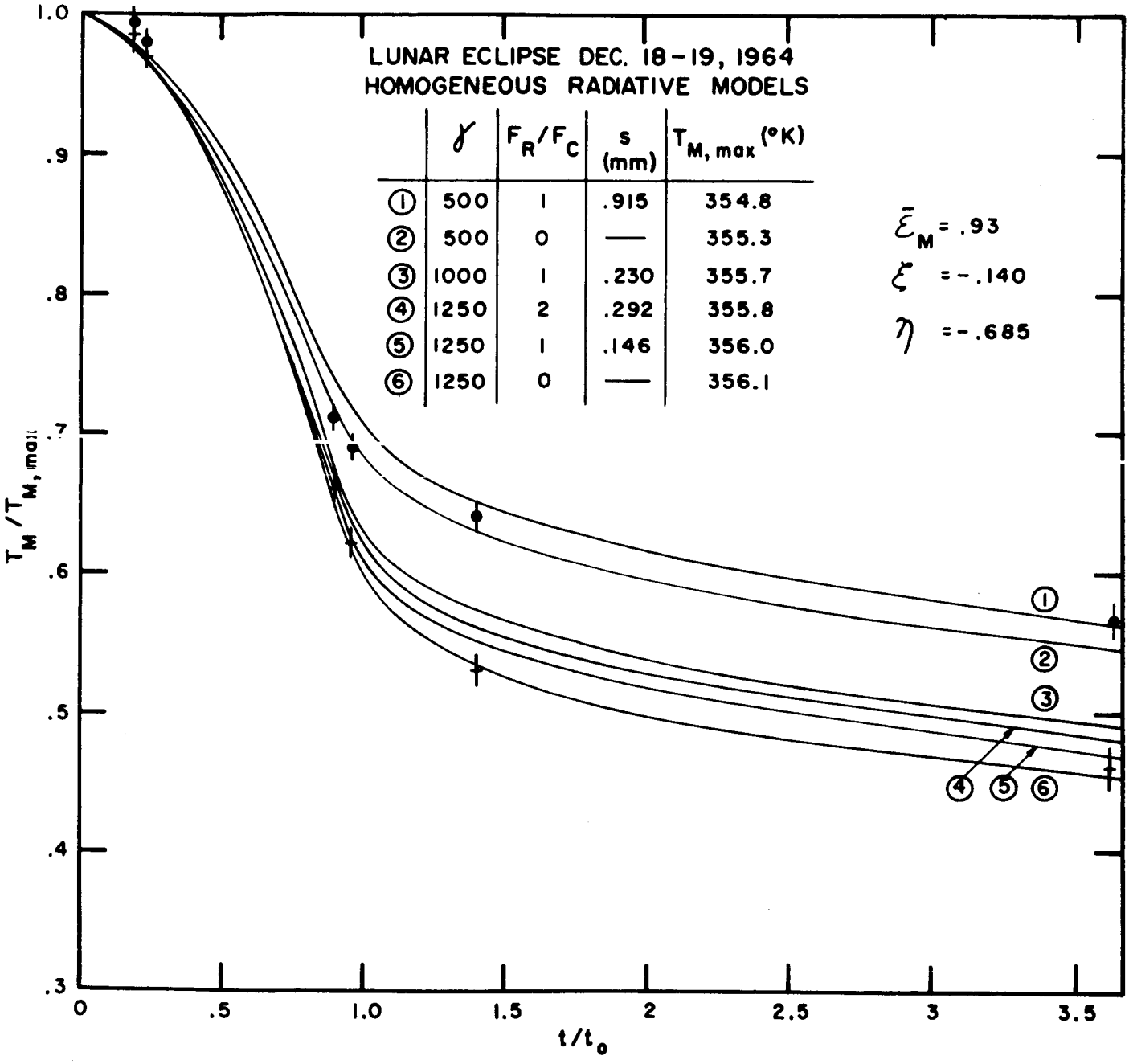

FIG. 27. Computed ratios of surface brightness temperatures to their pre-eclipse values for models including a radiative component to the conductivity. The meaning of the parameters is the same as in Figure 25.

conductivity of crushed olivine basalt by Bernett et al.[40] showed a decrease with temperature under high vacuum conditions, but Bernett et al. explained them in terms of radiative transport in the holes of the material, and made no measurements below 203°K. Measurements of the thermal conductivity of possible lunar materials under high vacuum and over the lunar range of temperatures are urgently needed.

In order to investigate the qualitative effects of temperature-dependent properties we have assumed, as has Muncey, the specific heat and the conductivity to be of the forms

$$c = c_o T \quad , \qquad K = k_o T \quad , \tag{138}$$

which lead to the heat conduction equation

$$\rho c_o T = \frac{\partial T}{\partial t} = \frac{\partial}{\partial x}\left(k_o T \frac{\partial T}{\partial x}\right) . \tag{139}$$

Using difference methods as before, one may write the heat conduction equation in the material (140) and at a boundary (143); the interlayer boundary condition (142), and the surface boundary condition (145), as follows:

$$T_m^{\,n} = T_m^{n-1} + A_L\left\{(T_{m+1}^{n-1} - 2T_m^{n-1} + T_{m-1}^{n-1}) + \frac{1}{4T_m^{n-1}}\left[(T_{m+1}^{n-1})^2 - 2T_{m+1}^{n-1}\,T_{m-1}^{n-1} + (T_{m-1}^{n-1})^2\right]\right\}, \tag{140}$$

where

$$A_L = \left(\frac{k_o}{\rho c_o}\right)\frac{\Delta t}{(\Delta x)^2} \quad ; \tag{141}$$

$$T_L = T_{L+1} \quad ; \tag{142}$$

$$T_m^{\,n} = T_m^{n-1} + \frac{B}{T_m^{n-1}}\left[k_{o,L+1}\left(\frac{T_{m+1}^{n-1} + T_m^{n-1}}{2}\right)\left(\frac{T_{m+1}^{n-1} - T_m^{n-1}}{(\Delta x)_L}\right)\right.$$

$$\left. - k_{o,L}\left(\frac{T_m^{n-1} + T_{m-1}^{n-1}}{2}\right)\left(\frac{T_m^{n-1} - T_{m-1}^{n-1}}{(\Delta x)_L}\right)\right] \quad ; \tag{143}$$

where

$$B = \frac{4(\Delta t)}{(\rho_L c_L + \rho_{L+1} c_{L+1})[(\Delta x)_L + (\Delta x)_{L+1}]} \tag{144}$$

and

$$-k_o\left(\frac{T_o^{\,n} + T_1^{\,n}}{2}\right)\left[\frac{3T_o^{\,n} - 4T_1^{\,n} + T_2^{\,n}}{2(\Delta x)_1}\right] = \bar{\varepsilon}_M\sigma(T_o^{\,n}) - \bar{\varepsilon}_M I(\xi, n, t) \, . \tag{145}$$

As before, we cannot predict explicitly what effects the temperature dependence of the thermal properties will have upon the shape of eclipse and lunation cooling curves. For a given outward flux when the surface is cooling, one expects that a larger temperature gradient would be required near the surface than farther in where the temperature is higher. This is apparent if we compare the temperature distribution immediately below the surface during an eclipse for a temperature-dependent model with that for a temperature-

independent model (Figure 25). The exact effect this variable temperature gradient has upon the surface temperature at any time, however, can be found only by obtaining the solution of Eq. (140), subject to the appropriate boundary conditions.

The results of such computations (see Figure 28) show that homogeneous models characterized by the parameter $\gamma_{350^\circ K} \equiv (k\rho c)^{-1/2}$ at 350°K, exhibit the same rate of cooling as do the lunation data. We have assumed that $\rho = 1$ gm cm^{-3} and $c = 0.20$ cal gm$^{-3}{}^\circ K^{-1}$ at 350°K. A model with $\gamma_{350^\circ K} =$ 450 appears to be about the best fit. Clearly, two-layer models with depths less than about 6 cm are ruled out, as are horizontally inhomogeneous models.

Homogeneous temperature-dependent models come close to fitting the eclipse data for Tycho and its environs as shown in Figure 29. A typical two-layer model (see Figure 30), such as that having an upper layer of material 7mm thick with $\gamma_{350^\circ K} = 800$ over a substrate with $\gamma_{350^\circ K} = 250$ is consistent with the data for the environs of Tycho. A model with the same lower layer material but an upper layer characterized by $\gamma_{350^\circ K} = 400$ and a depth of roughly 6 mm would be appropriate for the crater itself. However, any of a number of such models could fit the data.

From the above discussion it should be apparent that radically different models of the lunar surface can exhibit similar, and in some cases indistinguishable, cooling curves

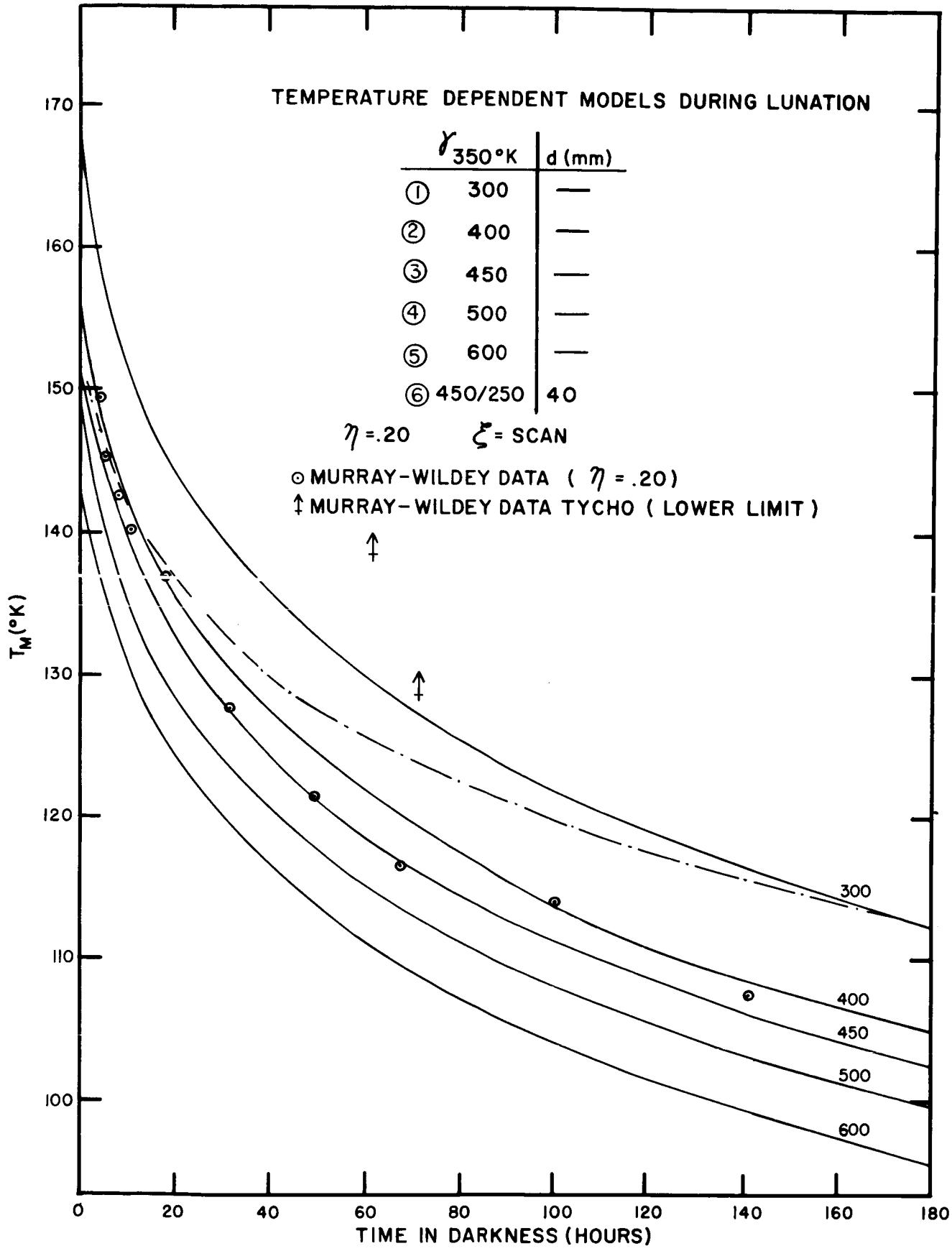

FIG. 28. Computed surface brightness temperatures for models assuming linear temperature-dependent thermal properties, $K = K_o T$, and $c = c_o T$. The value of γ characterizes these parameters at a temperature of 350°K. Changes in the data of Murray and Wildey are the same in Figure 23.

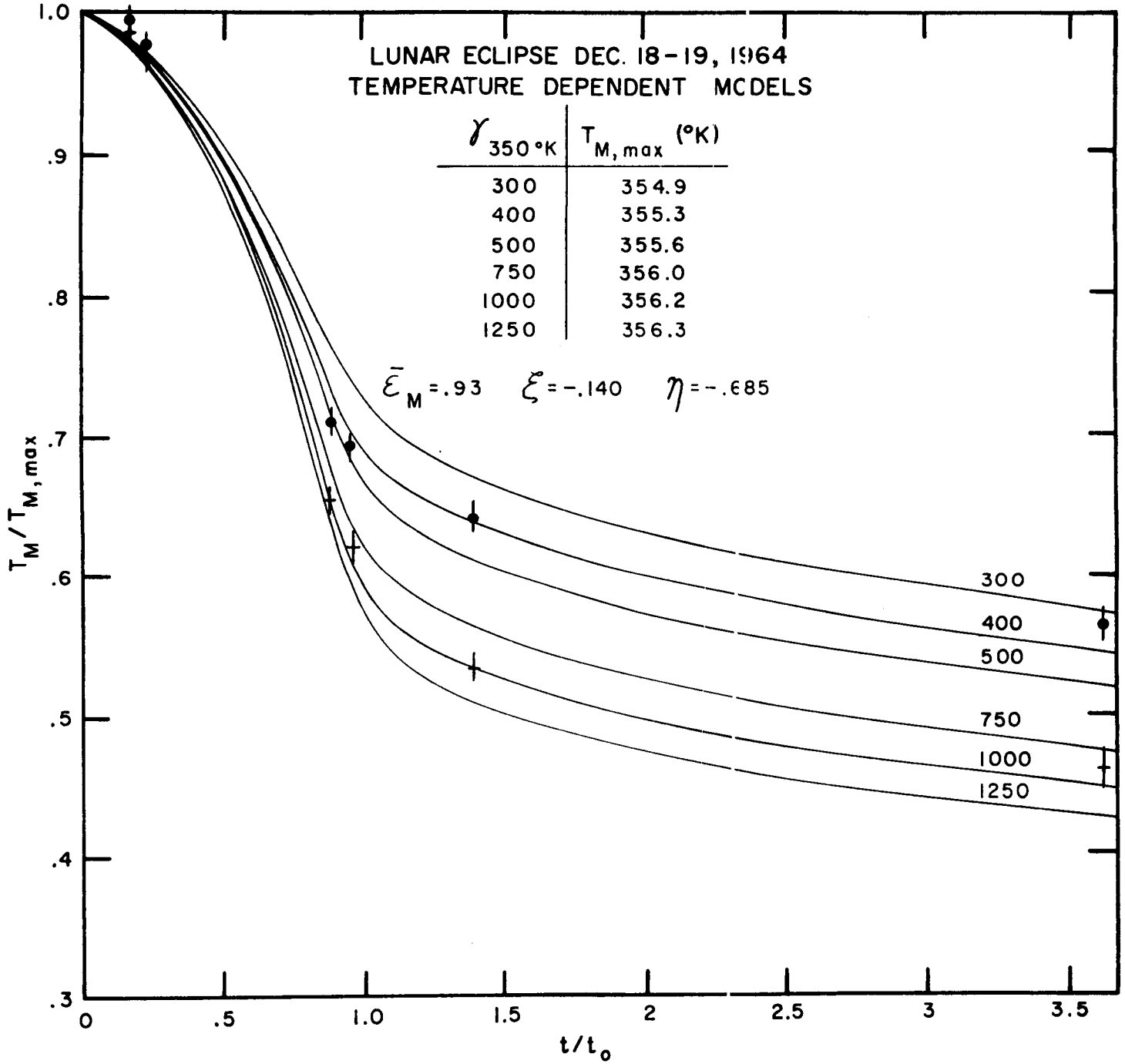

FIG. 29. Computed ratios of surface brightness temperatures to their pre-eclipse values for homogeneous models assuming linearly temperature-dependent thermal properties.

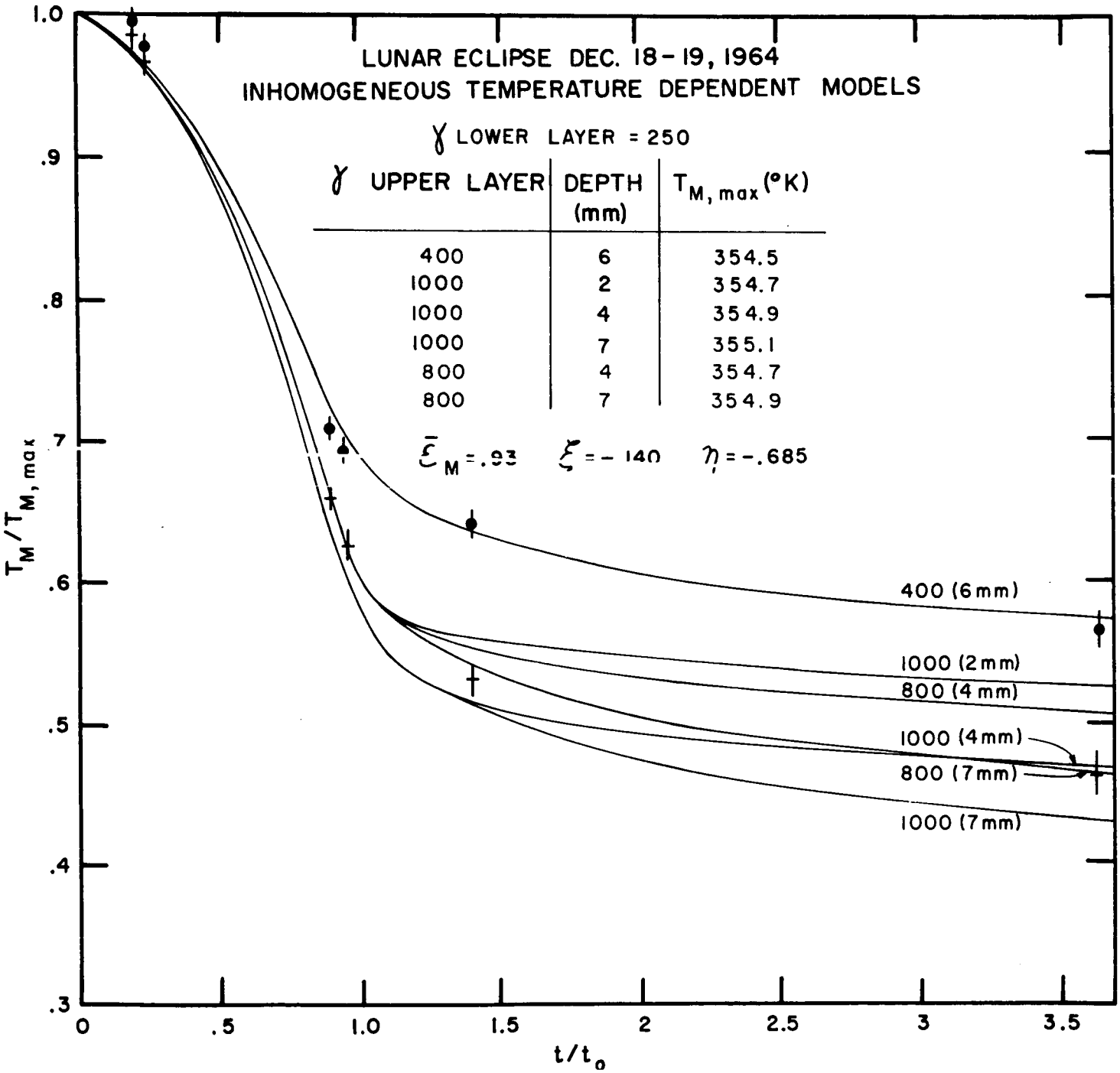

FIG. 30. Computed ratios of surface brightness temperatures to their pre-eclipse values for two-layer models assuming linearly temperature-dependent thermal properties.

during an eclipse and a lunation, and at the same time can have significantly different internal temperature distributions at millimeter and centimeter depths. Comparison of mm-wave radio observations of small regions of the lunar surface with predictions based upon each of these models, may be able to distinguish among them.

d) Conclusions

At a time when the problem of the lunar surface material has ceased to be a question of theoretical astrophysics and has become one of practical engineering, it is important to consider critically the alternative explanations not fully developed previously, of the thermal behavior of the lunar surface. Clearly, the anomalous crater Tycho can be readily explained in terms of simple two-layer temperature-independent models, but several other models agree equally as well with the data. In particular, the environs of Tycho can be explained by many different kinds of models; the large region scanned by Murray and Wildey can be accounted for by temperature-dependent or by radiative-conductivity models. In the light of our present inability to decide uniquely which of several plausible models applies even to any of the regions of the lunar surface we have studied, any detailed description of small-scale lunar surface structure, uncritically based upon any one kind of model yet devised, may be physically meaningless.

ACKNOWLEDGMENTS

This work was sponsored by the National Aeronautics and Space Administration under Grant No. NsG 64-60.

The authors wish to thank Mr. Roger Moore, former Head, Planetary Sciences, NASA, for his continued encouragement throughout the development of the first part of this program; Dr. A. D. Thackeray, director of the Radcliffe Observatory (Pretoria, Republic of South Africa) for allowing us to use the 74-inch reflector to observe the lunar eclipse on June 24-25, 1964; Mr. S. Roland Drayson of the University of Michigan for his assistance with the CO_2 band absorption data; and the members of the Infrared Laboratory at Harvard College Observatory for their assistance during various phases of this project. Thanks are also due to Mr. Richard Munro for supplying the original version of the computer program to integrate heat conduction equations.

REFERENCES

1. H. C. Ingrao and D. H. Menzel, Scientific Report No. 4, NASA Research Grant No. NsG 64-60, June 15, 1964.

2. R. Penndorf, J.Opt.Soc.Am., 47, 176 (1957).

3. R. Atkinson, M.N., 111, 448 (1951).

4. D. W. G. Arthur, Commun. Lunar & Planet. Lab, Vol. 11.

5. D. M. Gates and W. J. Harrop, Applied Optics, 2, 887 (1963).

6. W. M. Sinton and J. Strong, Ap.J., 131, 470 (1960).

7. W. M. Sinton and J. Strong, Ap.J., 131, 459 (1960).

8. B. C. Murray and R. L. Wildey, Ap.J., 139, 734 (1964).

9. R. M. Goody, Quarterly J. Roy. Meteorol. Soc., 78, 165 (1952).

10. R. M. Goody, The Physics of the Stratosphere, Cambridge University Press, New York (1958).

11. W. M. Elsasser, Harvard Meteorological Studies, 6 (1942).

12. W. M. Elsasser, Phys.Rev., 53, 768 (1938).

13. F. Saiedy, Oxford Radiation Symposium, Abstract #30 (1959).

14. F. Saiedy, Ph.D. Thesis, London University (1960).

15. K. Bignell, F. Saiedy, and P. A. Sheppard, J.Opt.Soc.Am., 53, 466 (1963).

16. R. Drayson, University of Michigan Report 05863-6-T (1964).

17. U. S. Standard Atmosphere (1962).

18. M. Migeotte, L. Neven, and J. Swensson, Mémoires de la Societé Royale des Sciences de Liège, Special Volume No. 1 (1956).

19. J. Strong, Journal of the Franklin Institute, 232, 1, (1941).

20. T. Sasamari, Science Reports of the Tokoku University, Fifth Series, 11, 149 (1959).

21. A. Wesselink, B.A.N., 10, 351 (1948).

22. J. C. Jaeger, Australian J. of Phys., 6, 10, (1953).

23. J. C. Jaeger and A. F. A. Harper, Nature, 166, 1026 (1951).

24. B. Y. Levin, Astronomicheskii Zhurnal, 40, 1071 (1963).

25. J. H. Piddington and H. C. Minnett, Australian J. of Sci. Res. Series A, 2, 63 (1949).

26. F. L. Whipple, Ap.J, 111, 375 (1950).

27. A. E. Wechsler and P. E. Glaser, The Lunar Surface Layer, ed. by J. W. Salisbury and P. E. Glaser, Academic Press, New York (1964).

28. C. W. Allen, Astrophysical Quantities, Athone Press, London (1963).

29. F. B. Hildebrand, Methods of Applied Mathematics, Prentice-Hall, New York (1952).

30. R. D. Richtmyer, Difference Methods for Initial Value Problems, Interscience, New York (1957).

31. W. M. Sinton, The Moon, ed. by Z. Kopal and Z. K. Mikhailov, Academic Press, London (1962).

32. E. Pettit, Ap.J., 91, 408 (1940).

33. J. M. Saari and R. W. Shorthill, Boeing Scientific Research Laboratories D1-82-0176 (1962).

34. A. R. Geoffrion, M. Korner, and W. M. Sinton, Lowell Observatory Bulletin No. 106 (1960).

35. R. L. Wildey, Private communication.

36. K. J. K. Buettner, Planetary and Space Science, 11, 135 (1963).

37. R. W. Muncey, Nature, 181, 1458 (1958).

38. R. W. Muncey, Australian J. of Phys., 16, 24 (1963).

39. R. B. Scott, J. Res. Nat. Bur. Stand., 58, 317 (1957).

40. E. C. Bernett, H. L. Wood, L. D. Jaffe, and H. E. Martens, AIAA J., 1, No. 6 (1963).